Supporting Information

Evaluation of *in situ* thermal stability assessment for flow batteries and deeper investigation of the ferrocene *co*-polymer

Ivan A. Volodin[a,b], Katrin Wulf[a,b], Felix Tzschoeckell[a,b], Steffi Stumpf[a,c], Stephanie Hoeppener[a,c], Nicole Fritz[a,c], Cristina Morales-Reyes[d], Thomas Wichard[d], Nico Ueberschaar[e], Christian Stolze[a,b], Martin D. Hager[a,b,c] and Ulrich S. Schubert[a,b,c]*

[a] Laboratory of Organic and Macromolecular Chemistry (IOMC), Friedrich Schiller University Jena, Humboldtstr. 10, 07743 Jena, Germany

[b] Center for Energy and Environmental Chemistry Jena (CEEC Jena), Friedrich Schiller University Jena, Philosophenweg 7a, 07743 Jena, Germany

[c] Jena Center for Soft Matter (JCSM Jena), Friedrich Schiller University Jena, Philosophenweg 7, 07743 Jena, Germany.

[d] Institute for Inorganic and Analytical Chemistry (IAAC), Friedrich Schiller University Jena, Lessingstraße 8, 07743 Jena, Germany

[e] Mass Spectrometry Platform, Friedrich Schiller University Jena, Humboldtstraße 8, 07743 Jena, Germany

* Corresponding author: Laboratory of Organic and Macromolecular Chemistry (IOMC), Friedrich Schiller University Jena, Humboldtstr. 10, 07743 Jena, Germany. E-Mail: ulrich.schubert@uni-jena.de

Table of Contents

Evaluation and mitigation of the zinc dendrite growth

The mixed galvanostatic-potentiostatic cycling of a PFc/Zn RFB with the OS-NF-8800 membrane has shown poor coulombic efficiency (CE) below 85% after 13 cycles at 99.8% CE (Figure S12). The visual inspection of the RFB membrane after the cycling test has revealed metal-like deposits on both sides of the membrane (Figure S13). The structures were confirmed as zinc dendrites by means of energy-dispersive X-ray (EDX) spectroscopy (Figure 3a, b). The dendrites are well recognized both at the membrane front-side sample (Figures 3a and S13), which contacted the RFB catholyte half-cell, and on the membrane cross-section image (Figure 3b). Thus, the reason for the CE drop was an intensive dendrite growth in the OS-NF-8800 and the net of micro-short circuits formed during cycling. Since the CE does not completely decrease to 0% value during the whole RFB test, we expect the charged PFc polymer to partially oxidize the newly formed dendrites at the outer membrane surface and to, consequently, prevent the complete short-circuiting. Such process was described by Xie *et al.* as a recovery of micro-short circuits inside the pores of a polyolefin size-exclusion membrane in a zinc-iodine RFB.[1] There, the recovery occurred by means of direct chemical oxidation of the zinc metal structures inside the pores by charged polyiodide anions crossing into the membrane. In our system, the 0.6 kDa membrane MWCO suppresses the polymer cross-over. Still, we expect similar membrane recovery processes to occur in the external PES layers, which are located closer to the catholyte side (*e.g.,* at the left side of the cross-section membrane sample in Figure 3b).

According to potentiostatic electrochemical impedance spectroscopy (PEIS) analyses (Figure S14) of both the RFB with the Spectra/Por 6 and the RFB with the OS-NF-8800 membrane, the resistance increases from 0.29 Ohm to the 2.02 Ohm, respectively. Higher separator resistances cause higher zinc concentration polarization at the membrane-electrode interface and, consequently, promote a dendritic deposit formation.[2] It is well investigated that decreasing the current density lowers the zinc concentration polarization and, thus, facilitates the formation of a more even metal layer on the electrode surface.[2] Subsequently, in the same RFB cell the older dendrite-punctured OS-NF-8800 membrane was replaced with a new piece of the same membrane and the battery cycling was performed at a lower current regime: Galvanostatic charge-discharge at 10 mA (2 mA cm^{-2}) with voltage cutoffs at 1.5 and 0.5 V with subsequent potentiostatic holding at these voltage limits until the current decreased to ≤ 2.5 mA (0.5 mA cm^{-2}). As it is seen in Figure S15, the coulombic efficiency reached stable values at approximately 99% during the cycling at lower current densities. Both charge-discharge tests have been performed during 5.5 to 6 days long periods. During RFB cycling at the high-current regime the CE started to drop starting from the thirteenth cycle (0.17 days), while during the test at lower fixed current densities the CE stayed at 99% over the whole 100 cycles (5.93 days). Subsequently, the experiment has been repeated in both current regimes (Figure S15) showing very similar behavior. Thus, the results demonstrate the positive impact of a current decrease on the stability and the CE of the RFB by avoiding intensive dendrite formation.

Furthermore, Figure 3c presents cross-section and front-side scans of the OS-NF-8800 membrane after the charge-discharge cycling in the lower current regime. Photographs of the membrane can be seen at the Figure S16. Both from the EDX scan (Figure 3c) and visual inspection (Figure S16) no dendrites were found at the membrane front-side and cross-section. Small zinc deposits could be visually detected at the back-side of the membrane indicating the beginning of dendrite growth. The full set of the EDX scans with their spectra for each of the membrane sides for a pristine OS-NF-8800 membrane and for the ones used during the charge-discharge cycling with higher and lower current densities can be seen in Figures S17-S28. The cross-section and front-side of the pristine OS-NF-8800 membrane piece (Figures S17 and S18) are largely identical to the corresponding scans of the membrane after the RFB cycling in the lower current regime (Figures S25 and S26). However, some zinc deposits can still be recognized both in the photos (Figure S16) and in the EDX scans (Figures S27 and S28) of the PP fibers reinforced back-side of the membrane after cycling in the lower current regime.

Validation of the CV and UV-Vis techniques

The techniques may not detect PFc in the *post mortem* RFB anolyte if the polymer is being fully degraded after crossing the membrane. To rule out this possibility a full RFB test with an intentionally PFc-contaminated anolyte was performed, *i.e.*, the catholyte contained 27 mM PFc, 0.1 M $ZnCl_2$, 0.8 M NH_4Cl while the anolyte contained 2.7 mM PFc, 0.1 M $ZnCl_2$, 0.8 M NH_4Cl. The 2.7 mM PFc concentration in the anolyte was chosen, since the estimated difference of the total capacity fade over 5.7 days cycling between the least stable full RFB and the UCSFCC corresponds to roughly 10% of catholyte PFc concentration. The full RFB with the fresh 2.7 mM PFc, 0.1 M $ZnCl_2$, 0.8 M NH_4Cl anolyte was pumped for a 0.5 hour period. Then a portion of the anolyte was taken to estimate the PFc content *via* UV-Vis and CV measurements. After that, the RFB was cycled for a 5.7 day period and, subsequently, the anolyte was taken again to analyse the PFc content *via* UV-Vis and CV (Figures S35 and S36). According to UV-Vis, the polymer concentration in the anolyte has decreased by only 9%, whereas a decrease of 25% was measured from the CV. The UV-Vis test results are considered more accurate, since a proper calibration was done prior to the measurement (Figures S30 and S31). From both methods, the assessed fade rate of the PFc in the anolyte does not correspond to a value which would be sufficiently high to make the PFc invisible for the cross-over assessment. Thus, the CV and UV-Vis techniques are sufficient to track the PFc cross-over.

A brief review of temperatures applied during *in operando* thermal stability assessment in redox flow batteries (RFBs)

The temperature stressed stability assessment tests provide at least two benefits:

1) Acceleration of stability assessment experiments, and
2) investigation of system behavior at stressed conditions.

Both possibilities are very attractive, though it is not obvious how high or low temperatures may it be reasonable to apply? The suitable conditions depend on the aim of the investigation.

If the first benefit is prioritised, established temperature limits are not defined. In case if the reaction mechanism is well-known and no additional processes occur inside the chosen temperature range, according to Arrhenius model of kinetic behavior, it may be possible to facilitate stability assessment by 2 to 4 times with each additional 10 °C and at the same time to avoid catastrophic failure occurrence (*i.e.*, involvement of an additional capacity fade mechanism, which causes very fast device degradation and subsequent failure). The more stable a device is, the longer period may be needed to assess its stability with sufficient accuracy. Thus, more promising systems require far more time for characterization. From this perspective, redox flow batteries struggle with very long experimental time requirements, as the device is developed to work for years and as it is hardly possible to run several identically planned experiments simultaneously during the research. In most cases, an RFB experiment requires high reagent portions, a pump, and relatively large space, thus, due to system design characteristics it is very challenging to run many experiments at once. Consequently, the time limitations become very problematic when it comes to stability assessment in RFBs; hence, every opportunity to facilitate the process is favoured. Thus, for stable RFB systems the first benefit is very relevant.

Regarding the second benefit, the practically reasonable highest and lowest temperature thresholds depend on the real RFB operating conditions. According to VRFB thermal modelling work by A. Tang *et al.*,[3] in case, when the ambient temperature is fixed at 25 °C, the stack temperature may rise up and stabilize at 40 °C during continuous charge-discharge operation using 67 mA cm^{-1} current densities. In another study by A. Trovo *et al.* a thermal model was experimentally validated using an industrial VRFB installation.[4] The model has subsequently shown that at 20 °C fixed ambient temperature, a stack can heat up from initial 32 °C to the value of 53 °C, when 667 mA cm^{-1} current density is applied over 8 hours long discharge process (in the publication a discharge process is confirmed to generate more heat). In the real case, of course, the surrounding temperature may change, depending on the climate. Therefore, in the study by A. Tang and M. Skyllas-Kazacos,[5] a VRFB stack temperature in a 5 kW power, 30 kWh capacity flow battery was simulated for operation in summer and winter in three geographic positions: a) Sapporo, Japan (average annual temperature (AAT) ~ 6 °C);[6] b) Sydney, Australia (AAT 18 °C);[7] and c) Dubai, United Arab Emirates (AAT 28 °C).[8] For comparison: The hottest annual climate temperature among all cities on Earth corresponds to 32.9 °C (Makkah, Saudi Arabia)[9] and one of the coldest is −12.5 °C (Oymyakon, Russian Federation).[10, 11] Thus, Dubai climate is fairly close to one of the hottest, while Sapporo is more likely between the medium and cold climate conditions. According to the study, during Dubai-Summer as the hottest scenario the stack electrolyte can reach its maximum temperature of 57 °C in a standby mode, when heat transfer between the stack and the environment interferes with exothermic self-discharge reaction due to the cross-over.[5] As soon as the electrolyte begin to be pumped, the temperature between the tanks and the stack starts to equilibrate and stabilizes at 45 °C. Correspondingly, during Sapporo-Winter as the coldest scenario the stack may heat up to 17 °C in the standby mode and cools to 5 °C, when the electrolyte is pumped. Based on the thermal modelling works for VRFBs, in practice the flow battery electrolyte and stack temperatures may hardly exceed 60 °C, when the energy storage installation does not include cooling units. Thus, we propose the 60 °C as the practically reasonable highest temperature threshold for *in operando* thermal stability studies. So far, we could not find thermal modelling works or experimental studies performed for extreme cold climate. Nevertheless, to compensate for absence of the magnitude, in this contribution we state the currently experimentally covered temperature ranges.

To make an overview of currently investigated temperature range of *in situ* thermal stability assessment studies in RFBs we briefly discuss research on the topic for iron-chromium,[12-14] iron-vanadium,[15] all-vanadium (only publications, which were reported during the last four years, starting from 2019),[16-24] zinc-inorganic (*i.e.,* mainly halogen or cerium-based

catholyte),[25-32] and organic RFBs.[33-45] The extreme low applied temperatures are −40 °C for acetonitrile-based RFB with organic electroactive materials,[38] −32 °C for mixed ionic liquid-water RFB with phthalocyanine-iron chloride electroactive couple[33] and −20 °C for all-vanadium and zinc-iodine aqueous RFBs.[20, 32] Subsequently, currently for aqueous systems the −20 °C condition is the lowest threshold for *in situ* thermal stability assessment. However, it is worth noting, that the actual practically reasonable threshold for low temperature electrolyte stability assessment can now hardly be defined, because of a lack in publications, where modelling of RFB electrolyte and stack temperatures in extreme cold climates (*e.g.,* Oymyakon and *etc.*) is presented. The *in situ* studies at extreme high temperatures are represented by nonaqueous system, applying phenothiazine-viologen derivatives battery at up to 70 °C,[45] by aqueous systems, applying iron-chromium battery at 65 °C,[12-14] , and by the already mentioned ionic liquid-water mixed electrolyte system, applying phthalocyanine-iron battery at 65 °C.[33] It is worth noting that for iron-chromium systems the 65 °C is desired not on account of thermal stability assessment, but because that is an optimum operational temperature for the RFB type.[46] Consequently, so far to our knowledge, if one excludes the Fe-Cr system and concentrates on the aqueous-based electrolytes, then 60 °C is the highest studied value, supporting our proposal to consider 60 °C as the practically-reasonable threshold. Such high temperatures were reached in several aqueous electrolytes, namely zinc-bromine,[25, 30] zinc-cerium,[26] all-vanadium,[16, 22, 23] symmetric anthraquinone-2,6-disulfamidic acid,[44] and PFc-BTMAPV systems.[43] Therefore, in our research on the PFc electrolyte stability at elevated temperatures we decided to conduct studies in the range from the glovebox ambient temperature to 60 °C.

Choice of the heating setups

Table S1 presents the commonly applied types of heating setups in the flow battery literature. Among the 31 analyzed publications, in eight of them a heating setup is not described.[12, 14, 22, 25, 26, 32, 39, 41] In other eleven publications, strongly localized heating was performed as, *e.g.*, putting tanks in water bath[19-21, 27, 35, 36, 43, 44, 47] or heating only the flow cell.[31, 37] And the highly homogeneous heating configurations as, *e.g.*, thermostat were applied in ten of the observed references.[13, 15-17, 23, 24, 29, 30, 33, 38] Also, there were found intermediately homogeneous heating setups, where heating was performed both in tanks and in a flow cell, while tubing and pump were kept at ambient temperature.[34, 45] A good example of such configuration is a scientific contribution by Quinn *et al.*[45] where both tanks and the flow cell were heated and a pre-calibrated temperature probe was additionally positioned on the flow cell walls (*cf.* Table S1).

Only in absolute homogeneous configurations as, *e.g.*, a thermostat which contains flow cell, tanks, tubing and pump, a desired temperature is supposed to be accurately reached. Unfortunately, in the reviewed publications it is not always specified, whether thermostat heating setups store the complete RFB set or, *e.g.*, keep the pump outside to save space. In such case the pump and the tubes connected to it are kept outside from the thermostat and these units would play a role of cooling zones and cause negative deviation of average electrolyte temperature from the heating setup atmosphere. Consequently, in less homogeneous heating configurations (as, *e.g.*, water bath) the negative deviation may be even bigger. To avoid inaccuracies in heating a bulk electrolyte, a temperature-sensing probe or a preliminary setup calibration should be used. Of course, the closer is the probe to electrolyte or the more calibration conditions are similar to the experimental ones, the more accurate is the following heating. In small amount of investigations a temperature-measuring probe immersed in electrolyte or placed near to it, IR thermal camera or a pre-calibration was used to ensure accuracy of heating to the desired temperature.[16, 29, 31, 34, 45] In other publications usage of such approaches to check the electrolyte temperature was not specified. Often, the absence of temperature sensing probes may be explained by the high corrosivity of RFB electrolytes. Nevertheless, it does not concern the IR-cameras and calibrations. Also, the probe may either be encapsulated or kept above the solution level and put down only for restricted time periods. Therefore, it is often possible to measure bulk electrolyte temperature by means of any of the mentioned methods and we suggest doing so in order to increase accuracy of thermal stability assessments performed in non-ideally homogeneous heating setups.

Since the PFc used in our investigation is sensitive to air and the battery cycling is performed in glovebox, the experiment's environment place additional constraints in the form of space limitations (prohibiting sufficiently large thermostats to contain a complete flow battery setup) and difficulties in workspace organisation (setup preparation and cleaning). These constraints were among the reasons for choosing particular heating setups. There are already existing thermal stability assessment studies performed in gloveboxes, where the following heating setups were applied: 1) Heating of the RFB tanks in a sand bath inside glovebox with temperature probe in sand (localized heating; temperature-sensing probe far from the electrolyte; sand instead of oil and water for the ease of maintenance and cleaning);[43, 44] 2) integration of temperature controller (which has both temperature assessment and heating function) in flow cell and additional positioning of tanks in a bath tempered to a desired temperature (intermediately distributed heating; temperature-sensing probe close to electrolyte);[34] and 3) placement of the whole RFB in a self-made thermostat inside a glovebox and assessment of temperature by probes inside tanks' leads and inside graphite block of the flow cell (highly uniform heat distribution; two probes positioned close to electrolyte; alternative to placement of a commercial thermostat, that does not suit to the constrained glovebox dimensions).[16] From these options for our investigation there was chosen the sand bath and the self-made thermostat setups. Usage of the two configurations enables to make a comparison between the heating setups: 1) Which can be used both in a glovebox and in standard conditions, 2) where temperature-sensing probe may be placed in various positions, and 3) where critical forms of localized and homogeneous heating are applied. Thus, the results of this comparison are supposed to suffice for estimation of a reliability of capacity fades, assessed in most of thermal stability assessment studies.

Heating setups applied for *in situ* thermal stability assessment in RFBs.

Table S1 Heating setups applied for *in situ* thermal stability assessment in RFBs.

RFB system	Article name and thermal range of RFB cycling	*In situ* heating setup	Ref.
	Zinc redox flow batteries		
Zn-I	Ambipolar zinc-polyiodide electrolyte for a high-energy density aqueous redox flow battery. Range −20 to 50 °C.	The setup is not described	32
Zn-Br	A complexing agent to enable a wide-temperature range bromine – based flow battery for stationary energy storage. Range r.t. to 60 °C.	Placement of whole RFB in climate chamber	30
Zn-Ce	The influence of operational parameters on the performance of an undivided zinc – cerium flow battery. Range 20 to 60 °C.	The setup is not described	26
Zn-Ce	Impact of electrolyte composition on the performance of the zinc – cerium redox flow battery system. Range 45 to 55 °C.	High volume tanks (0.5 L) placed in thermostatic water bath. No information about bath T probe position	27
Zn-Fe	A boron nitride nanosheets composite membrane for a long-life zinc-based flow battery. Range 50 °C.	Positioning of heating element directly in flow cell and assessment of heat distribution by IR thermal camera	31
Zn-$K_4[Fe(CN)_6]$	Efficient low-grade heat conversion and storage with an activity-regulated redox flow cell via a thermally regenerative electrochemical cycle. Range 25 to 50 °C.	Placement of whole RFB in climate chamber and assessment of heat distribution by IR thermal camera	29
Zn-Br	An organic imidazolium derivative additive inducing fast and highly reversible redox reactions in zinc-bromine flow batteries. Range 25 to 60 °C.	The setup is not described	25
	Iron-Vanadium redox flow batteries		
Fe-V	A new redox flow battery using Fe/V redox couples in chloride supporting electrolyte. Range 0 to 50 °C.	Placement of whole RFB in environment chamber	15
	Iron-Chromium redox flow batteries (limited to 4 random publications)		
Fe-Cr	Optimization studies on a Fe/Cr redox flow battery. Range 20 to 44 °C.	Schematic illustration of heater in tanks and T probe at tanks outlet, but no information specified in text	47
Fe-Cr	A composite membrane with high stability and low cost specifically for iron-chromium flow battery. Range 65 °C.	The setup is not described	14
Fe-Cr	Single cell performance studies on the Fe/Cr redox energy storage system using mixed reactant solutions at elevated temperature. Range 65 °C.	The setup is not described	12
Fe-Cr	A high-performance flow-field structured iron-chromium redox flow battery. Range 25 to 65 °C.	Placement of whole RFB in temperature chamber	13
	All-Vanadium redox flow batteries (limited to publications from 2019 to 2023)		
V-V	Enzyme-inspired formulation of the electrolyte for stable and efficient vanadium redox flow batteries at high temperatures. Range 25 to 60 °C.	The setup is not described	22
V-V	Temperature-induced precipitation of V_2O_5 in vanadium flow batteries-revisited. Range 30 to 60 °C.	Placement of whole RFB in self-made thermostat inside glovebox and assessment of T by probes inside tanks' leads and inside graphite block of flow cell	16
V-V	Tailoring the vanadium/proton ratio of electrolytes to boost efficiency and stability of vanadium flow batteries over a wide temperature range. Range −15 to 55 °C.	Placement of whole RFB in thermostat	17

RFB system	Article name and thermal range of RFB cycling	*In situ* heating setup	Ref.
V-V	Accelerated design of vanadium redox flow battery electrolytes through tunable solvation chemistry. Range −5 to 50 °C.	Placement of whole RFB in thermostat	24
V-V	A highly concentrated vanadium protic ionic liquid electrolyte for the vanadium redox flow battery. Range r.t. to 40 °C.	Julabo refrigerated/heating circulator, model F12-MA (thermostatic bath) heated RFB electrolyte (supposedly RFB tanks)	21
V-V	Improved broad temperature adaptability and energy density of vanadium redox flow battery based on sulfate-chloride mixed acid by optimizing the concentration of electrolyte. Range −20 to 50 °C.	Heating of RFB tanks in thermostatic water bath. No information about bath T probe position	20
V-V	Improved energy density and temperature range of vanadium redox flow battery by controlling the state of charge of positive electrolyte. Range −10 to 40 °C.	Heating of RFB tanks in thermostatic water bath. No information about bath T probe position	19
V-V	Boosting the thermal stability of electrolytes in vanadium redox flow batteries via 1-hydroxyethane-1,1-diphosphonic acid. Range 0 to 60 °C.	Placement of whole RFB in thermostat	23
	Organic redox flow batteries		
Anthraquinone deriv.-$K_4[Fe(CN)_6]$	Spatially resolved analysis of an organic alkaline RFB to investigate the influence of the operating conditions. Range 10 to 40 °C.	Custom RFB design where tubes with heating water were introduced to flow cell. No information about T probe position	37
Alloxazine deriv.-$K_4[Fe(CN)_6]$	Comprehensive study of the performance of alkaline organic redox flow batteries as large-scale energy storage systems. Range 25 to 55 °C.	The setup is not described	41
Alloxazine deriv.-$K_4[Fe(CN)_6]$	Effect of temperature on the performance of aqueous redox flow battery using carboxylic acid functionalized alloxazine and ferrocyanide redox couple. Range 20 to 45 °C.	The setup is not described	39
Phthalocyanine-Fe	Unlocking simultaneously the temperature and electrochemical windows of aqueous phthalocyanine electrolytes. Range −32 to 65 °C.	Placement of whole RFB in freezer/temperature chamber	33
Viologen deriv.-Phenothiazine deriv.	A prototype of high-performance two-electron non-aqueous organic redox flow battery operated at −40 °C. Range −40 to 25 °C.	Placement of whole RFB in freezer.	38
Viologen deriv.-TEMPO deriv.	Stability of TMA-TEMPO-based aqueous electrolytes for redox-flow batteries. Range r.t. to 40 °C.	Heating of RFB tanks in oil bath. No information about bath T probe position	36
Symmetric TEMPO deriv.	Structural alterations on the TEMPO scaffold and their impact on the performance as active materials for redox flow batteries. Range r.t. to 40 °C.	Heating of RFB tanks in oil bath. No information about bath T probe position	35
Symmetric Anthraquinone deriv.	Anthraquinone-2,6-disulfamidic acid: an anolyte with low decomposition rates at elevated temperatures. Range 32 to 60 °C.	Heating of RFB tanks in sand bath inside glovebox. T probe in sand from the bath	44
Phenazine deriv.-$K_4[Fe(CN)_6]$	Ultrastable aqueous phenazine flow batteries with high capacity operated at elevated temperatures. Range r.t. to 45 °C.	Integration of temperature controller with both T assessment and heating function in flow cell and additional positioning of tanks in bath tempered to desired T. Study performed in glovebox.	34
Viologen deriv.-Ferrocene deriv.	Aqueous redox flow battery suitable for high temperature applications based on a tailor-made ferrocene copolymer. Range r.t. to 60 °C	Heating of RFB tanks in sand bath inside glovebox. T probe in sand from the bath	43
MEEPT	Elucidating the effects of temperature on nonaqueous	Heating of RFB tanks with a flexible	45

RFB system	Article name and thermal range of RFB cycling	*In situ* heating setup	Ref.
symmetric and MEEPT-Viologen deriv.	redox flow cell cycling performance	polyimide-based heater and of a flow cell silicone heating pads on both half-cells. Control of the heating based on outputs of a K-type thermocouple, positioned at the flow cell. Preliminary assessment of the heating accuracy by calibration with additional thermocouples at inlet and outlet of the flow cell. Heating accuracy ± 5 °C	

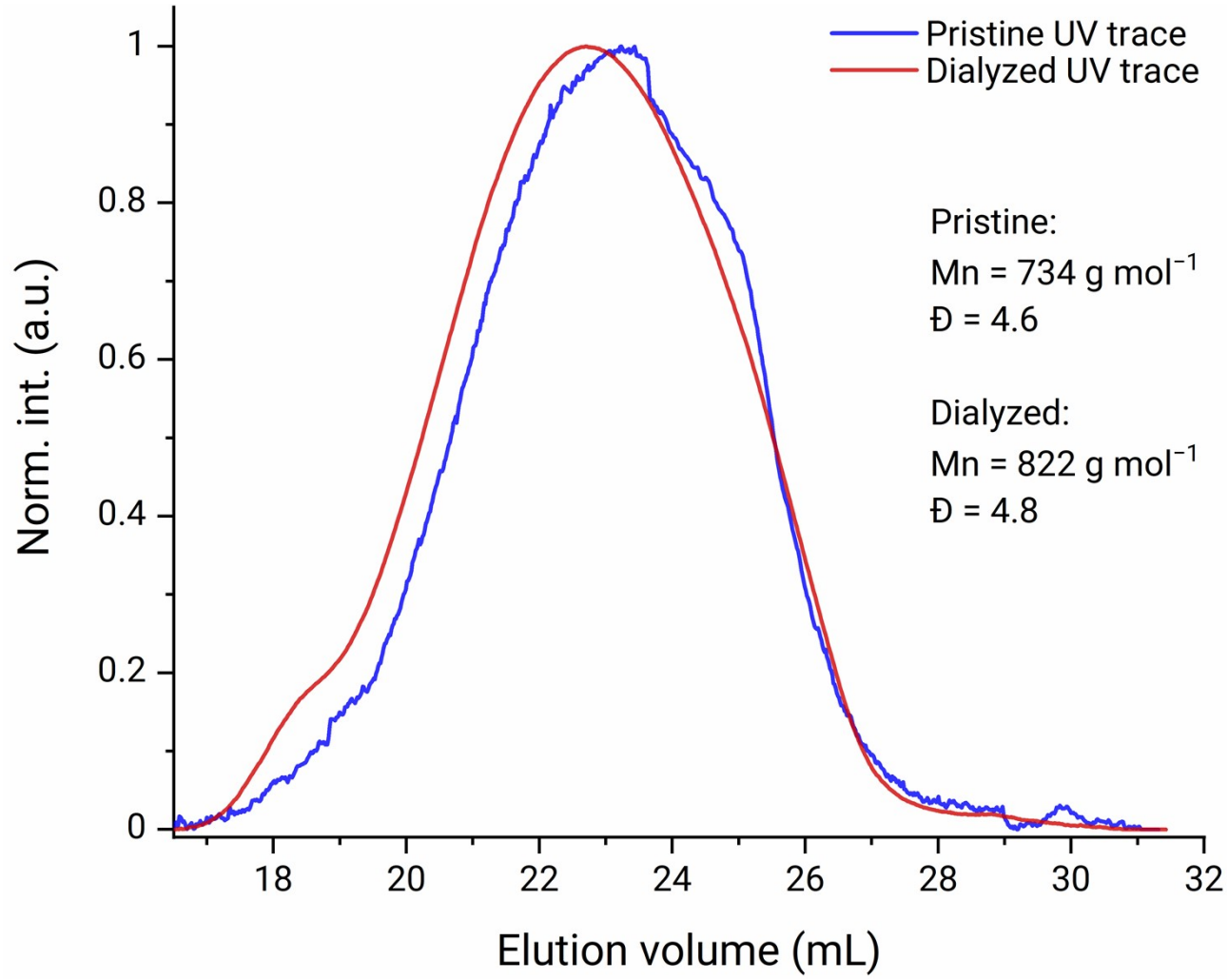

Figure S1 Elugram of the size-exclusion-chromatography of the PFc. The UV/VIS-traces (wavelength 309 nm) of the pristine and the dialyzed polymer are shown in blue and red, respectively. Both curves are normalized. 0.3% TFA + 0.1 NaCl solution in water was used as an eluent. P2VP was used as a calibration standard.

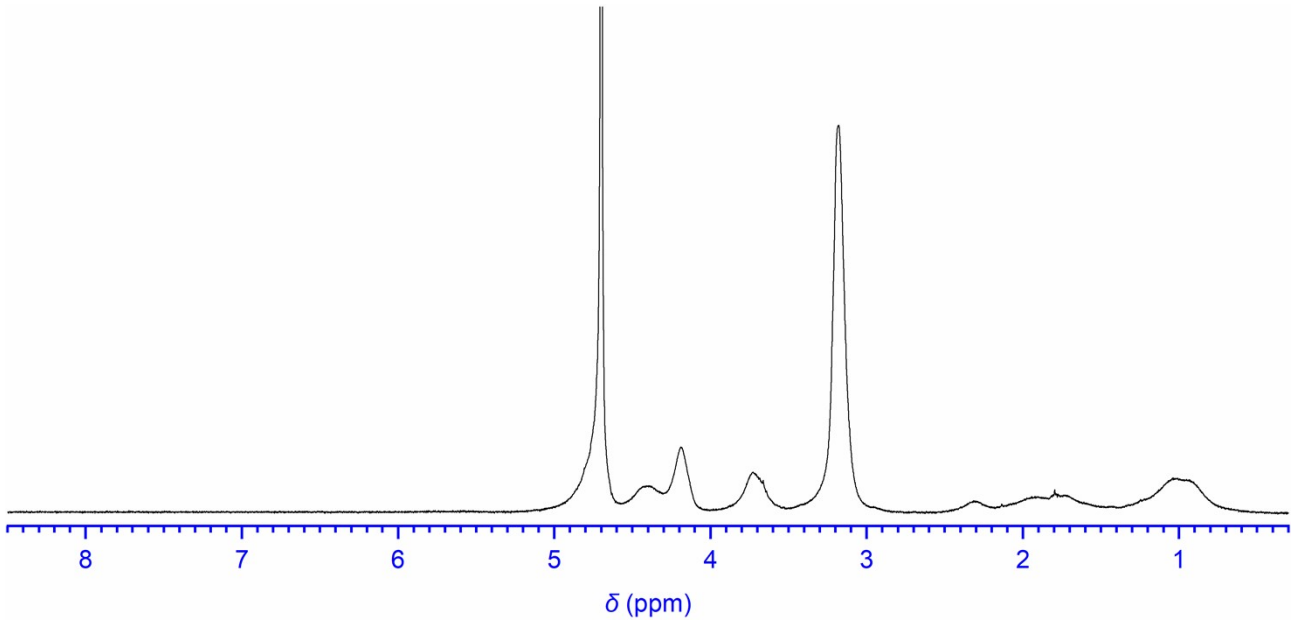

Figure S2 ^{1}H NMR spectrum of PFc (300 MHz, D_2O).

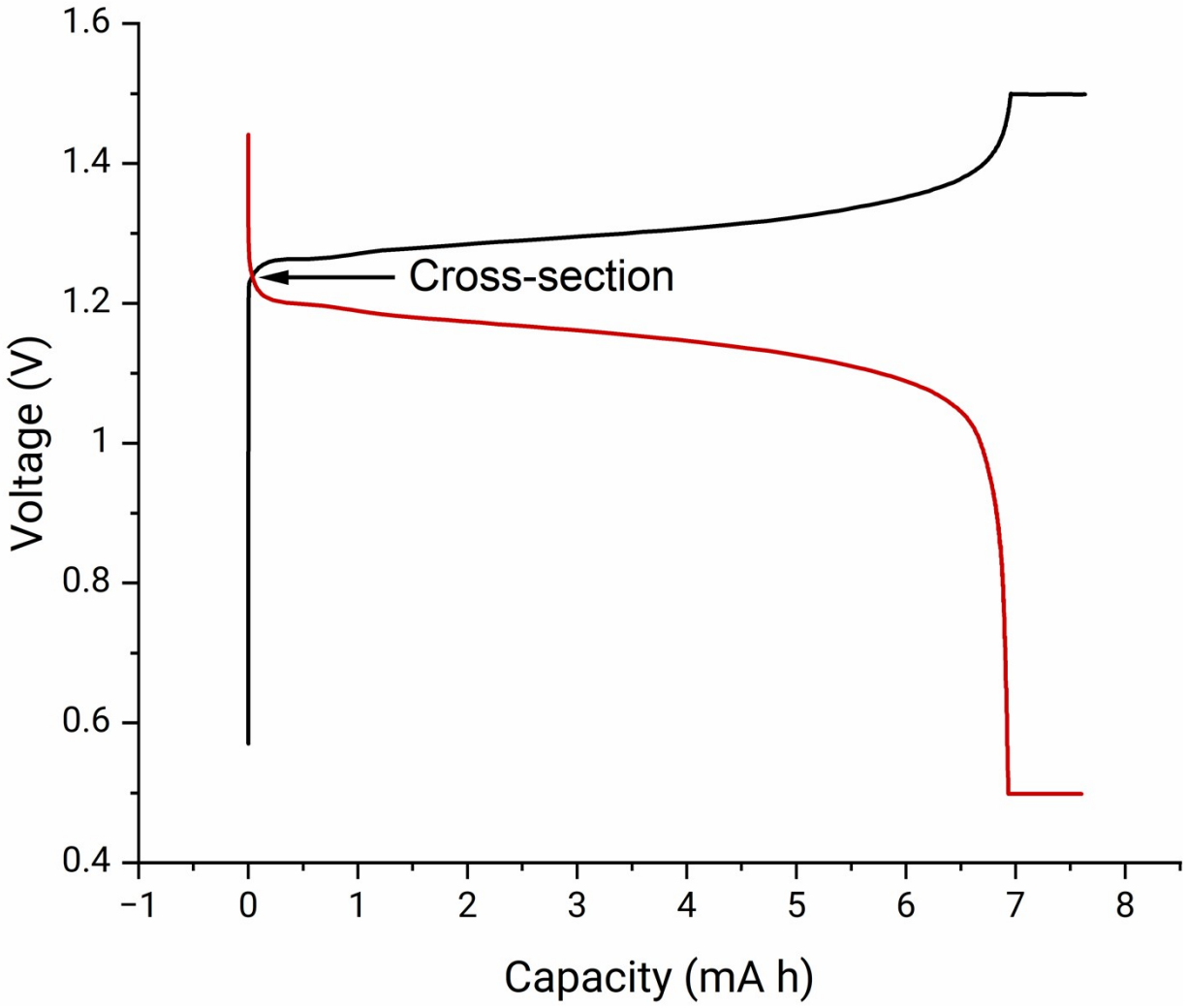

Figure S3 Exemplary cross-section of charge-discharge curves, which was used for estimation of the practical voltage of the PFc-Zn RFB

Potentiometric titration[35]

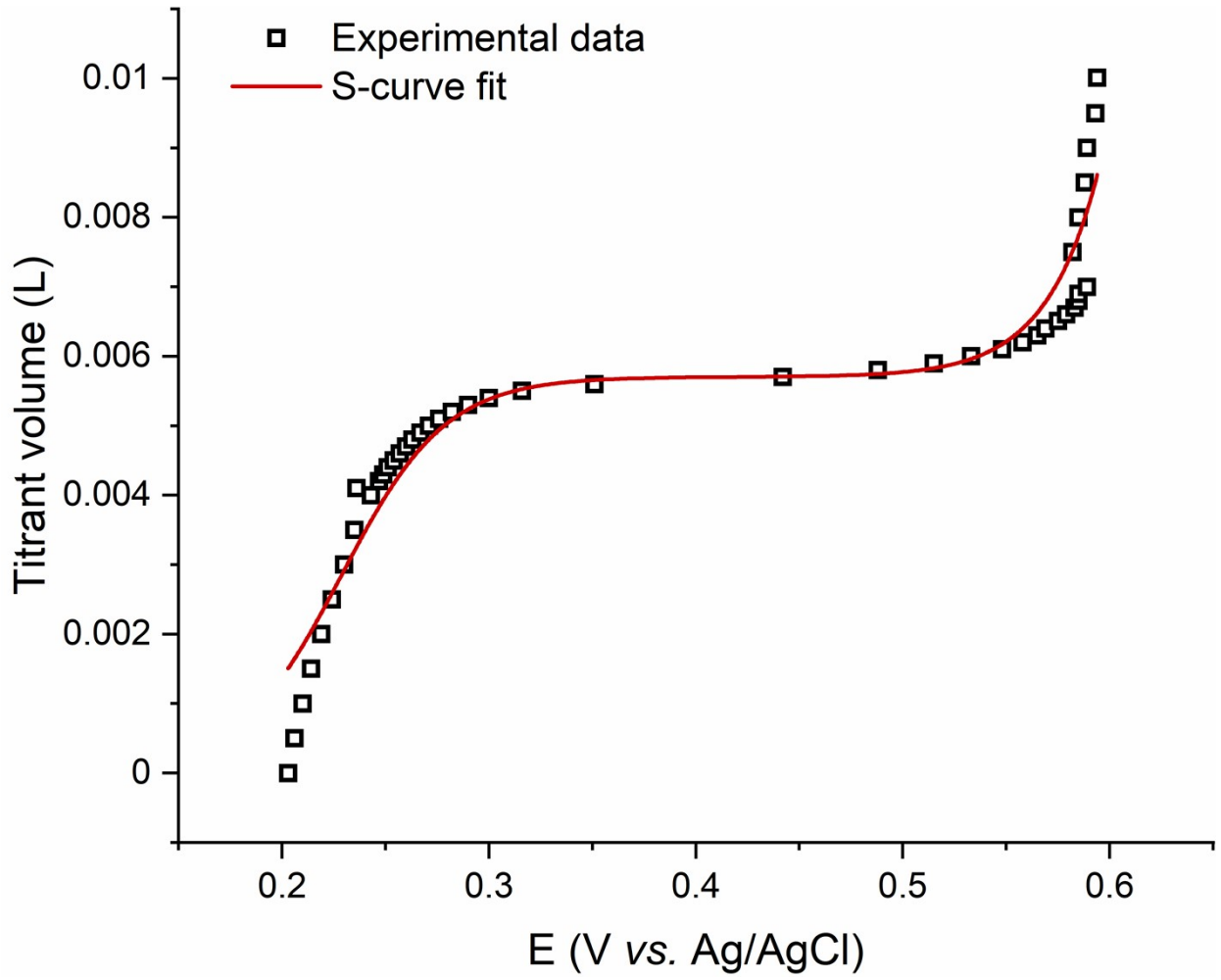

Figure S4 Exemplary redox titration curve of PFc solution in 1w/w% H_2SO_4 with the 0.203 mM $Ce(SO_4)_2$ in 1w/w% H_2SO_4 titrant. A digital redox potentiometer integrating both working and reference electrode was used to assess the electrolyte potential. The average ferrocene content in the PFc was estimated as the transition point on the fitted S-curve. The measurement was performed three times. The potential drift, occurring at 0.6 V, is reproducible and is subjected to PFc self-reduction, described in the Results and discussion, Subsection 3.2.3. Since no significant interference of the self-reduction was assessed at room temperature experiments, the process causes only negligible deviations in absolute charged and uncharged PFc concentrations. Still, the changes of the PFc state of charge in vicinity of SOC 100% are sufficient to cause the potential drift and, thus, to decrease the quality of the S-curve fit. Nevertheless, as it is proven by subsequent analyses in the Results and Discussion, Subsection 3.1.1, despite occurrence of the offset at 0.6 V, the accuracy of the potentiometric titration remains at sufficiently high level.

Atomic absorption spectroscopy

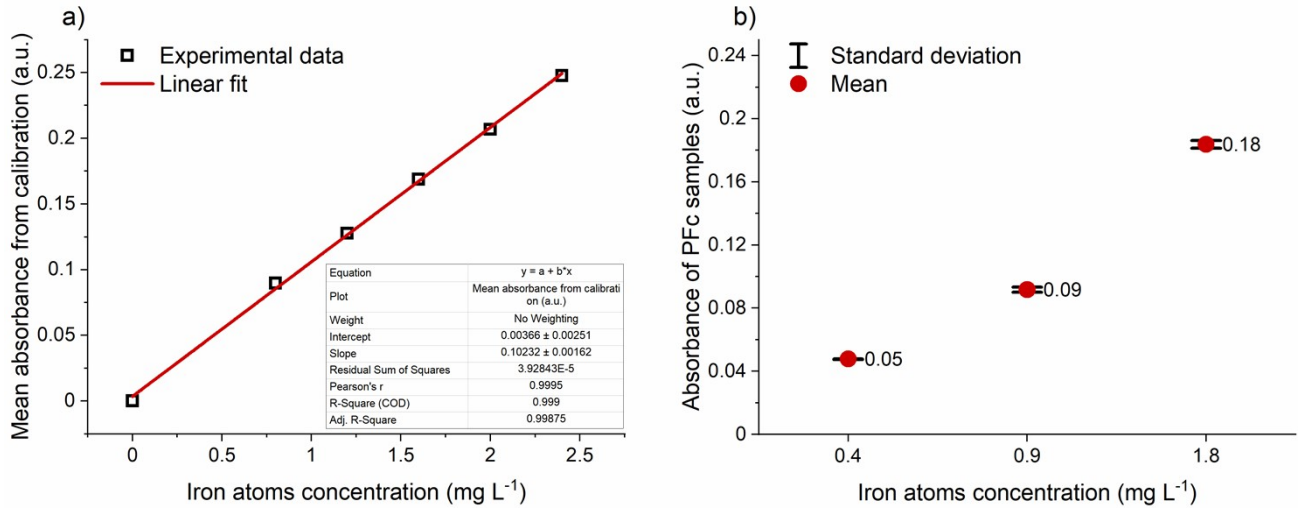

Figure S5 a) Calibration of the atomic absorption spectroscopy instrument with prepared iron cation solutions at defined concentrations (three replicates measured for each sample). b) Three replicate absorbance results from AAS analysis (the iron atoms concentration is calculated based on the preliminary measured calibration curve).

Exemplary curves from the RFB tests in higher current cycling regime

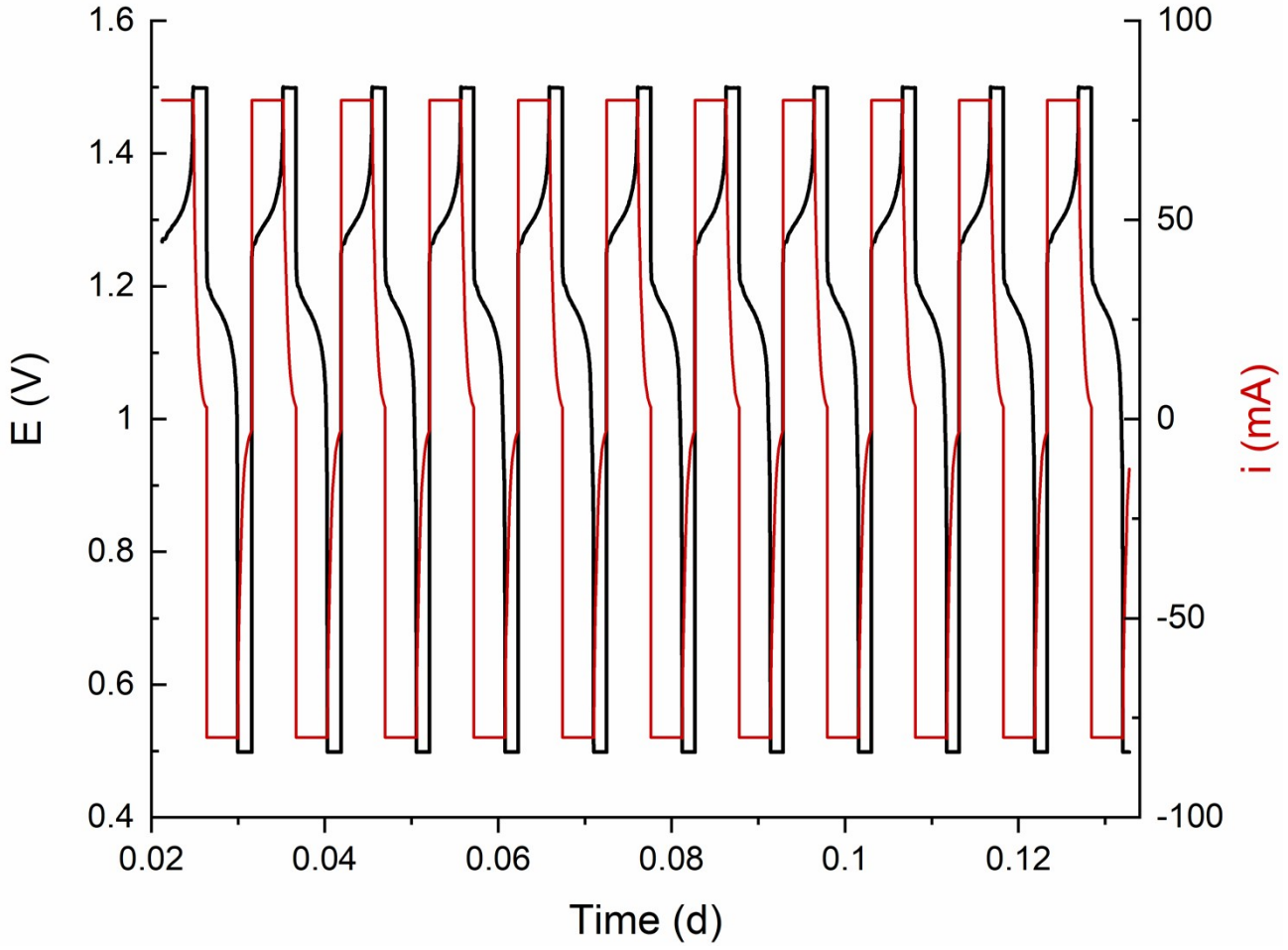

Figure S6 Exemplary RFB charge/discharge procedure, where galvanostatic regime at 16 mA cm^{-2} is mixed with potentiostatic holding at voltage cutoffs of 0.5 and 1.5 V till the current density decreases to ≤0.5 mA cm^{-2}.

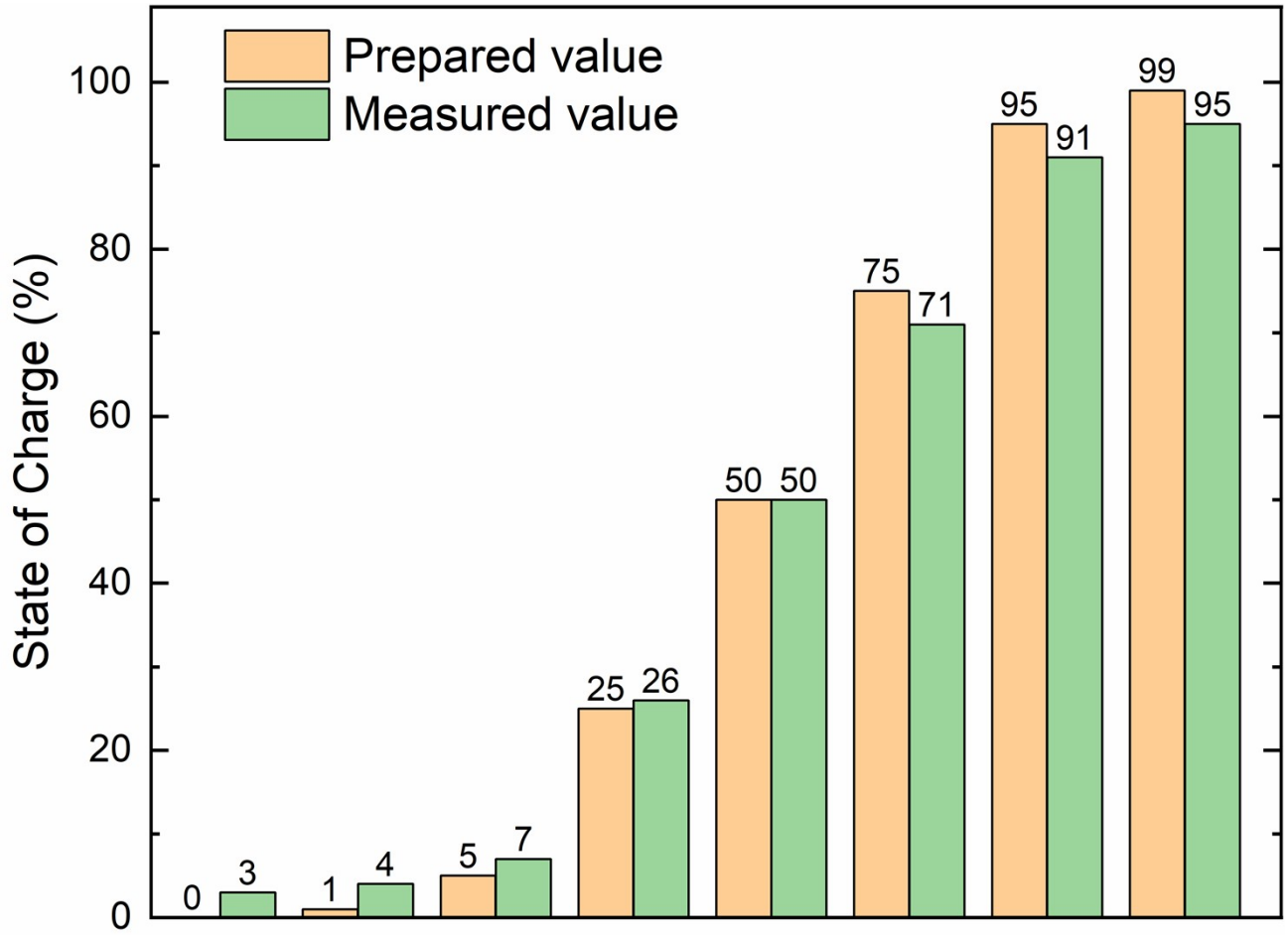

Figure S7 Comparison of the prepared SOC of the fresh catholyte solutions with their state of charge values measured with help of the steady-state amperometry. The assessed electrolytes were prepared by mixing of pre-charged and uncharged catholyte solutions (27 mM PFc, 0.1 M $ZnCl_2$, 0.8 M NH_4Cl).

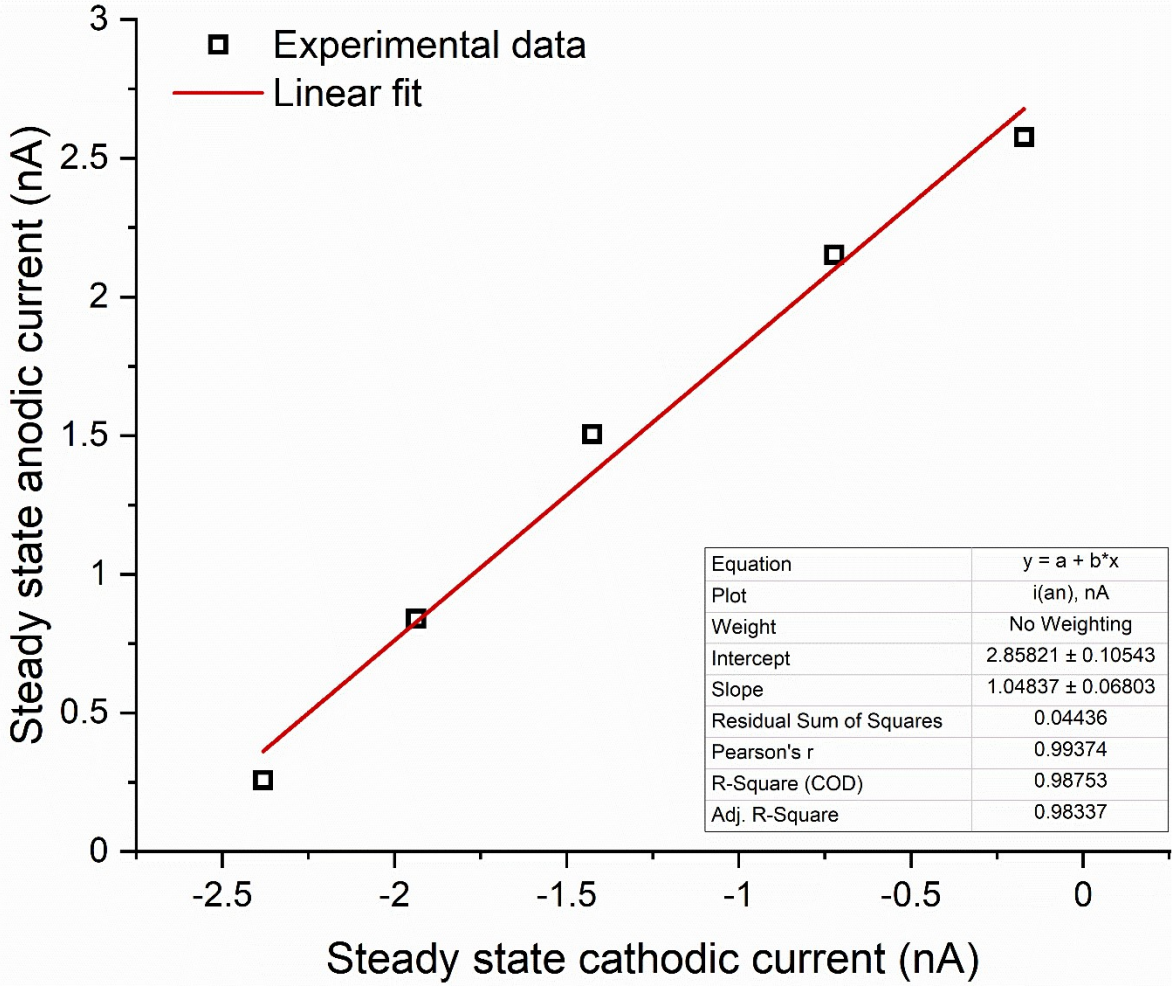

Figure S8 Plot of anodic *vs.* cathodic steady state current for samples with 5, 25, 50, 75, and 95% SOCs. The 1 and 99% SOC samples were excluded due to observation of a strong deviation from linearity. The curve slope corresponds to the ratio of diffusion coefficients of the reduced and the oxidized species, respectively (*i.e.*, D_{Red}/D_{Ox}). The ratio of the diffusion coefficients was further used in the SOC calculation for the experimentally measured values in Figure S7.

Photographs on the *post mortem* RFB electrolytes

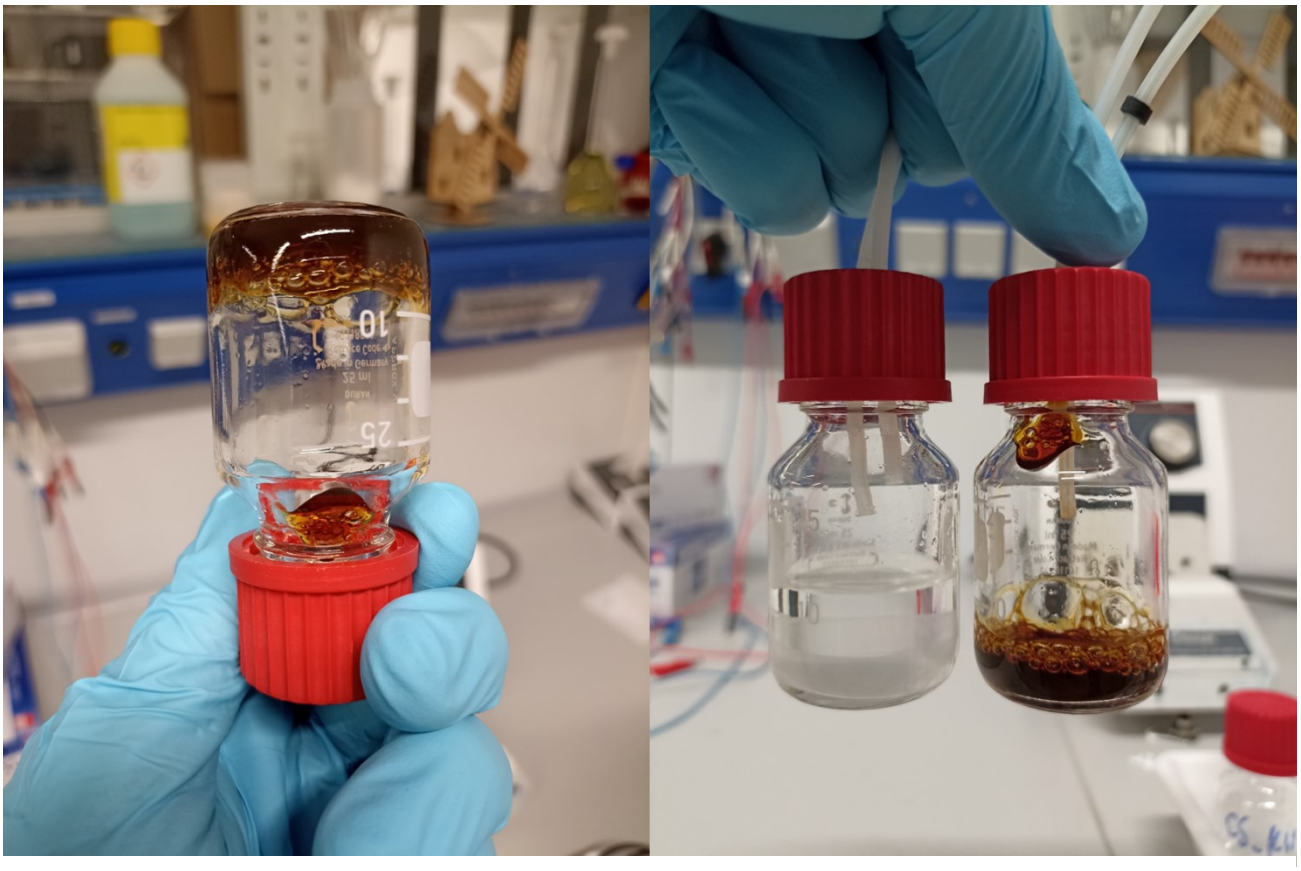

Figure S9 Photographs of RFB electrolytes after the battery cycling under ambient conditions, outside the glovebox. Conditions: Continuous battery cycling of 10 ml 27 mM PFc, 0.1 M $ZnCl_2$, 0.8 M NH_4Cl catholyte *vs.* 10 mL 0.1 M $ZnCl_2$, 0.8 M NH_4Cl anolyte galvanostatically at 16 mA cm^{-2} current in a 0.5 to 1.5 V cutoff voltage range with subsequent potentiostatic holding at cutoff voltages till absolute current value decreases to ≤0.5 mA cm^{-2}. Strong osmosis caused water transfer into the anolyte.

Figure S10 Photograph of the RFB electrolytes after battery cycling in the glovebox. Conditions: Continuous battery cycling of 10 mL 27 mM PFc, 0.1 M $ZnCl_2$, 0.8 M NH_4Cl catholyte *vs.* 10 mL 0.1 M $ZnCl_2$, 0.8 M NH_4Cl anolyte galvanostatically at 16 mA cm^{-2} current in a 0.5 to 1.5 V cutoff voltage range with subsequent potentiostatic holding at cutoff voltages till absolute current value decreases to ≤0.5 mA cm^{-2}.

Capacity fade during the UCSFCC test in, utilizing the NH_4Cl-based electrolyte

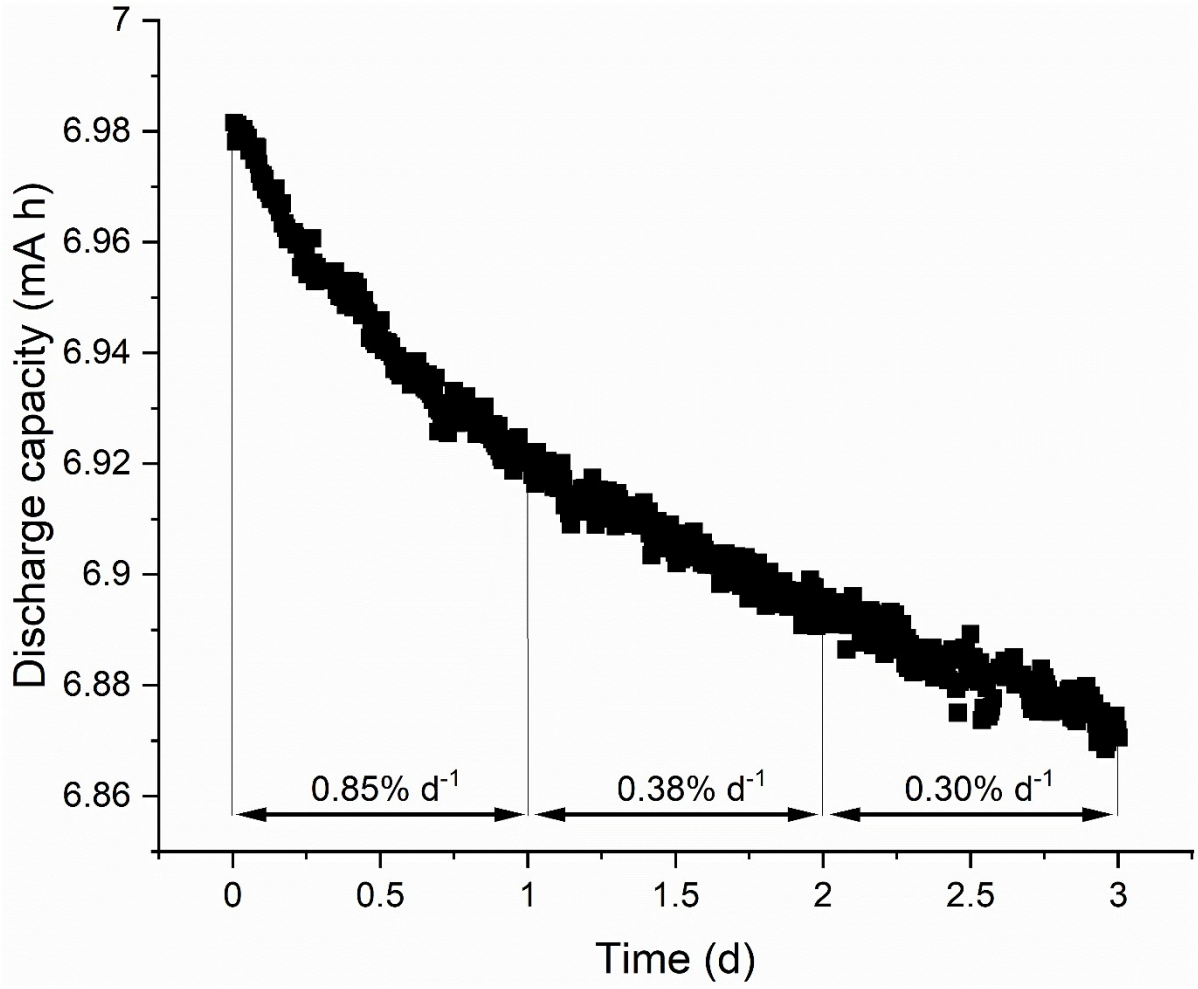

Figure S11 Capacity fade rate graph for the symmetric cycling. Conditions: 9 *vs.* 18 mL of 27 mM PFc, 0.1 M $ZnCl_2$, 0.8 M NH_4Cl electrolyte, potentiostatic cycling at ±300 mV voltages with 0.5 mA cm^{-2} current cutoff.

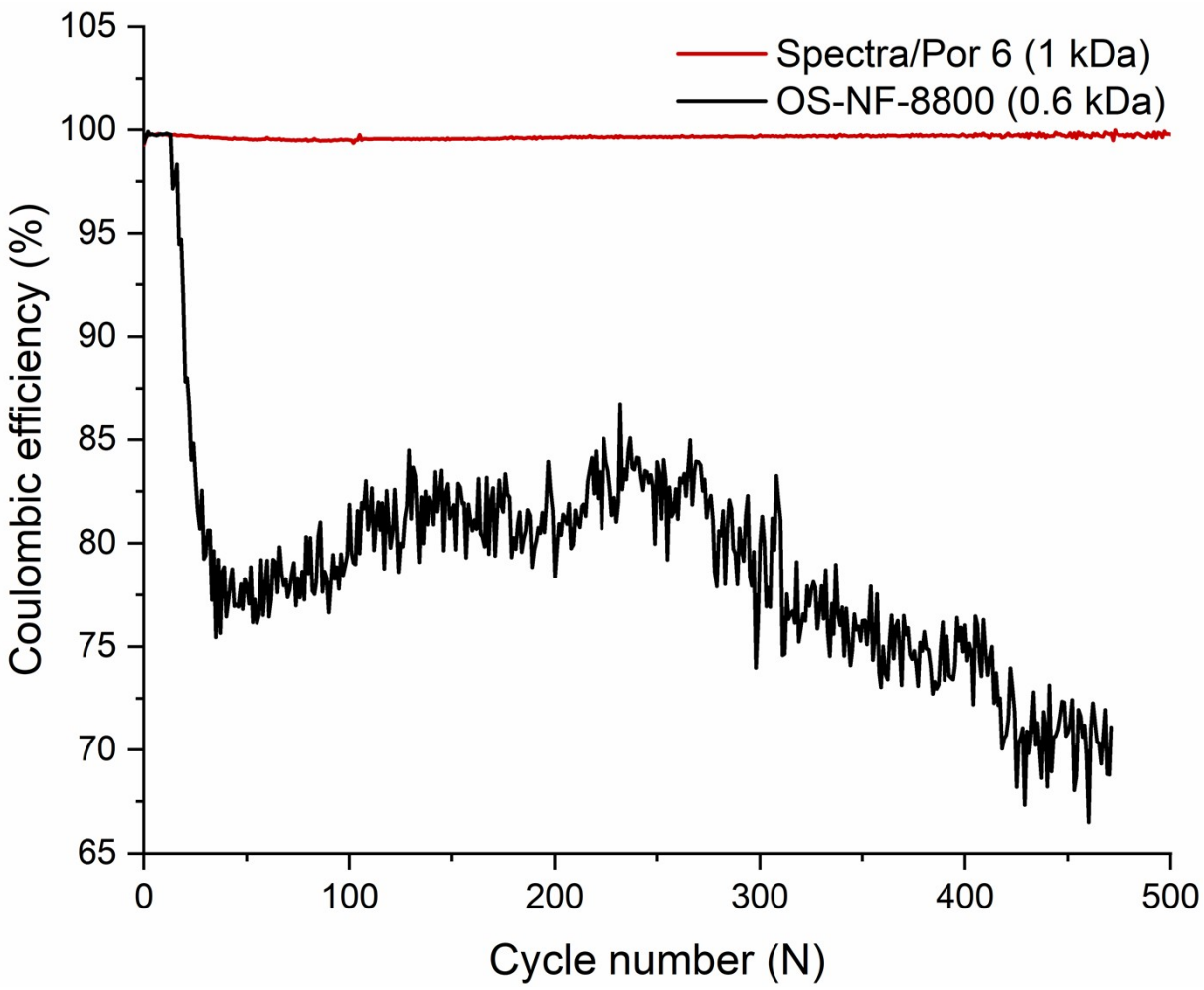

Figure S12 Coulombic efficiencies of the two RFBs cycled under the same conditions, but utilizing different membranes (*i.e.*, 1 kDa Spectra/Por 6 and 0.6 kDa OS-NF-8800). Conditions: Continuous battery cycling of 10 mL 27 mM PFc, 0.1 M $ZnCl_2$, 0.8 M NH_4Cl catholyte *vs.* 10 mL 0.1 M $ZnCl_2$, 0.8 M NH_4Cl anolyte galvanostatically at 16 mA cm^{-2} current in a 0.5 to 1.5 V cutoff voltage range with subsequent potentiostatic holding at cutoff voltages till the absolute current value decreased to ≤0.5 mA cm^{-2}.

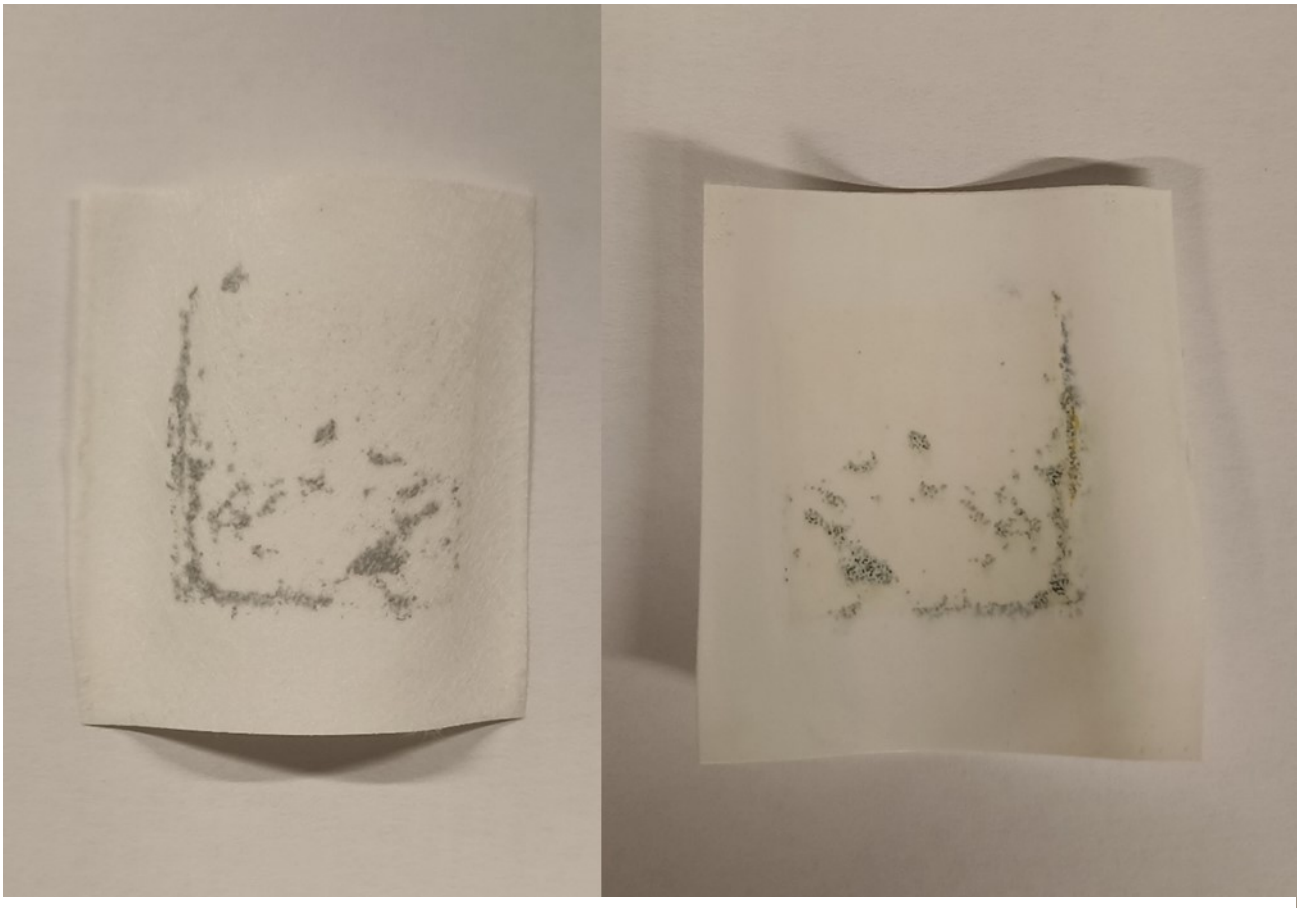

Figure S13 Photos of the PP and PES sides of the OS-NF-8800 membrane, respectively. The charge-discharge cycling was performed in the mixed galvanostatic-potentiostatic regime with 16 mA cm^{-2}, 0.5 and 1.5 V voltage cutoffs, and subsequent holding at the voltage cutoffs until the current decreased to ≤0.5 mA cm^{-2}. The PP side contacted the RFB anolyte and the PES layer faced the catholyte. Dendritic zinc deposits are visible on both sides.

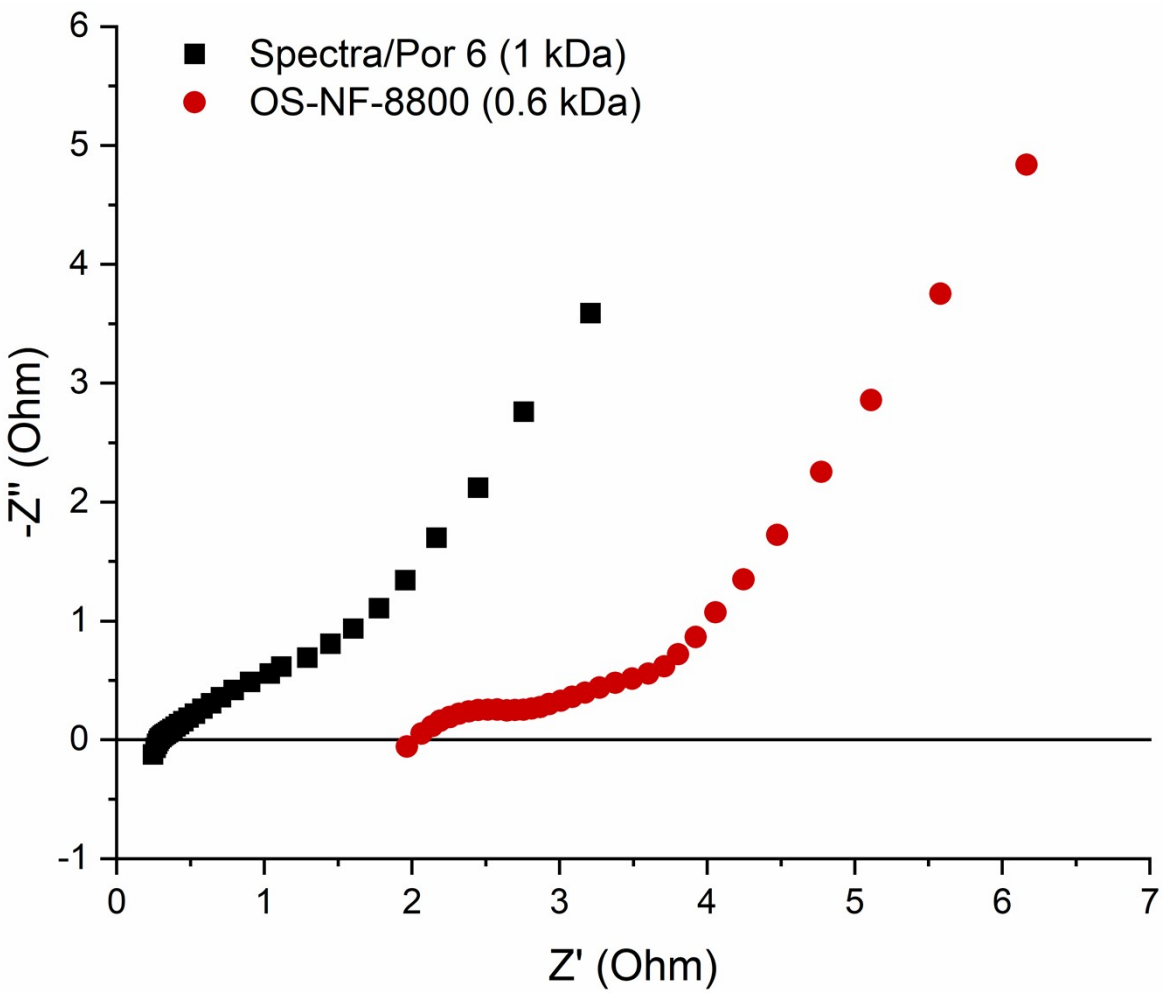

Figure S14 Potentiostatic electrochemical impedance spectroscopy (PEIS) of RFBs with Spectra/Por 6 and with OS-NF-8800 membranes. The PEIS was performed before the RFB cycling.

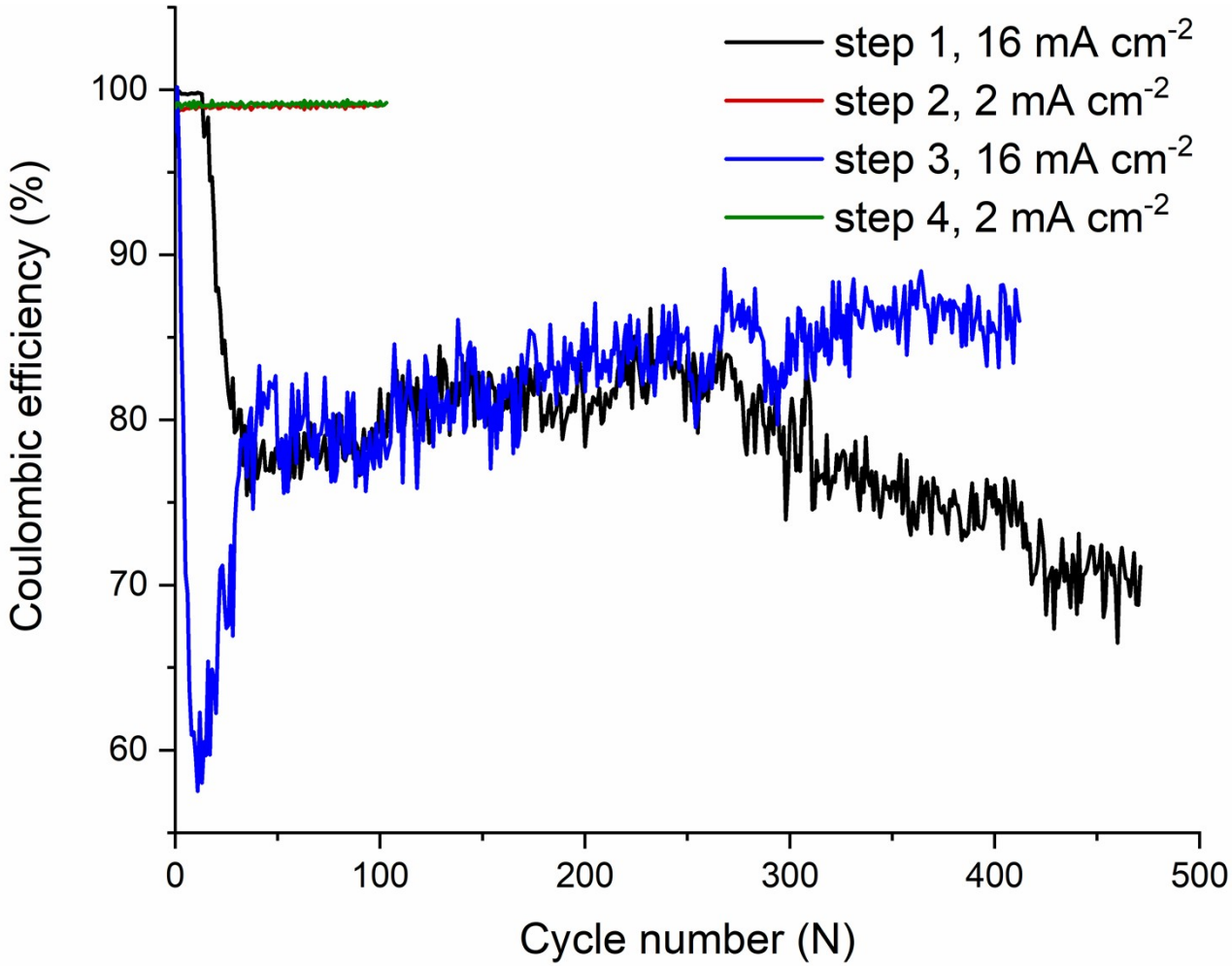

Figure S15 Coulombic efficiency in one RFB cell using the OS-NF-8800 membrane type. Between the steps, the RFB cycling regime was changed from the high current regime (galvanostatic at 16 mA cm^{-2}, mixed with potentiostatic) to the low current regime (galvanostatic at 2 mA cm^{-2}, mixed with potentiostatic) and back. Prior to each step, the membrane was replaced with a fresh one of the same type (OS-NF-8800). Between steps 1 and 2 the used anolyte was replaced with a fresh solution of the same volume to ensure equal testing conditions. The anolyte portion from step 2 was not replaced during the later testing, but additional 2 mL anolyte were added before step 3 and once more before step 4 in order to compensate for osmosis effect. Each of the steps was performed in the time frame of 5.5 to 6 days.

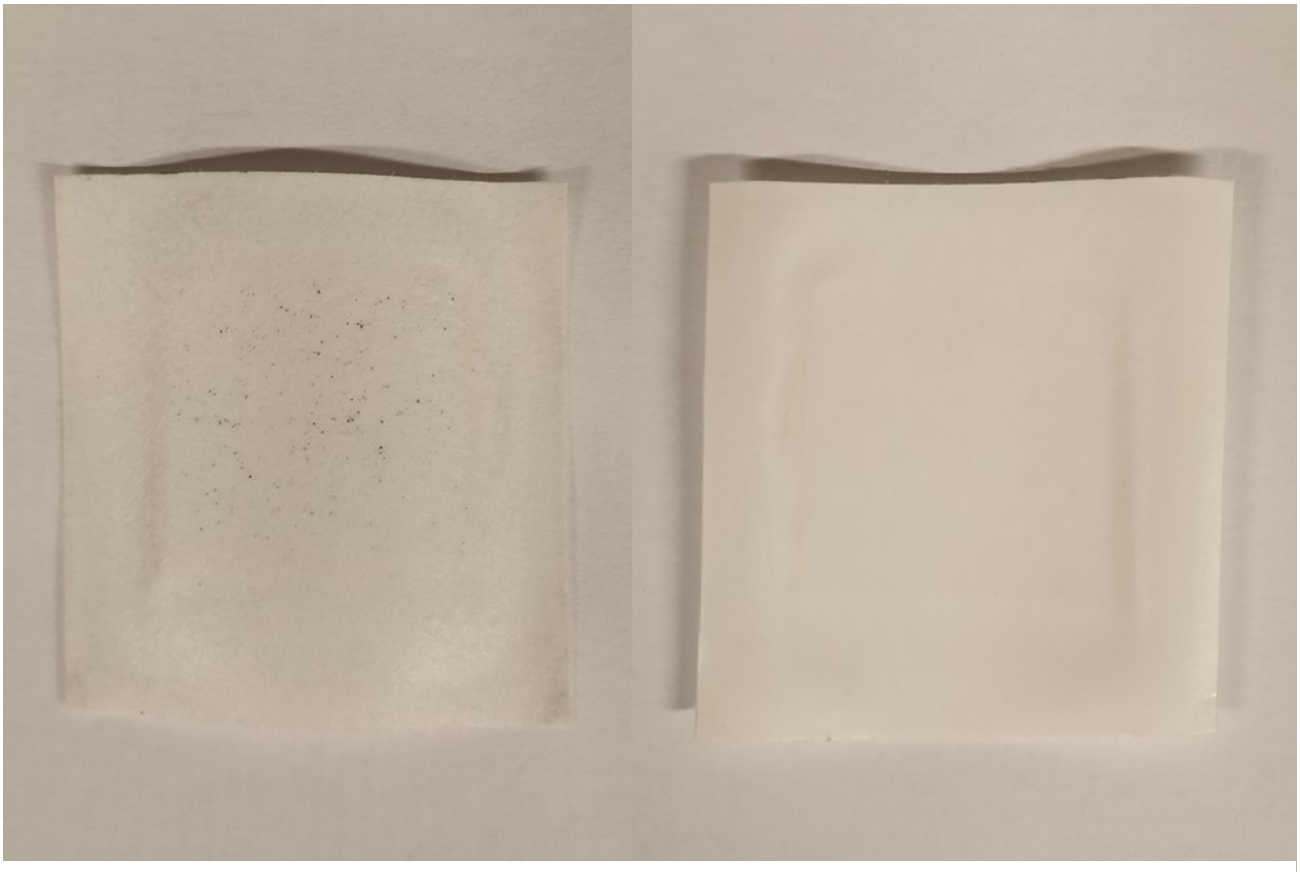

Figure S16 Photos of the PP and PES sides of the OS-NF-8800 membrane, respectively. The charge-discharge cycling was performed in the mixed galvanostatic-potentiostatic regime with 2 mA cm^{-2} fixed current, 0.5 and 1.5 V voltage cutoffs, and subsequent holding at the voltage cutoffs until the current decreased to ≤0.5 mA cm^{-2}. The PP side contacted the RFB anolyte and the PES layer faced the catholyte.

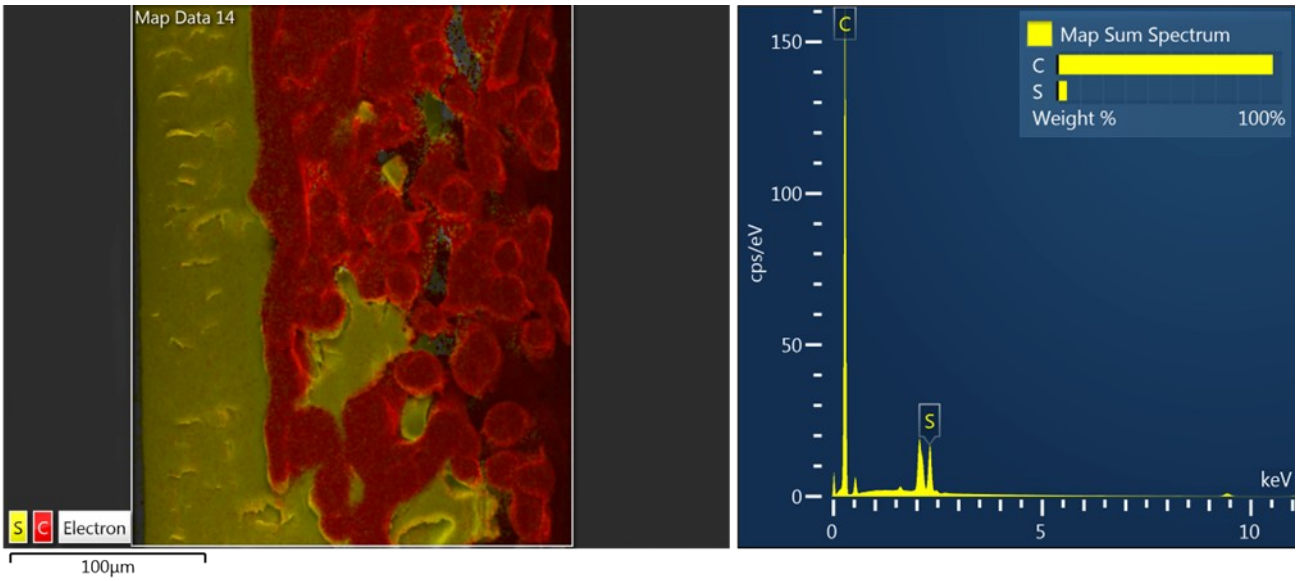

Figure S17 EDX scan of the cross-section of a pristine OS-NF-8800 membrane and the corresponding spectra. Sulphur-carbon coloration is applied. Magnification x200.

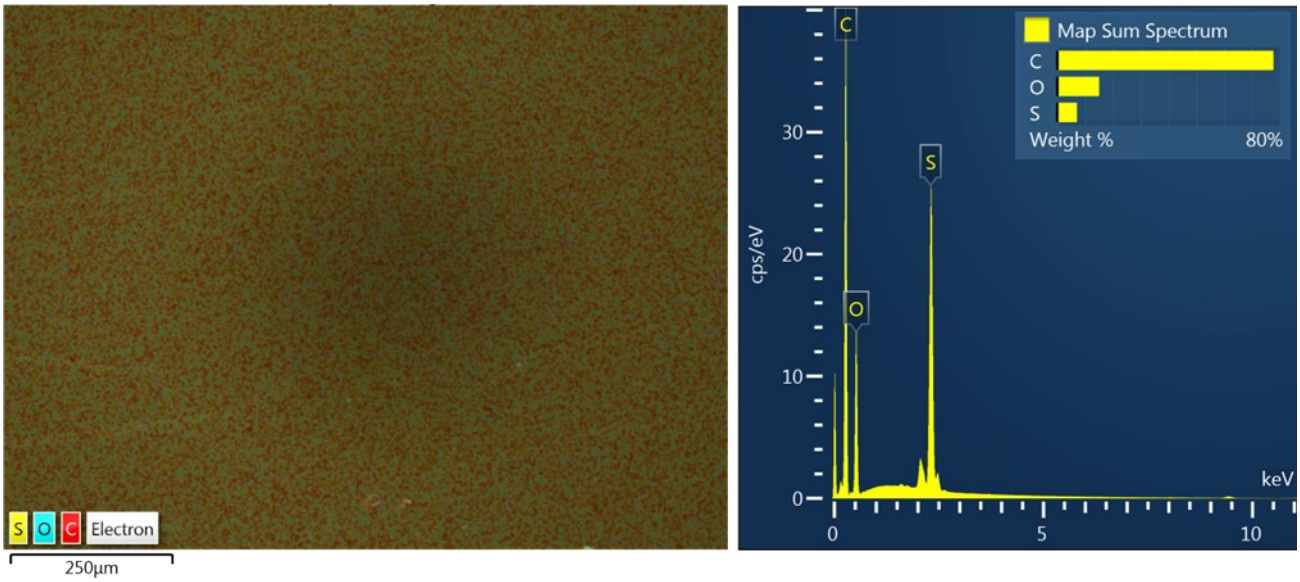

Figure S18 EDX scan of the front-side of a pristine OS-NF-8800 membrane and the corresponding spectra. Sulphur-oxygen-carbon coloration is applied. Magnification x100.

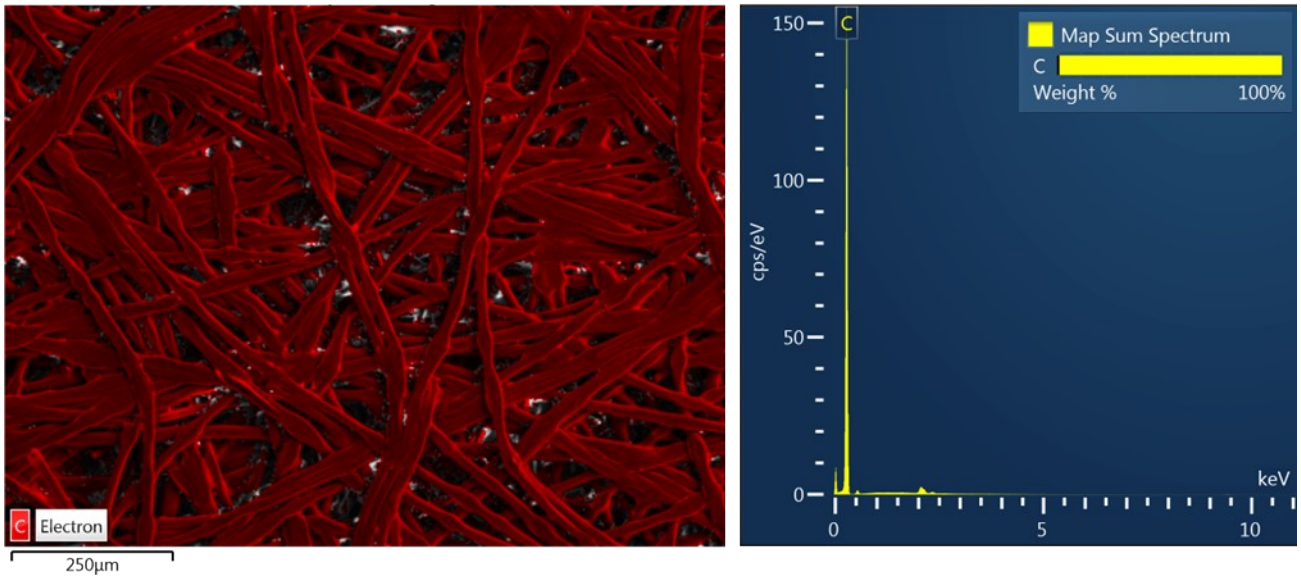

Figure S19 EDX scan of the back-side of a pristine OS-NF-8800 membrane and the corresponding spectra. Carbon coloration is applied. Magnification x100.

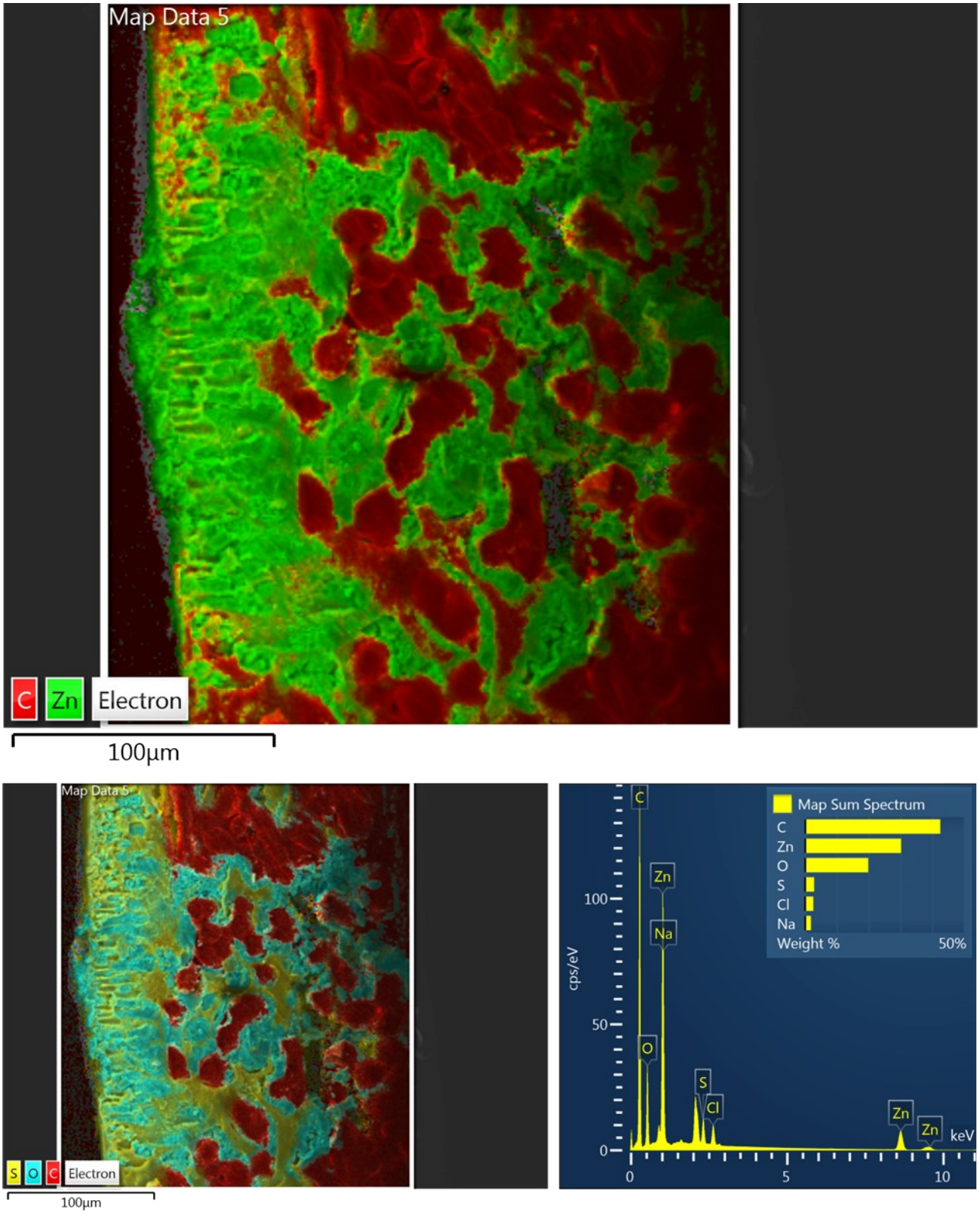

Figure S20 EDX scan of the cross-section of the OS-NF-8800 membrane after the RFB cycling in higher current regime and the corresponding spectra. Carbon-zinc and sulphur-oxygen-carbon colorations are applied. Magnification x200.

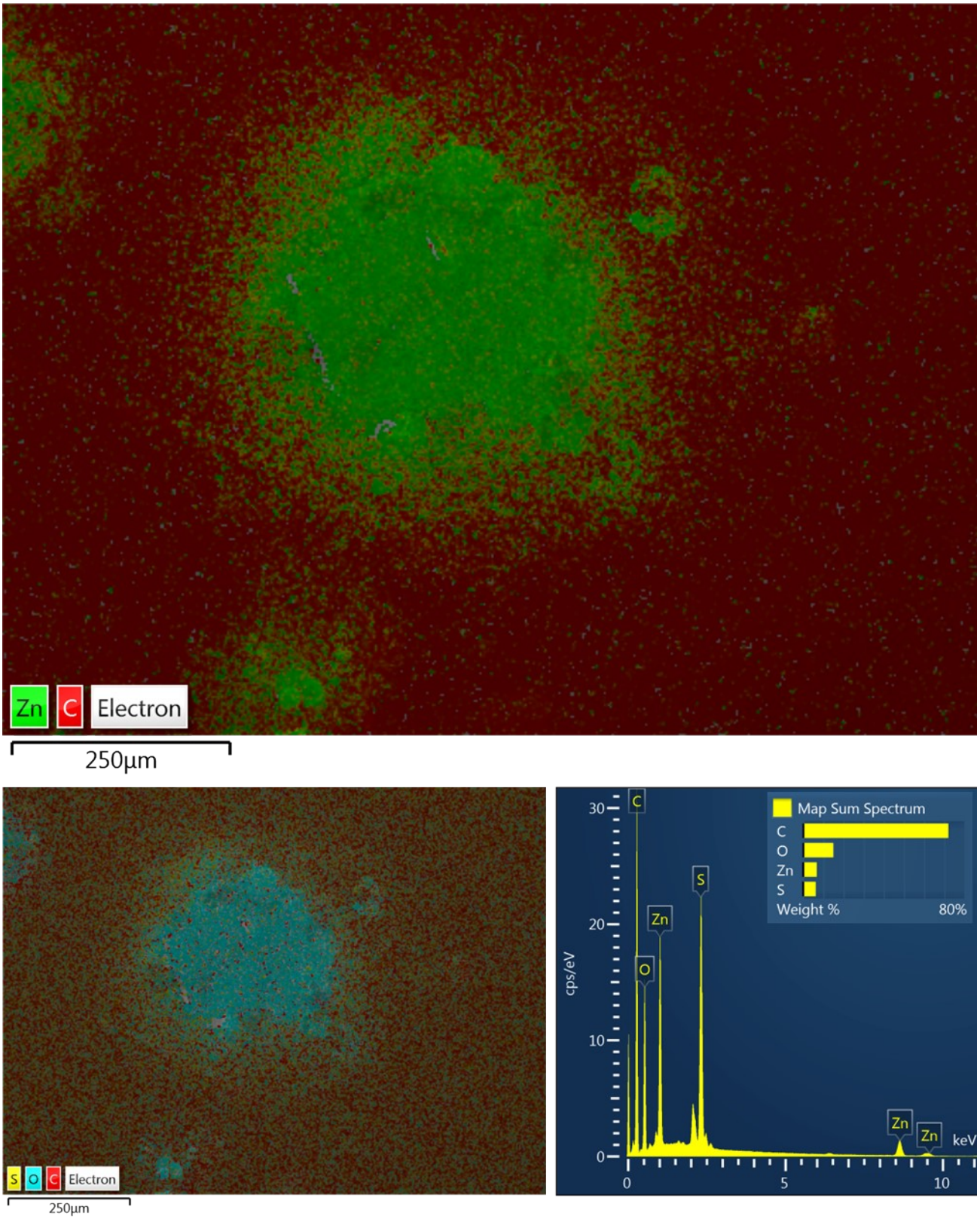

Figure S21 EDX scan of the front-side of the OS-NF-8800 membrane after the RFB cycling in higher current regime and the corresponding spectra. Carbon-zinc and sulphur-oxygen-carbon colorations are applied. Magnification x100.

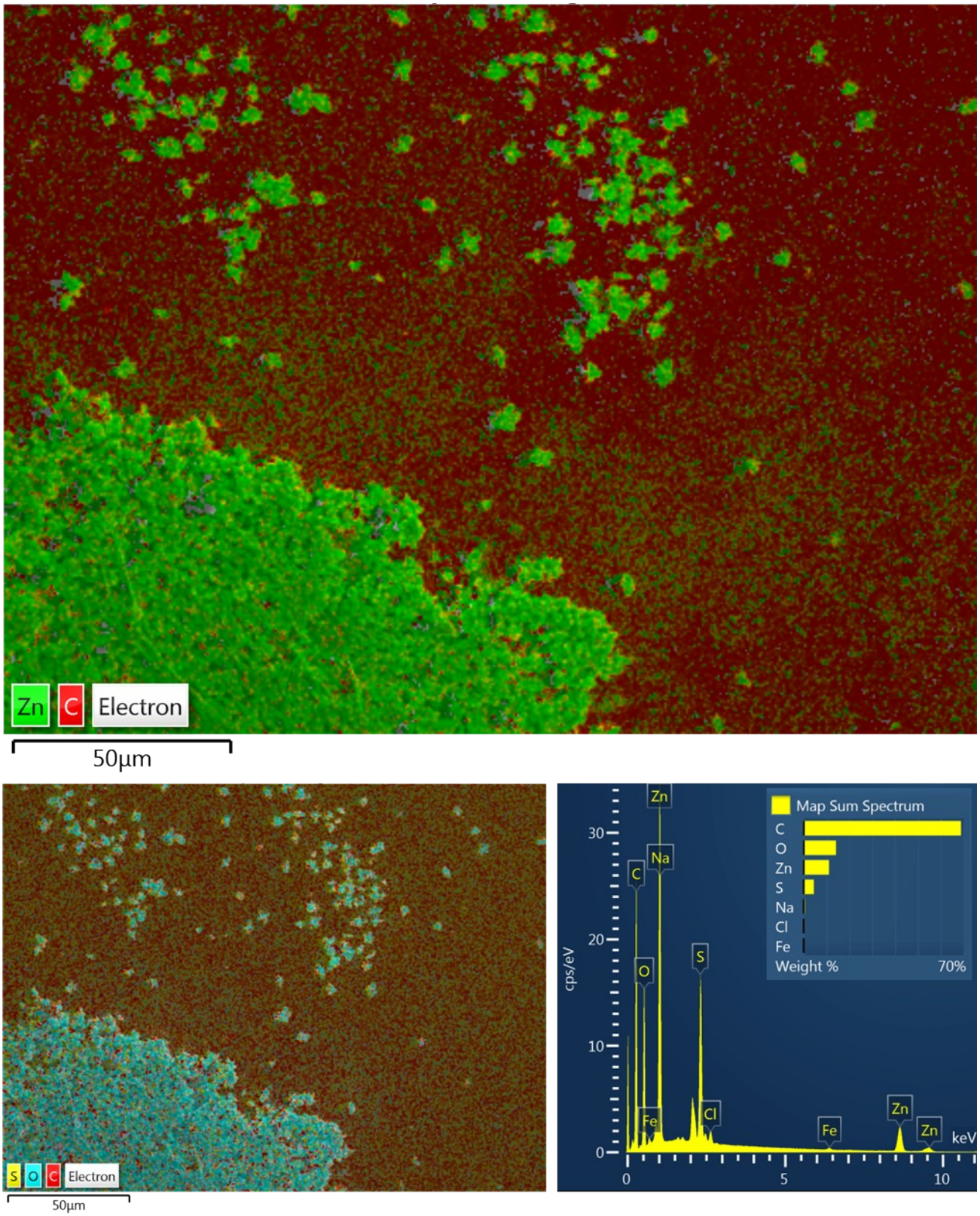

Figure S22 EDX scan of the front-side of the OS-NF-8800 membrane after the RFB cycling in higher current regime and the corresponding spectra. Carbon-zinc and sulphur-oxygen-carbon colorations are applied. Magnification x500.

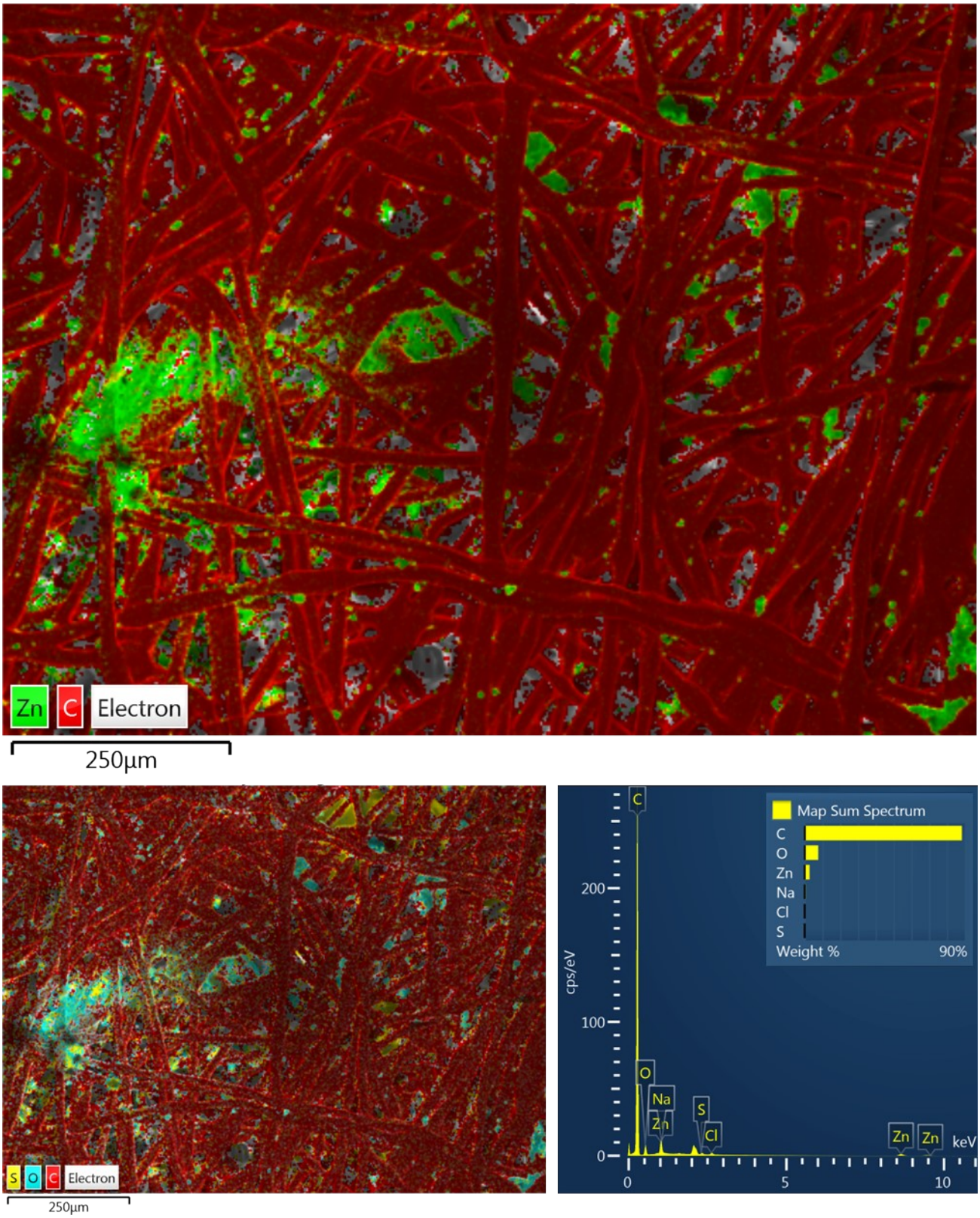

Figure S23 EDX scan of the back-side of the OS-NF-8800 membrane after the RFB cycling in higher current regime and the corresponding spectra. Carbon-zinc and sulphur-oxygen-carbon colorations are applied. Magnification x100.

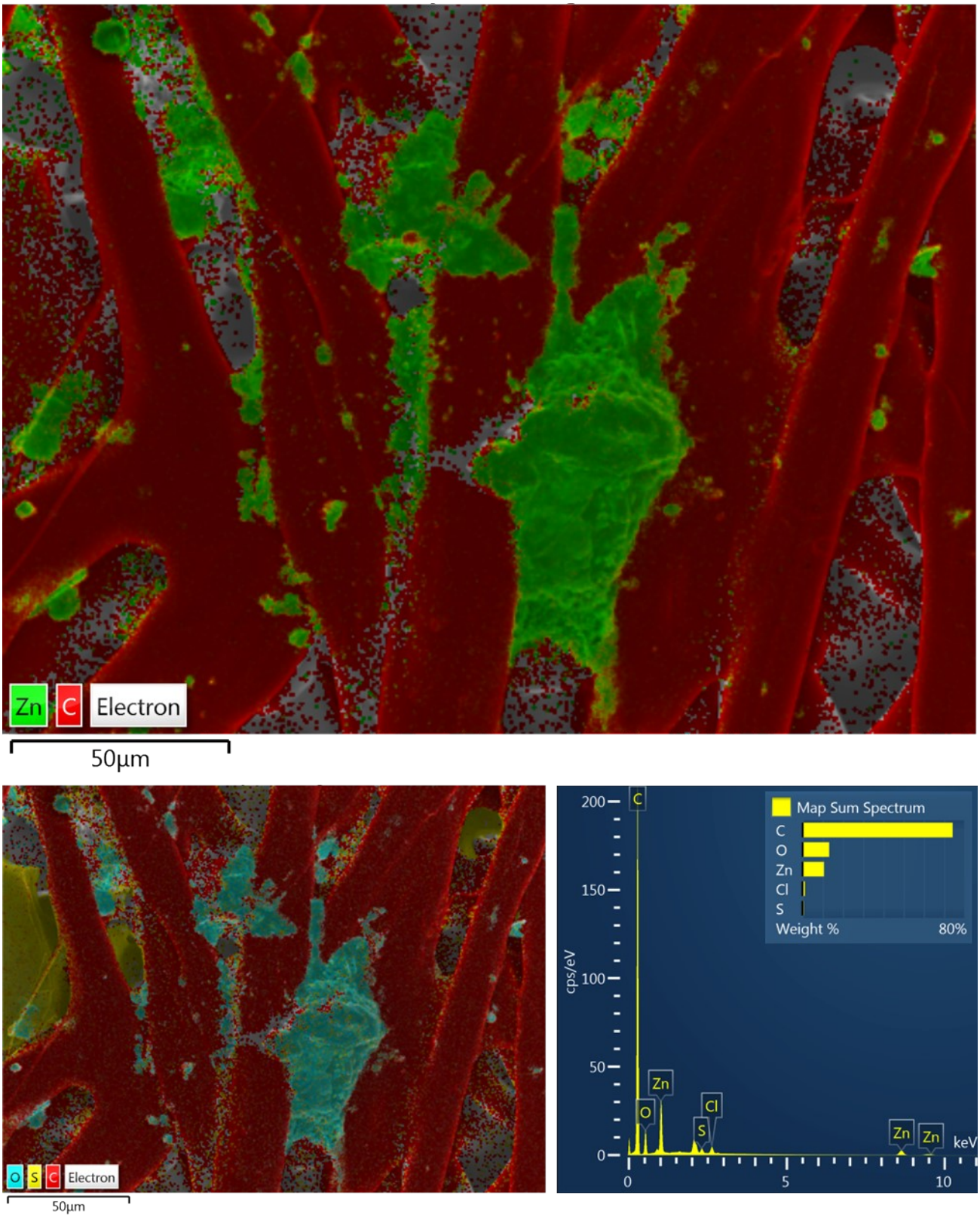

Figure S24 EDX scan of the back-side of the OS-NF-8800 membrane after the RFB cycling in higher current regime and the corresponding spectra. Carbon-zinc and sulphur-oxygen-carbon colorations are applied. Magnification x500.

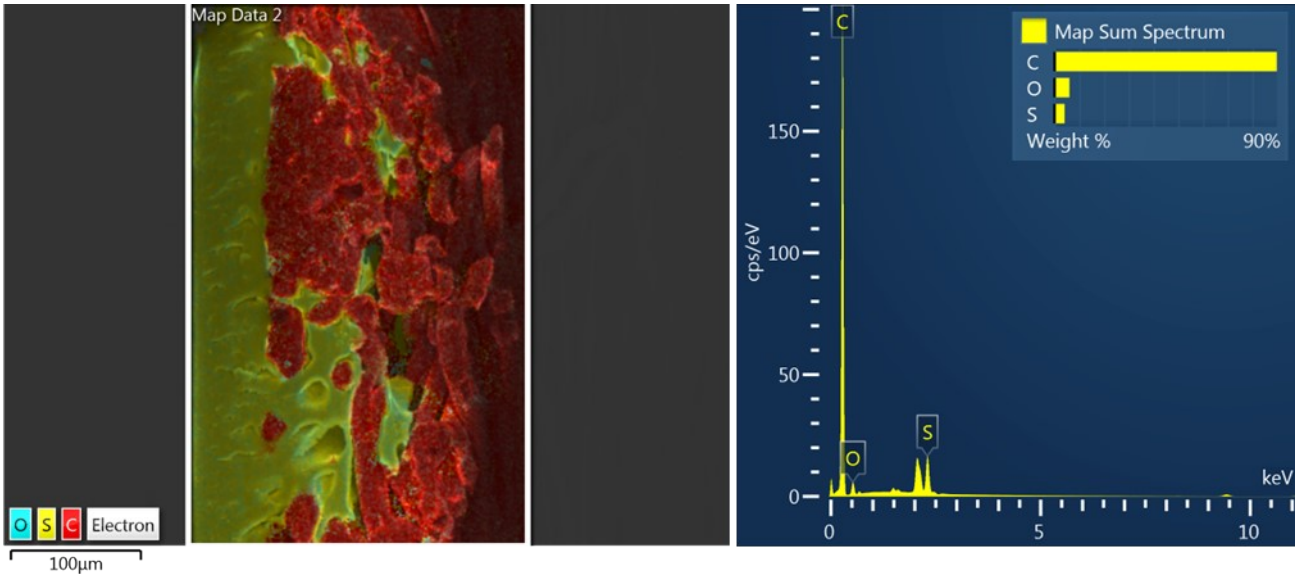

Figure S25 EDX scan of the cross-section of the OS-NF-8800 membrane after the RFB cycling in lower current regime and the corresponding spectra. Sulphur-oxygen-carbon coloration is applied. Magnification x200.

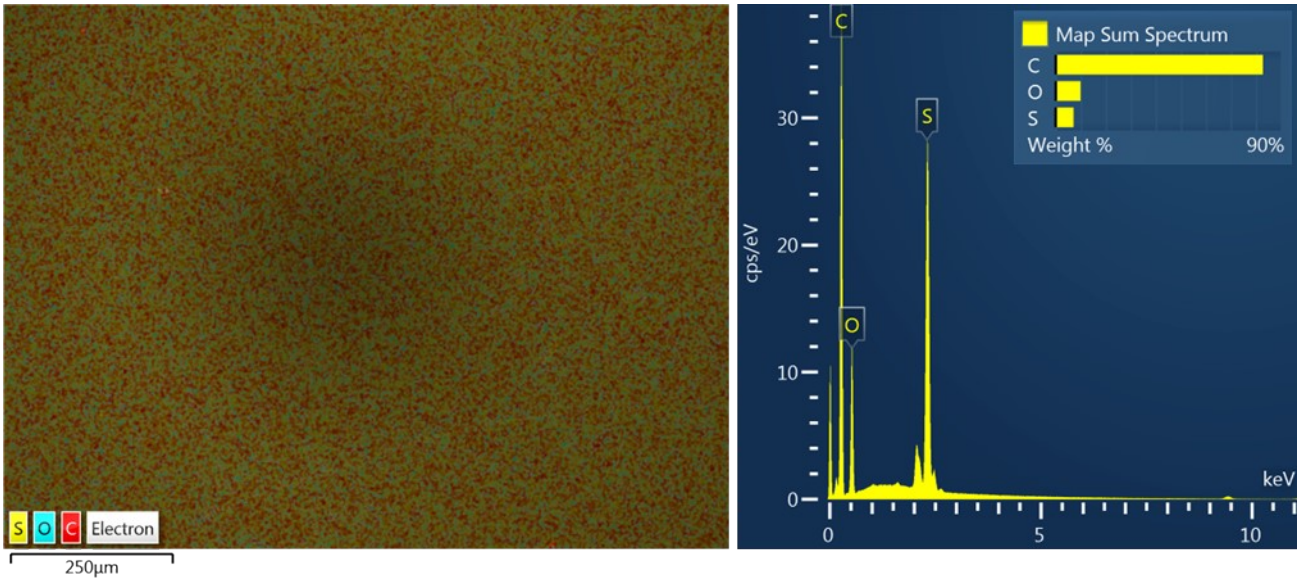

Figure S26 EDX scan of the front-side of the OS-NF-8800 membrane after the RFB cycling in lower current regime and the corresponding spectra. Sulphur-oxygen-carbon coloration is applied. Magnification x100.

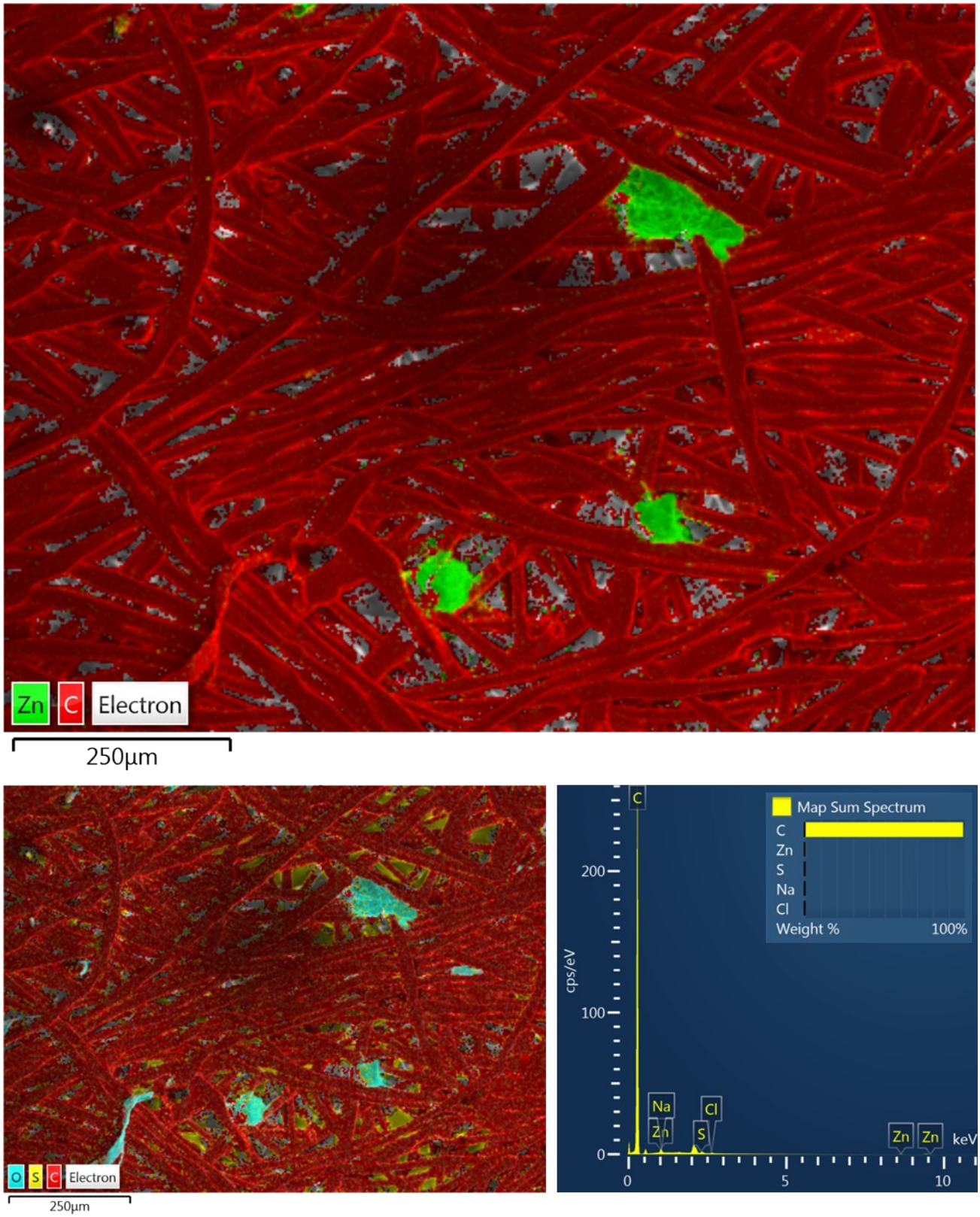

Figure S27 EDX scan of the back-side of the OS-NF-8800 membrane after the RFB cycling in lower current regime and the corresponding spectra. Carbon-zinc and sulphur-oxygen-carbon colorations are applied. Magnification x100.

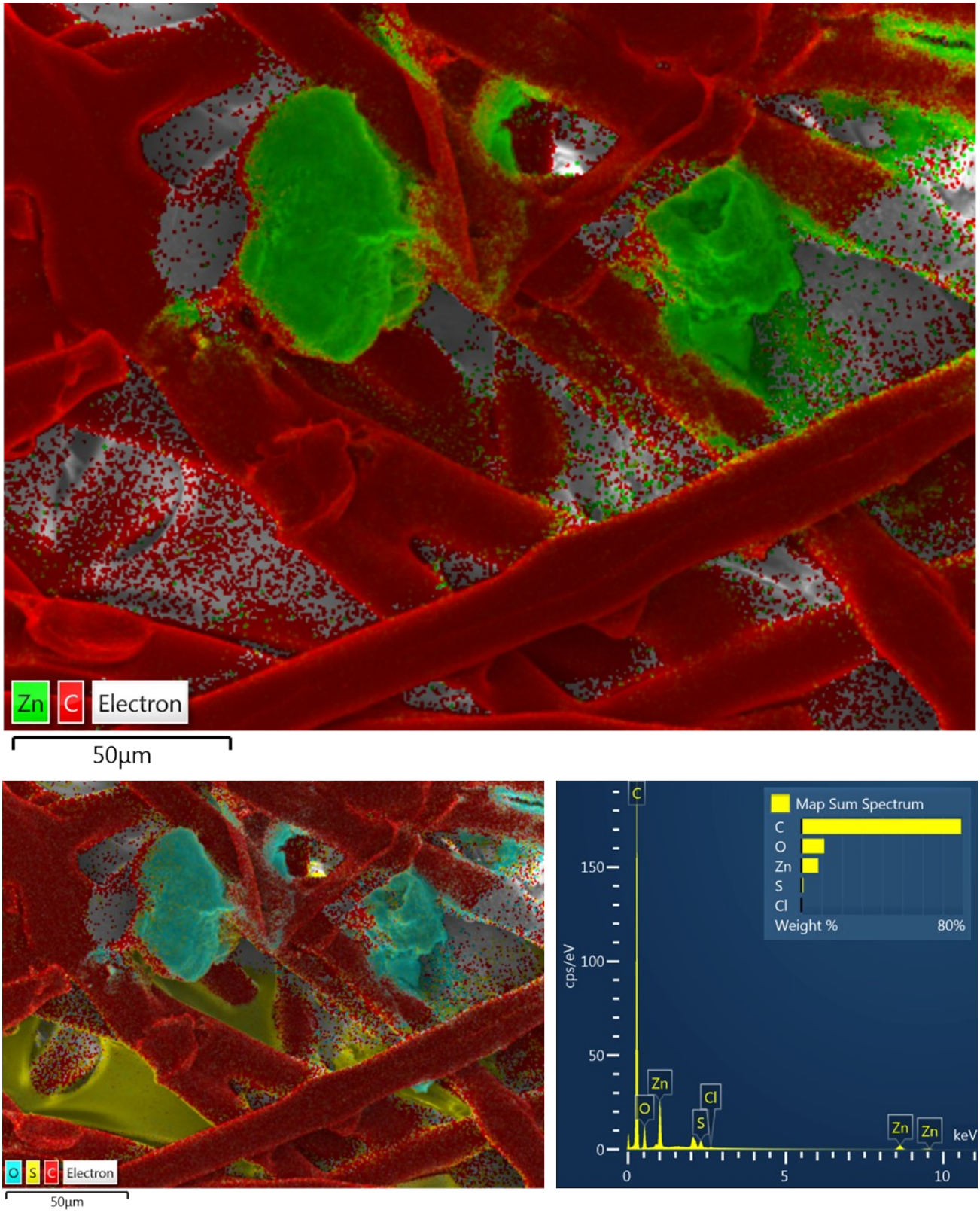

Figure S28 EDX scan of the back-side of the OS-NF-8800 membrane after the RFB cycling in lower current regime and the corresponding spectra. Carbon-zinc and sulphur-oxygen-carbon colorations are applied. Magnification x500.

Exemplary curves from the RFB tests in lower current cycling regime

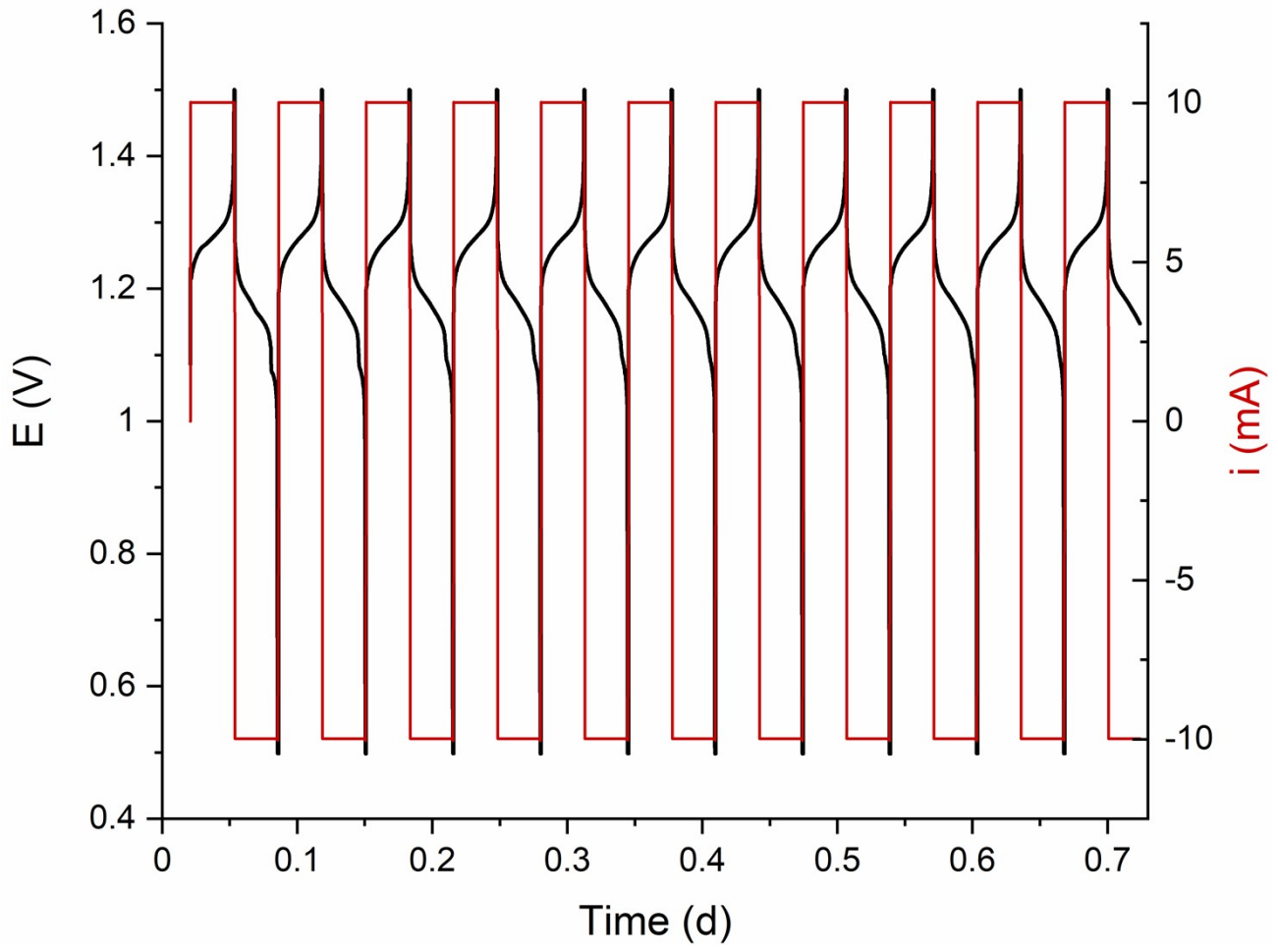

Figure S29 Exemplary RFB charge/discharge procedure, where galvanostatic regime at 2 mA cm^{-2} is mixed with potentiostatic holding at voltage cutoffs of 0.5 and 1.5 V till the current density decreases to ≤0.5 mA cm^{-2}. Since the current density in the galvanostatic part is already relatively low, the potentiostatic part requires significantly less time to complete the charge/discharge and, consequently, only the galvanostatic part may be recognised from the plot.

UV-Vis calibration for PFc containing solutions

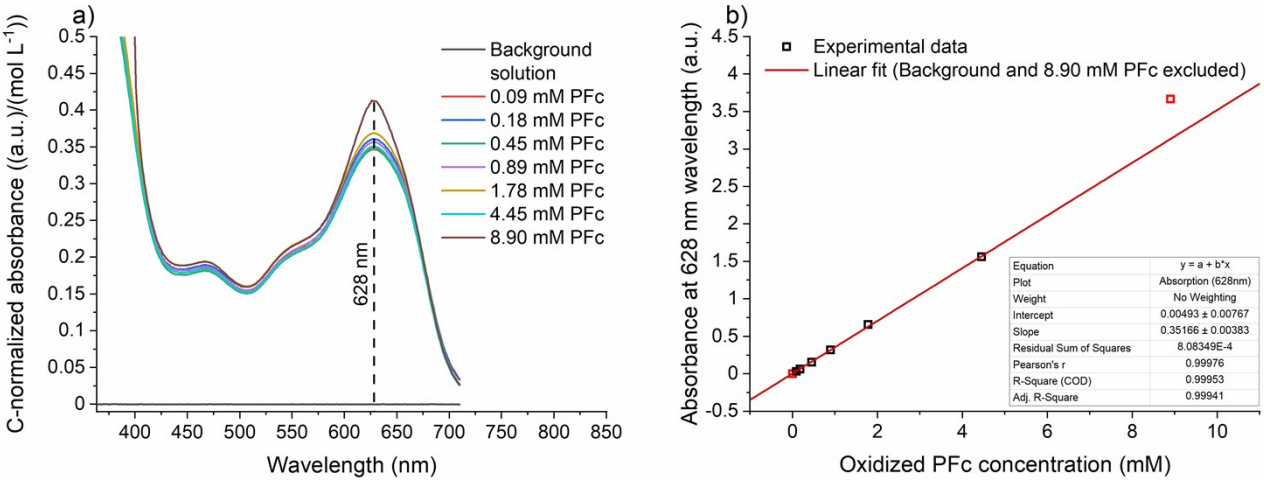

Figure S30 a) Normalized by PFc concentration absorbance of charged PFc in a 0.1 M $ZnCl_2$, 0.8 M NH_4Cl solution. b) Calibration curve for the absorbances of measured samples at 628 nm wavelength. The 8.90 mM PFc sample was excluded from the linear fit equation due to concentration effects detected at Figure S30a. Background solution sample was not used during preparation of the linear regression to avoid its influence on the linear fit and to further use it as a fit a quality control value.

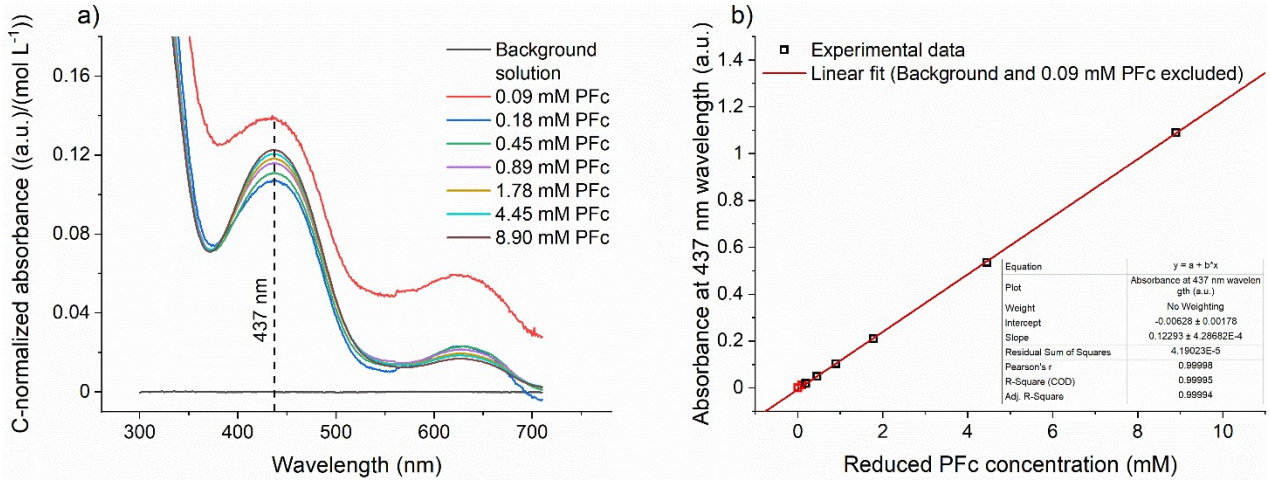

Figure S31 a) Absorbance of uncharged PFc in a 0.1 M $ZnCl_2$, 0.8 M NH_4Cl aqueous solution normalized by PFc concentration in each sample. b) Calibration curve for the absorbances of measured samples at 437 nm wavelength. The 0.09 mM PFc sample was excluded from the linear fit due to a wrong sample preparation detected at Figure S31a. Background solution sample was not used during preparation of the linear regression to avoid its influence on the linear fit and to further use it as a fit a quality control value.

Cross-over evaluation in the NH_4Cl-based electrolytes

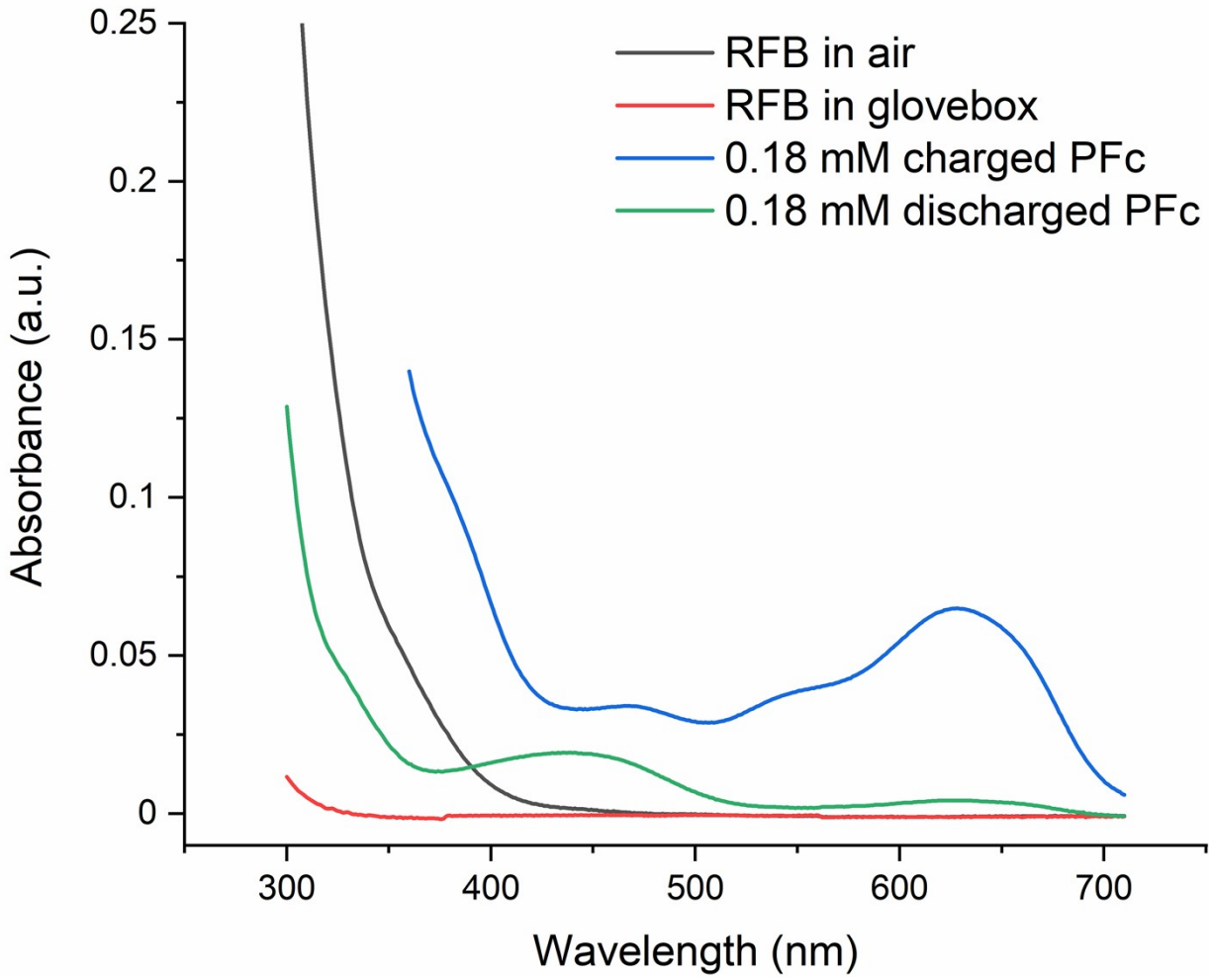

Figure S32 *Post mortem* cross-over studies of RFB anolytes after cycling in air and in a glovebox by UV-Vis spectroscopy. The 0.18 mM PFc solutions, corresponding to the theoretical 0.67% cross-over of the 27 mM PFc catholyte, were depicted on the Figure for comparison, while their spectra are taken in the non-normalized form from the data used for Figures S30a and S31a.

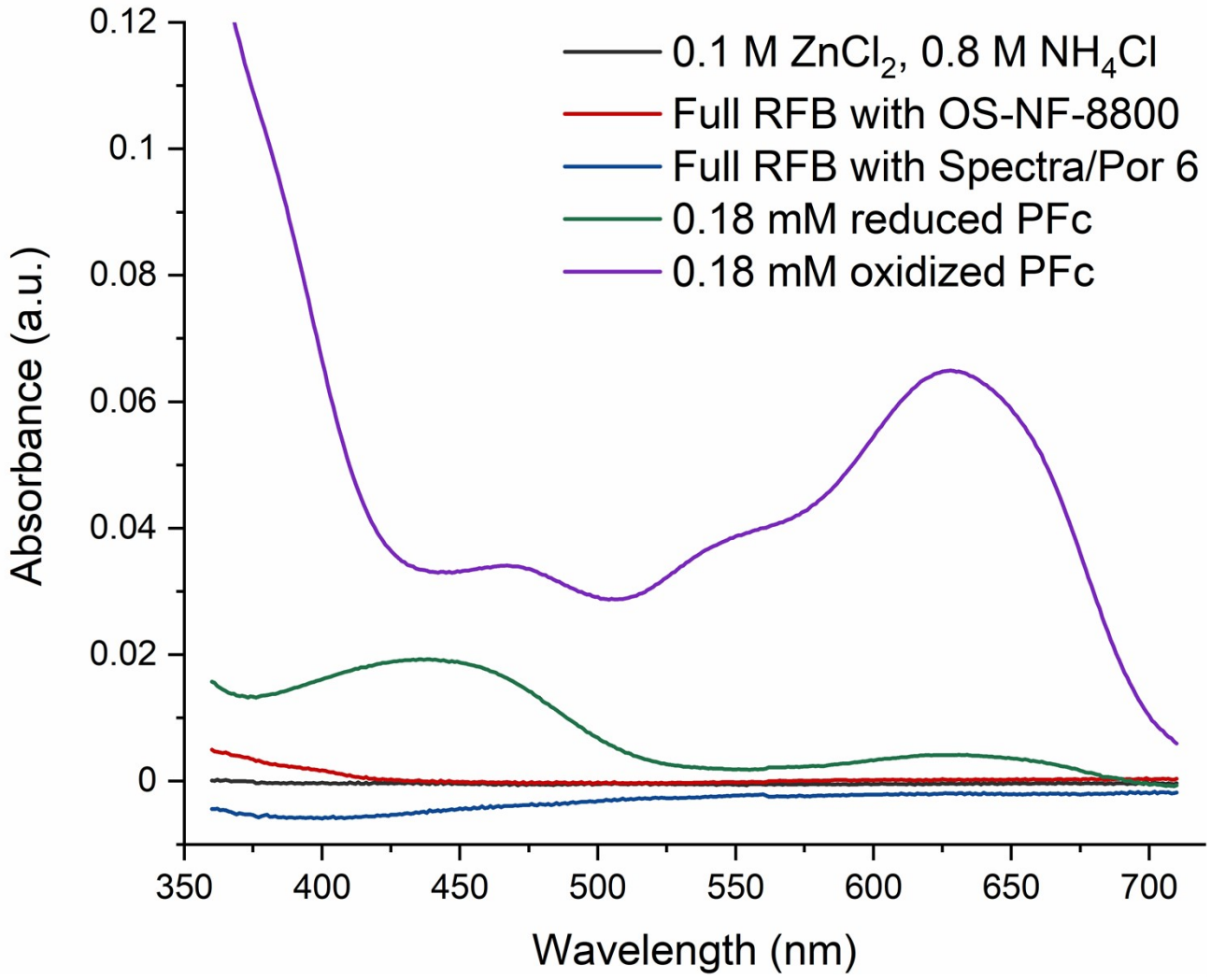

Figure S33 *Post mortem* cross-over analysis in the NH_4Cl-based anolytes by UV-Vis absorption spectroscopy. The samples were taken from RFBs using Spectra/Por 6 and OS-NF-8800 membranes. The 0.18 mM PFc solutions, corresponding to the theoretical 0.67% cross-over of the 27 mM PFc catholyte, were depicted on the Figure for comparison, while their spectra are taken in the non-normalized form from the data used for Figures S30a and S31a. Thus, the absorption of the 0.18 mM PFc samples was measured in solutions based on the 0.1 M $ZnCl_2$, 0.8 M NH_4Cl electrolyte.

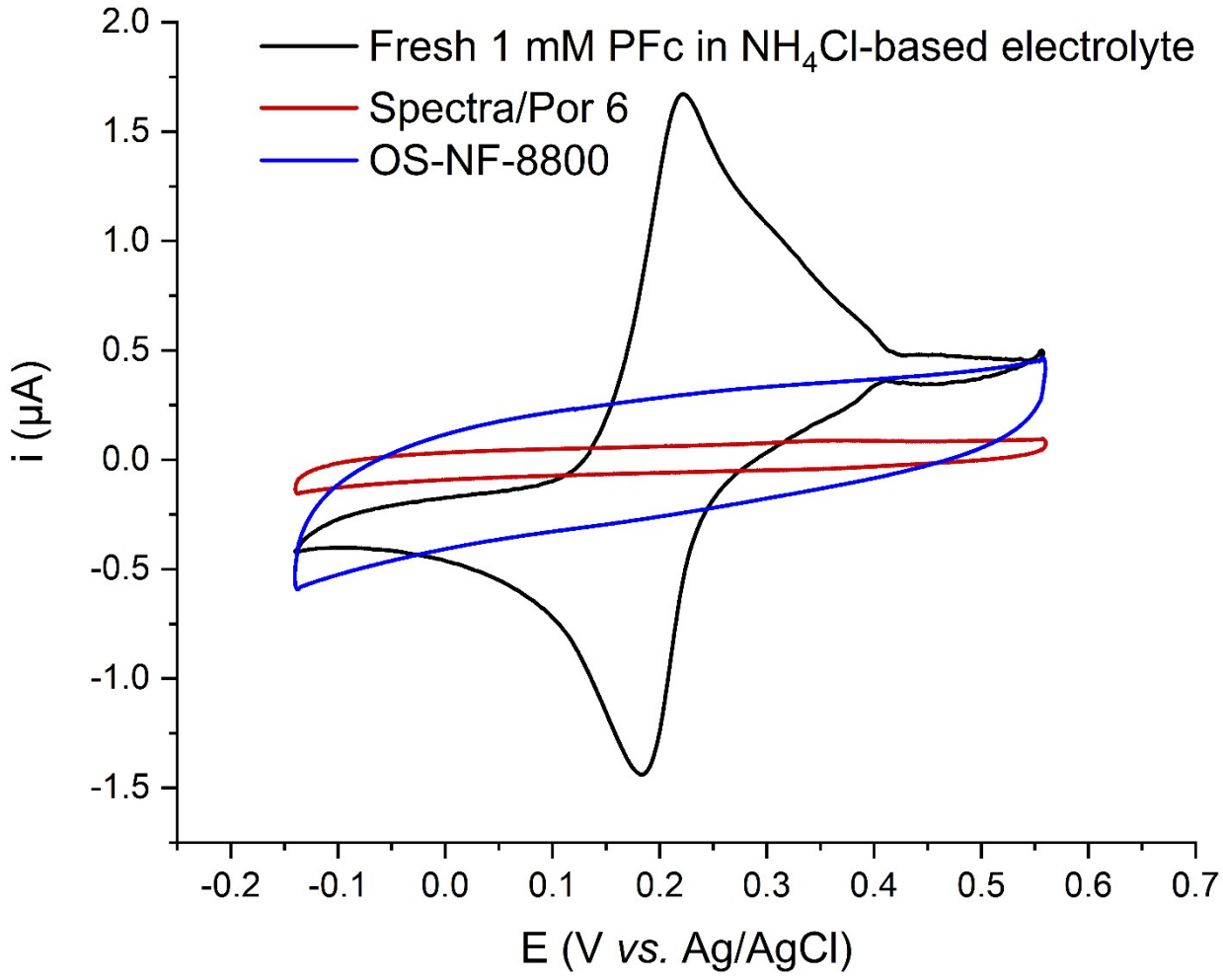

Figure S34 *Post mortem* cross-over assessment in the NH_4Cl-based anolytes by cyclic voltammetry. The samples were taken from RFBs using Spectra/Por 6 and OS-NF-8800 membranes. The 1 mM PFc solution, corresponding to the theoretical 3.7% cross-over of the 27 mM PFc catholyte, was depicted on the Figure for comparison, while its CV is taken from the data used for Figure 1 in the Results and Discussion, Subsection 3.1.1. Thus, the CV of 1 mM PFc sample was measured in solution, based on the 0.1 M $ZnCl_2$, 0.8 M NH_4Cl electrolyte.

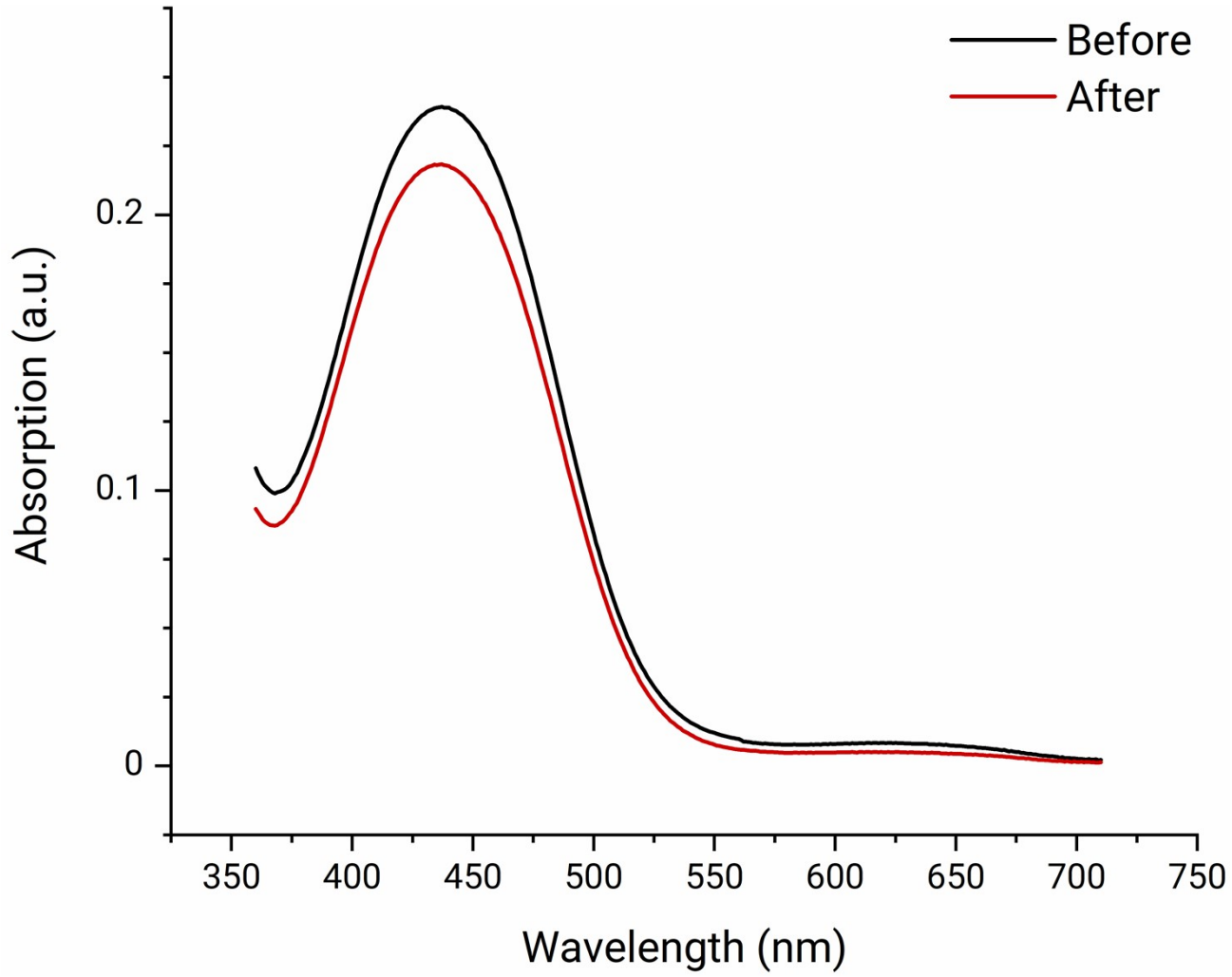

Figure S35 UV-Vis absorption of the RFB anolyte with intentionally dissolved PFc before and after the full RFB cycling.

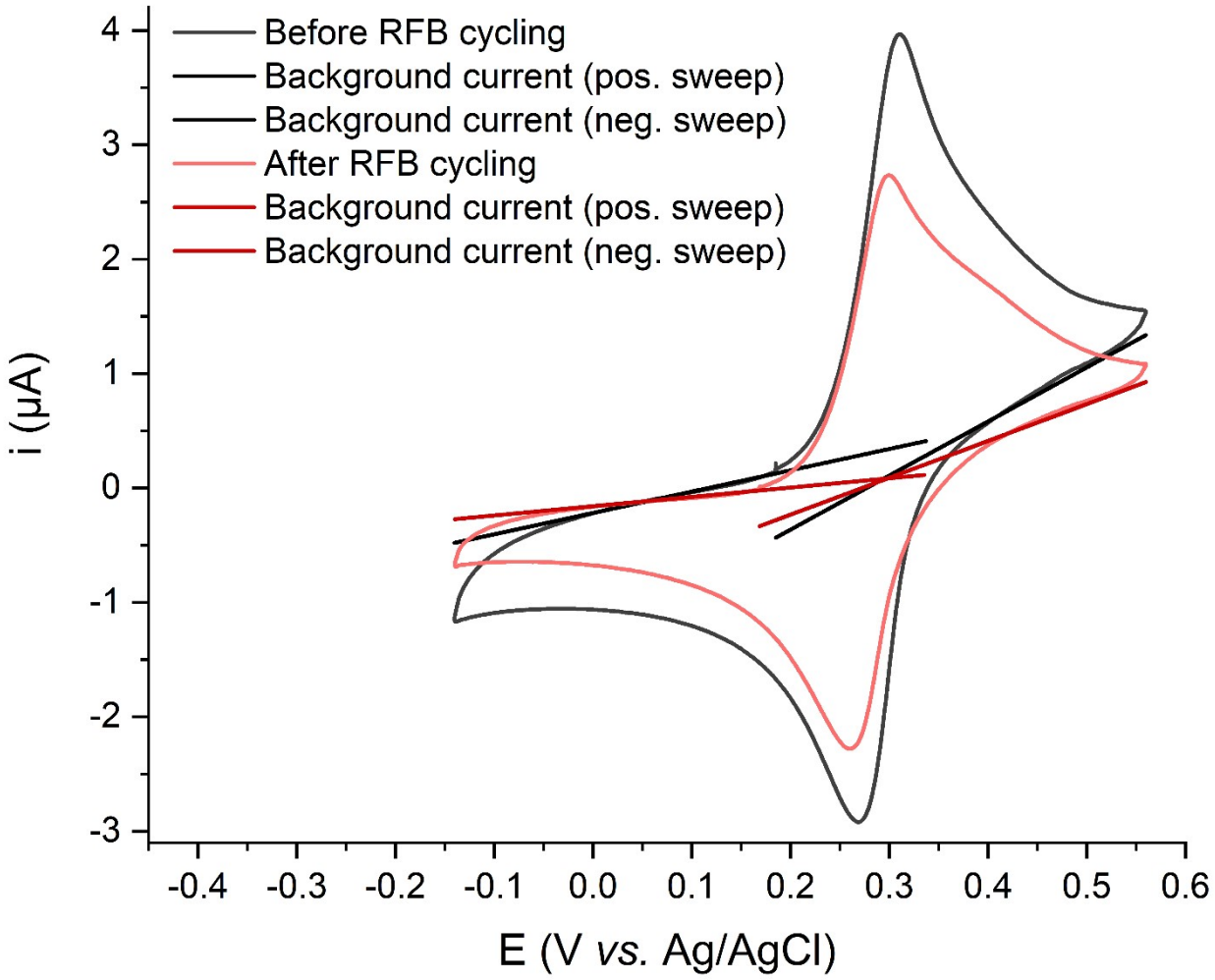

Figure S36 CV of the RFB anolyte with intentionally dissolved PFc before and after the full RFB cycling.

Electrospray ionization mass spectrometry

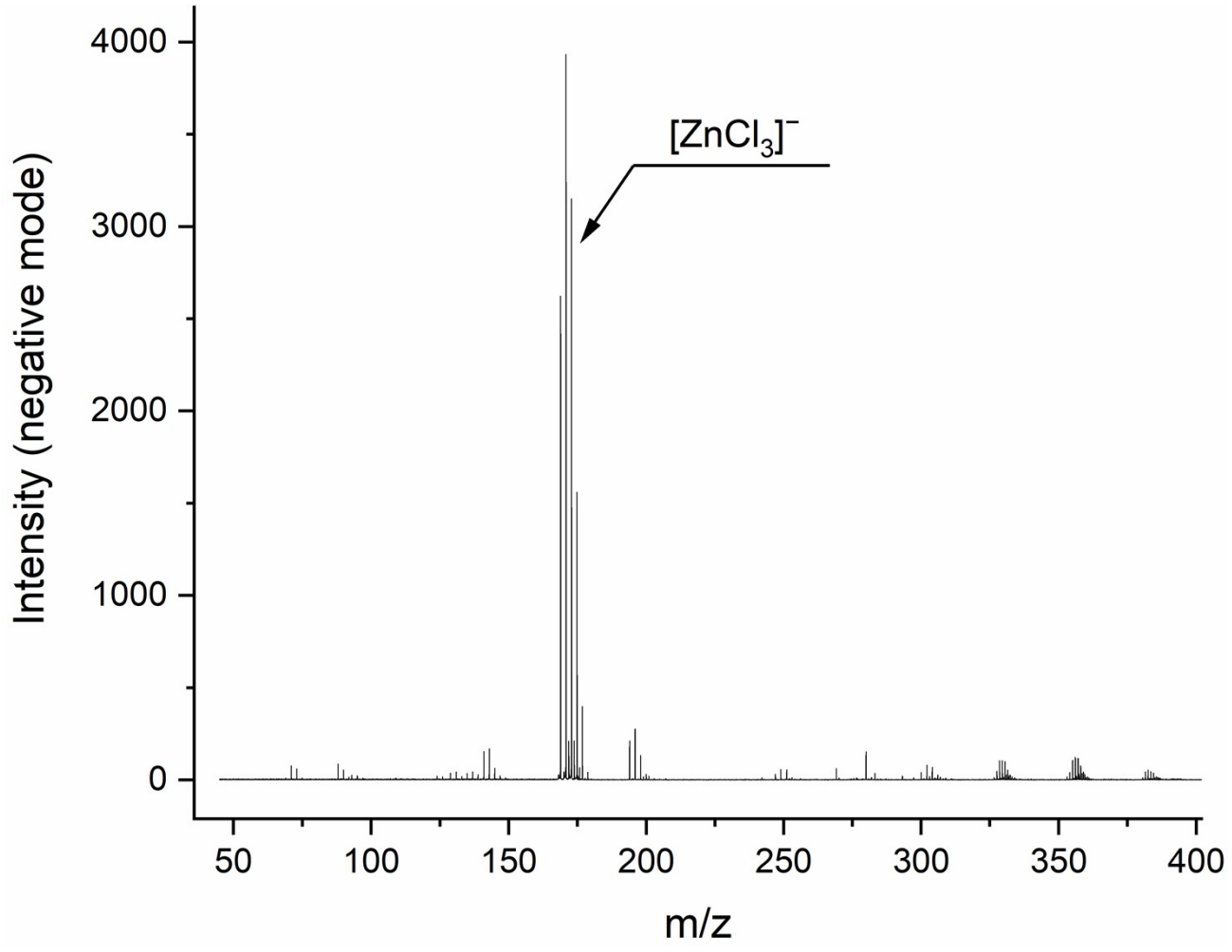

Figure S37 Negative spectra from the ESI-MS analysis of the *post mortem* anolyte 0.1 M $ZnCl_2$, 0.8 M NH_4Cl from the full RFB utilizing a OS-NF-8800 membrane and cycled for 5.7 days. The strongest signal corresponds to $ZnCl_3^-$ complex.

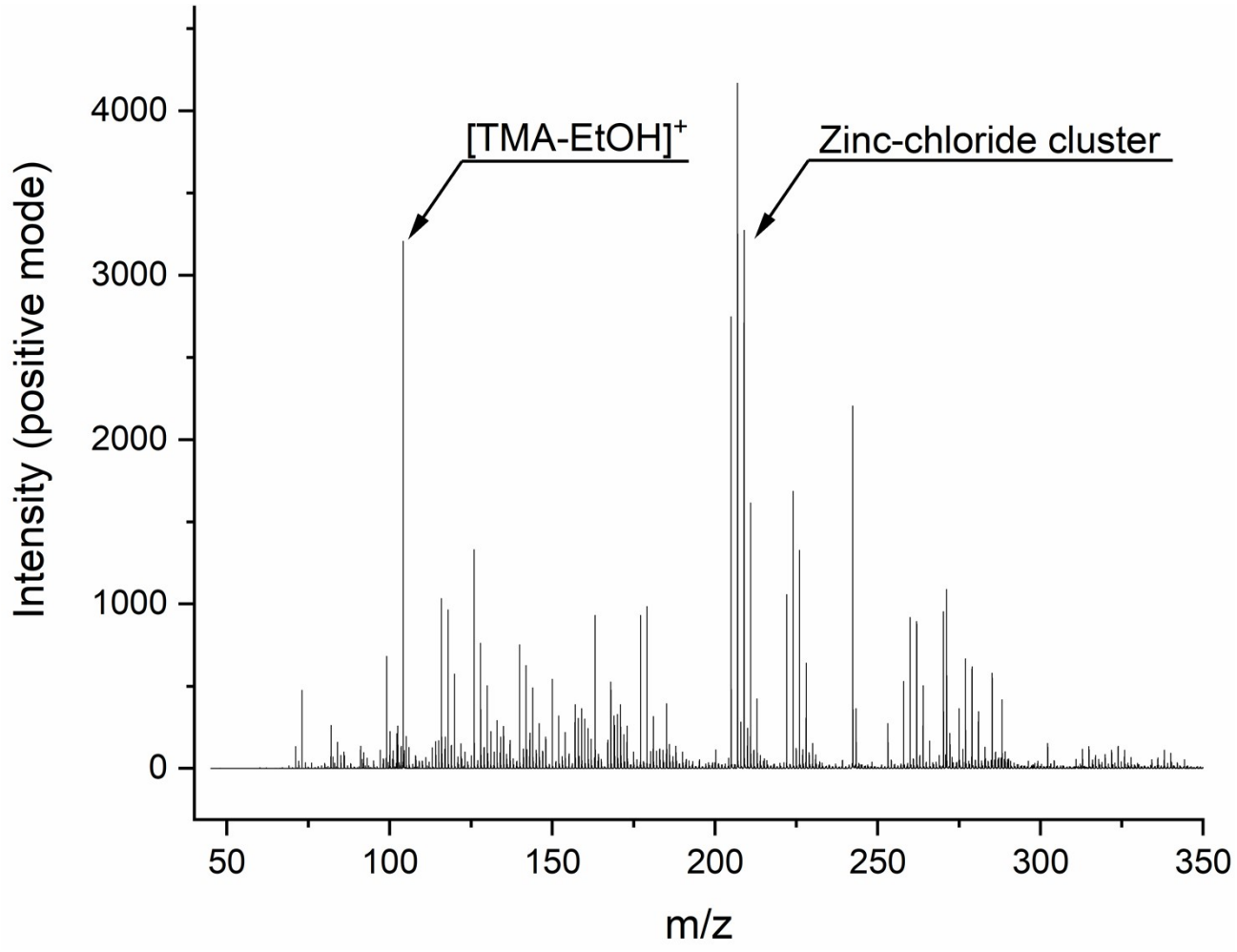

Figure S38 Positive spectra from the ESI-MS analysis of the *post mortem* anolyte 0.1 M $ZnCl_2$, 0.8 M NH_4Cl from the full RFB utilizing an OS-NF-8800 membrane and cycled for 5.7 days. The TMA-EtOH signal is clearly defined. According to the isotopic pattern, the strongest signal corresponds to a cluster, including zinc and chloride ions, though, it was not possible to determine a defined structure.

Cyclic voltammetry of the PFc in the newly applied tetramethylammonium-based electrolyte

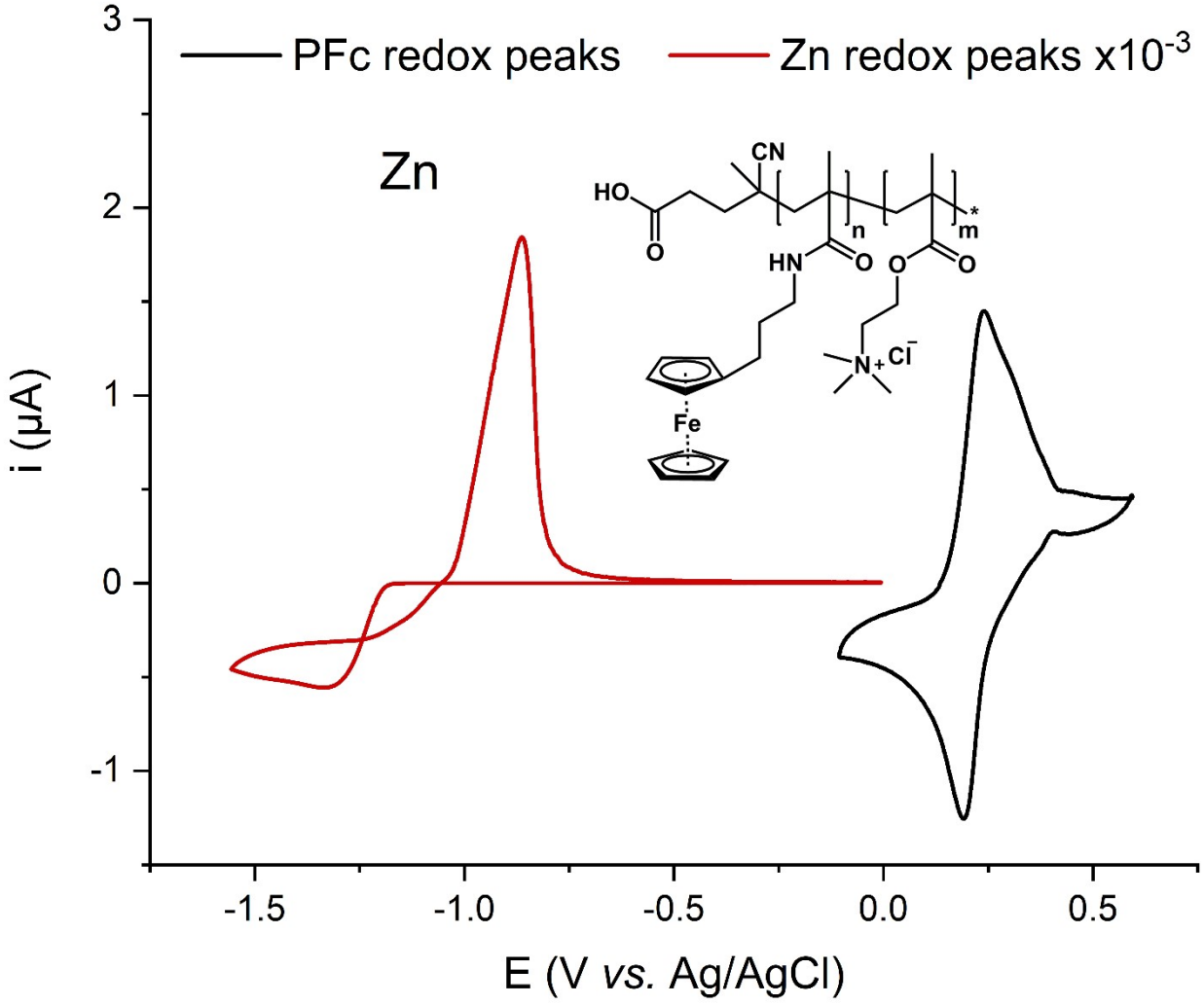

Figure S39 Cyclic voltammetry at 100 mV s^{-1} of zinc and 1 mM PFc *vs.* Ag/AgCl reference electrode as well as schematic representation of the polymer structure. Supporting electrolyte is 0.1 M $ZnCl_2$, 0.8 M TMACl, 6 mM HCl, pH 4.5-5 aqueous solution.

Cross-over evaluation in the TMACl-based electrolytes

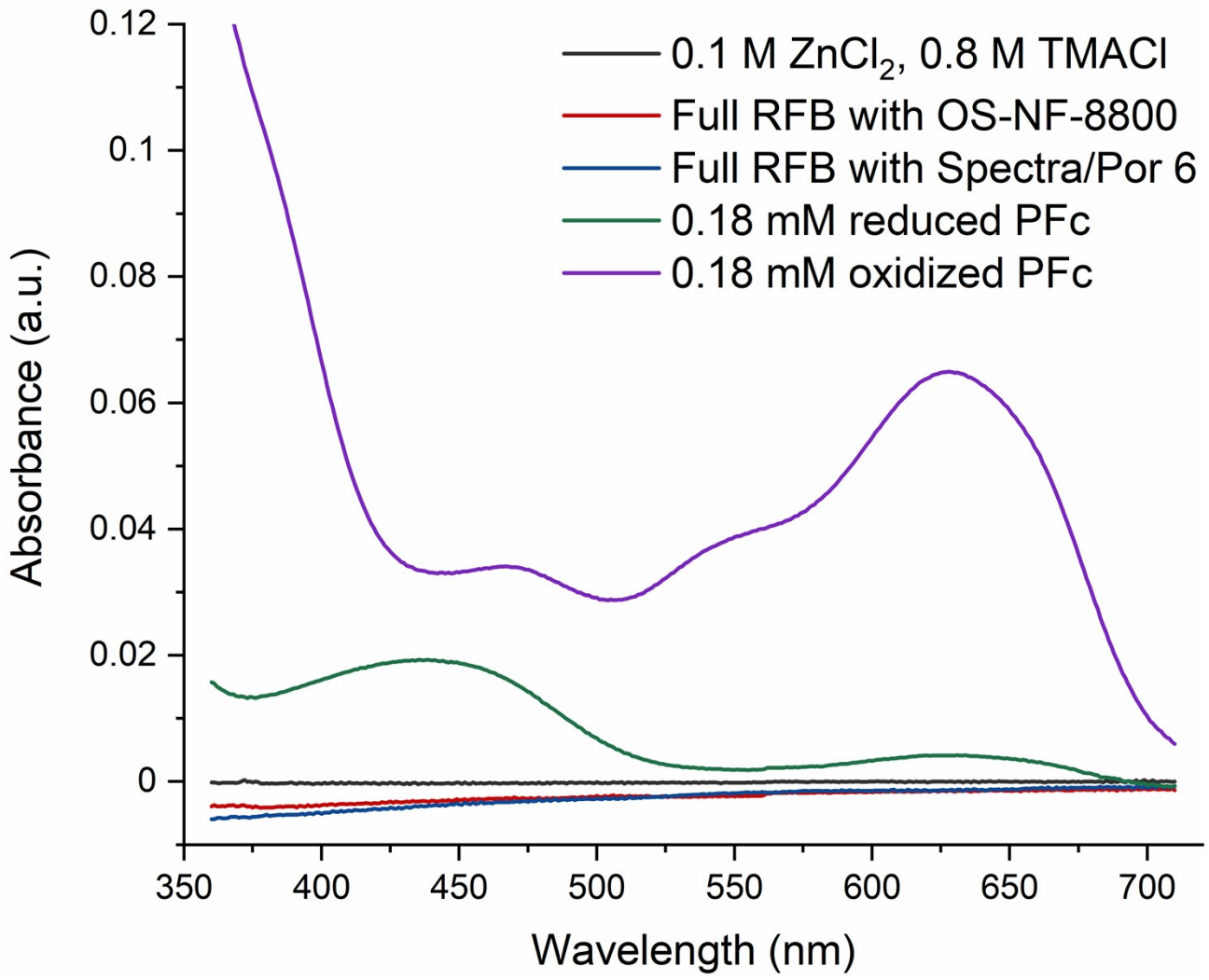

Figure S40 *Post mortem* cross-over assessment in the TMACl-based anolytes by UV-Vis absorption spectroscopy. The samples were taken from RFBs using Spectra/Por 6 and OS-NF-8800 membranes. The 0.18 mM PFc solutions, corresponding to the theoretical 0.67% cross-over of the 27 mM PFc catholyte, were depicted on the Figure for comparison, while their spectra are taken in the non-normalized form from the data used for Figures S30a and S31a. Thus, the absorption of the 0.18 mM PFc samples was measured in solutions based on the 0.1 M $ZnCl_2$, 0.8 M NH_4Cl electrolyte.

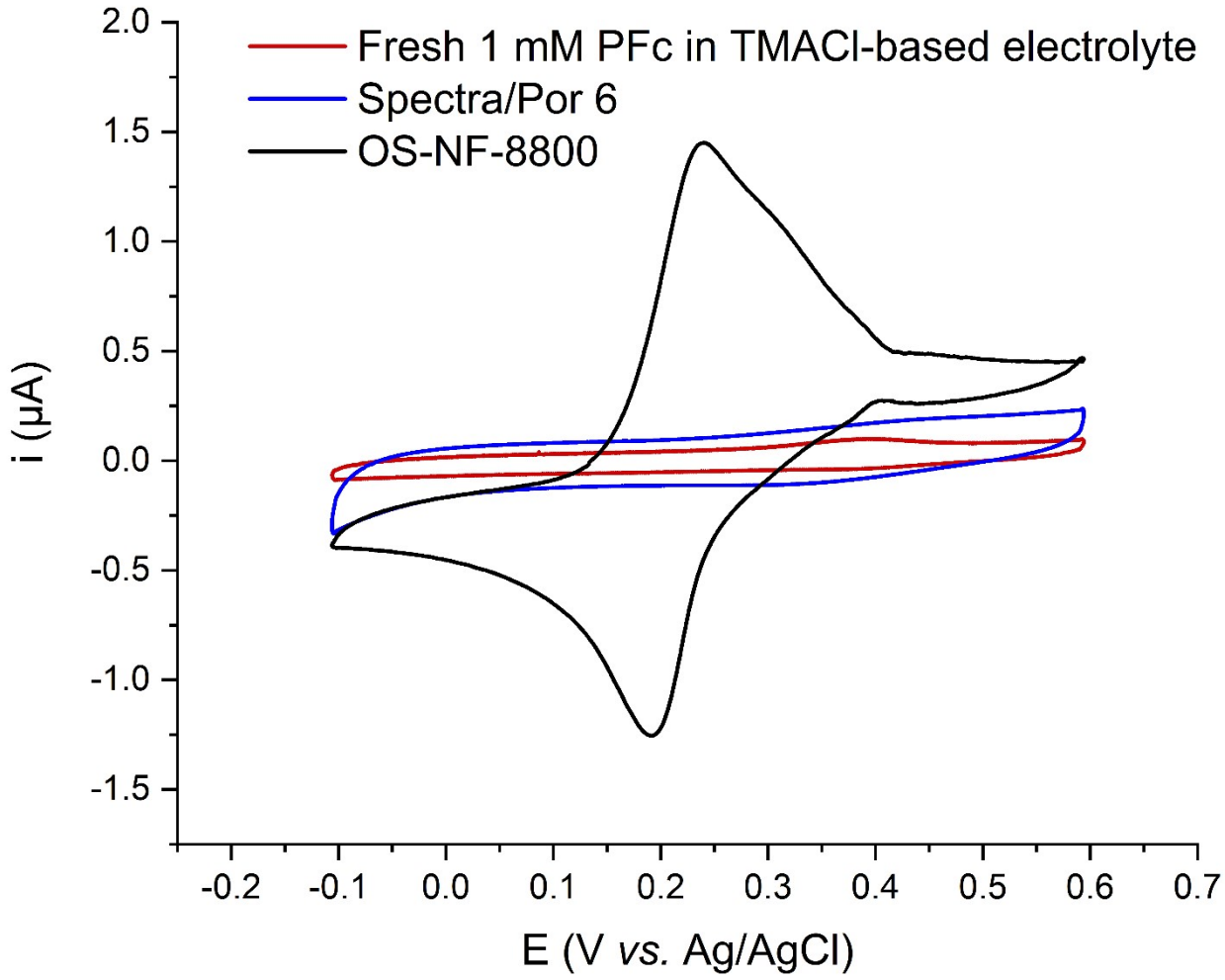

Figure S41 *Post mortem* cross-over assessment in the TMACl-based anolytes by cyclic voltammetry. The samples were taken from RFBs using Spectra/Por 6 and OS-NF-8800 membranes. The 1 mM PFc solution, corresponding to the theoretical 3.7% cross-over of the 27 mM PFc catholyte, was depicted on the Figure for comparison, while its CV is taken from the data used for Figure S39. Thus, the CV of 1 mM PFc sample was measured in solution, based on the 0.1 M $ZnCl_2$, 0.8 M TMACl electrolyte.

Estimation of RFB technical parameters under the finalized testing conditions

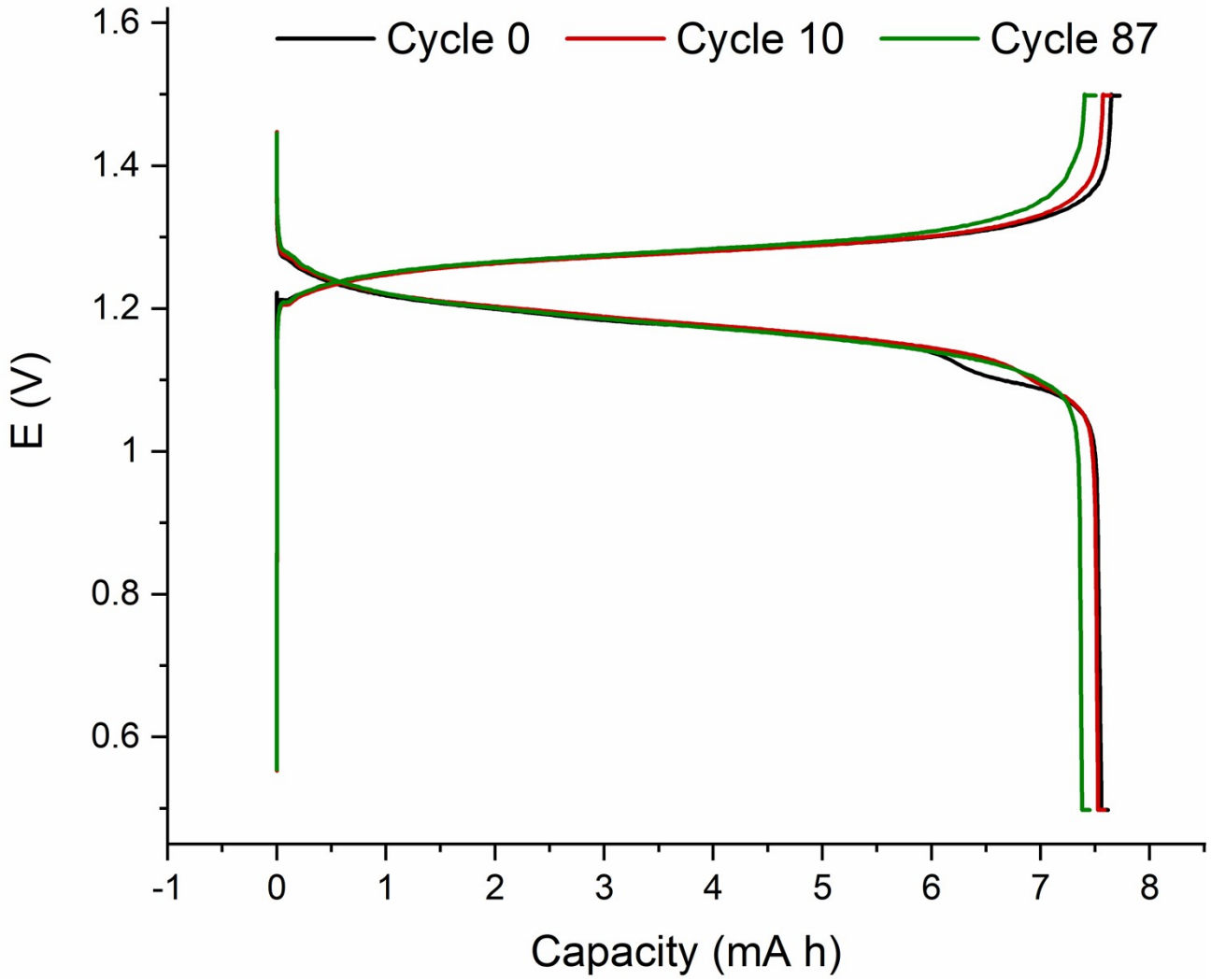

Figure S42 Voltage from capacity curves for the first, the tenth, and the last cycle of the RFB operated under the finally adopted conditions. Lower current cycling regime; 10 mL of 0.1 M $ZnCl_2$, 0.8 M TMACl, 6 mM HCl, pH 4.5-5 anolyte *vs.* 10 mL 0.1 M $ZnCl_2$, 0.8 M TMACl, 6 mM HCl, 27 mM PFc catholyte.

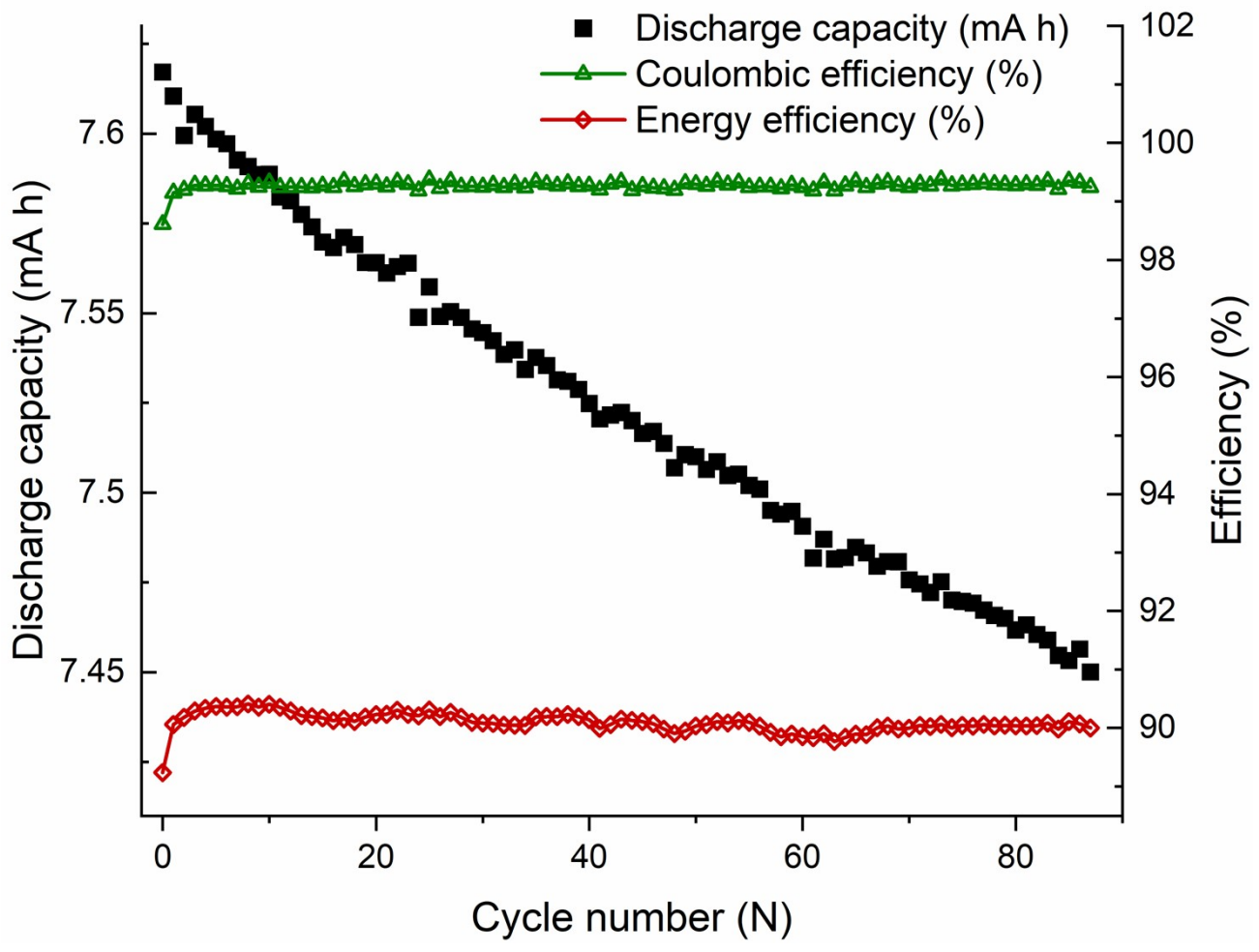

Figure S43 Capacity, CE, and EE dependency from the cycle number from the RFB tested at the finally adopted conditions. Lower current cycling regime; 10 mL of 0.1 M $ZnCl_2$, 0.8 M TMACl, 6 mM HCl, pH 4.5-5 anolyte *vs.* 10 mL 0.1 M $ZnCl_2$, 0.8 M TMACl, 6 mM HCl, 27 mM PFc catholyte.

Photographs depicting precipitate formation on RFB tank walls in setup 3

Figure S44 Gel phase formed at the catholyte tank walls during the full RFB thermal assessment test at 60 °C (setup 3).

Validation of the SOC assessment by the OCV measurement technique

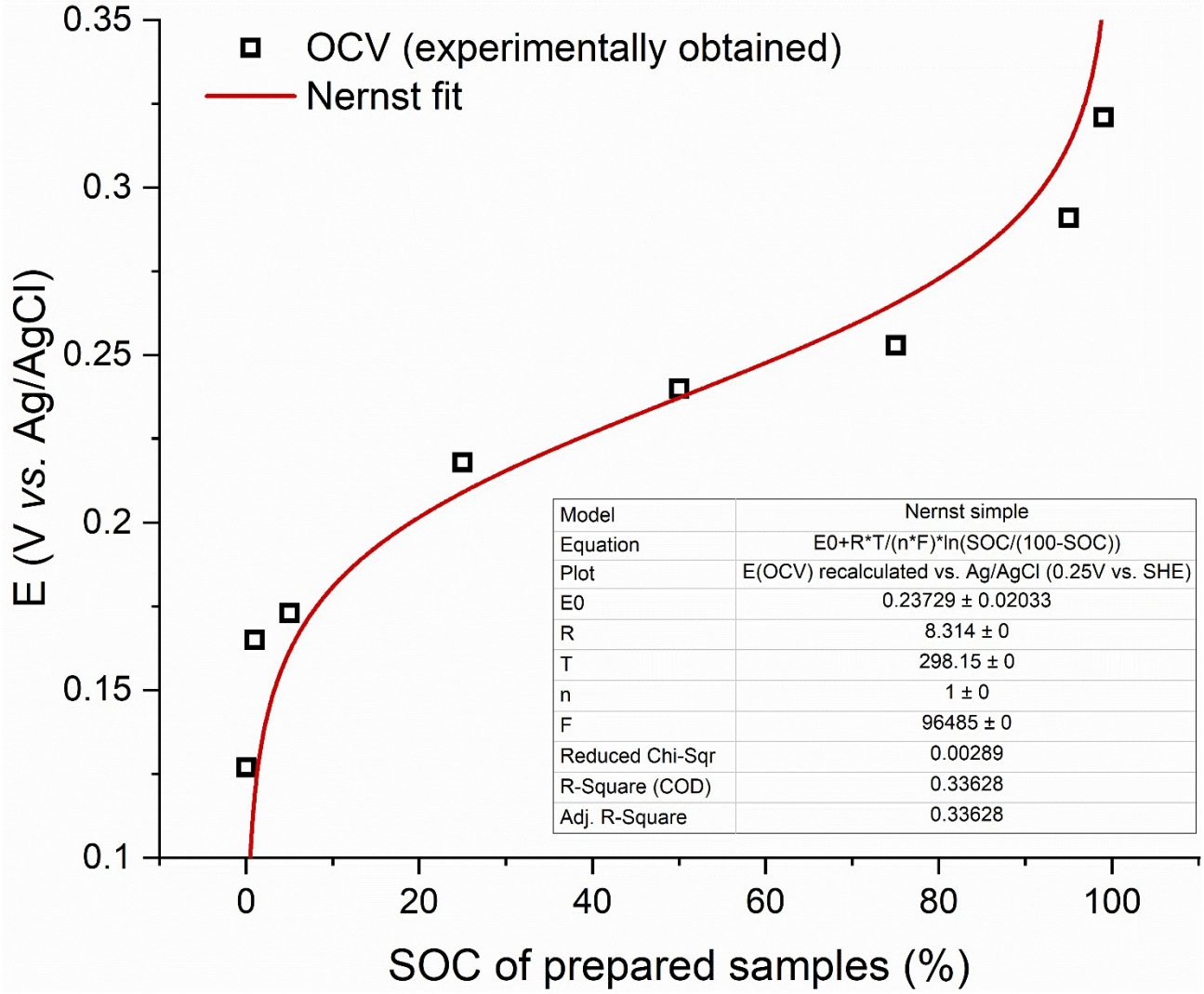

Figure S45 Validation of SOC assessment by OCV measurement technique for the PFc electrolyte.

GS-MS results

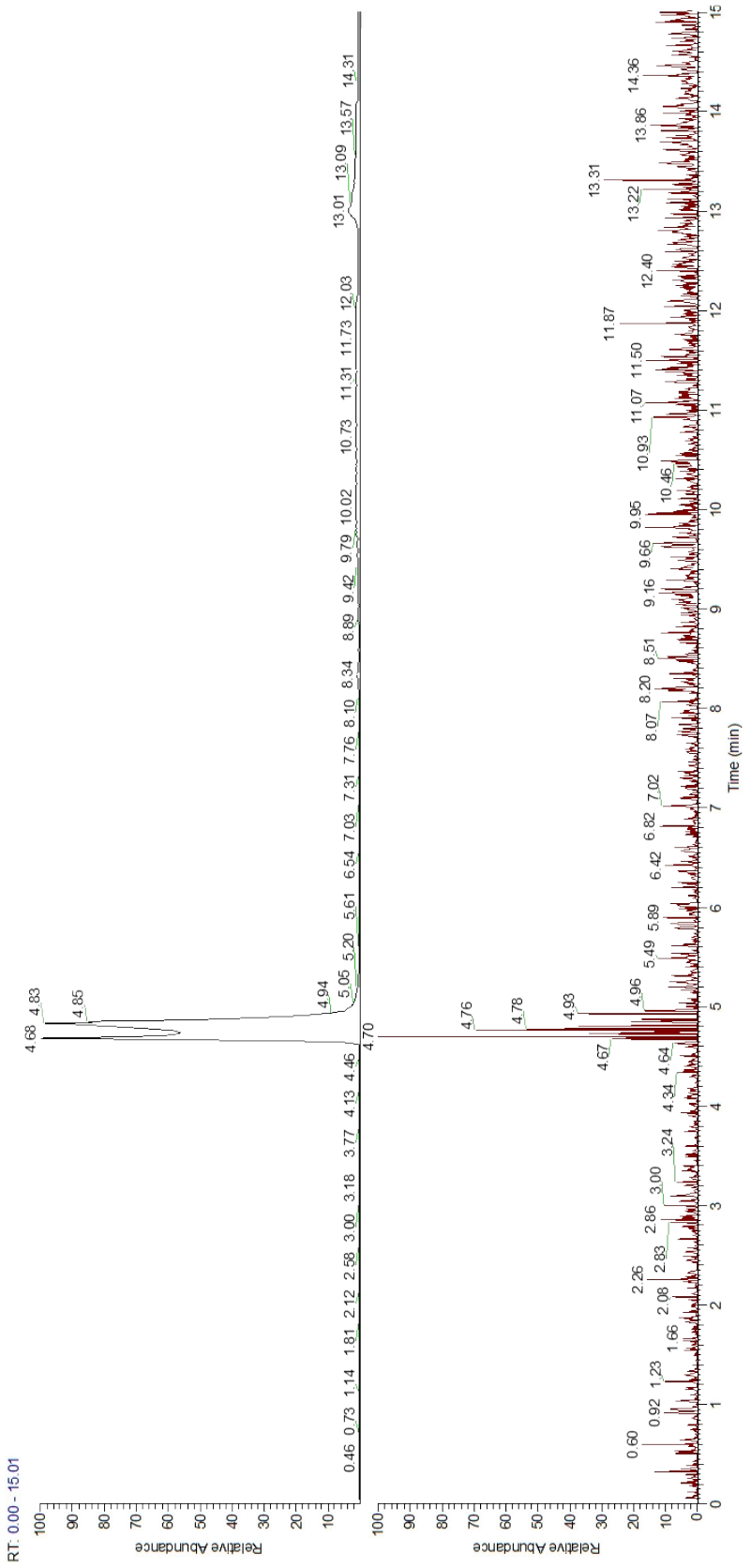

Figure S46 Head-space-GC-MS data of empty vial. Top – total ion current (TIC) (here main signals at 4.70 min and 4.83 min correspond to argon). Below – extracted ion current (EIC) of the mass to charge ratio of 66±0.5 m/z, which is specific for cyclopentadiene (if cyclopentadiene is present, a signal at RT 7.89 min is detected).

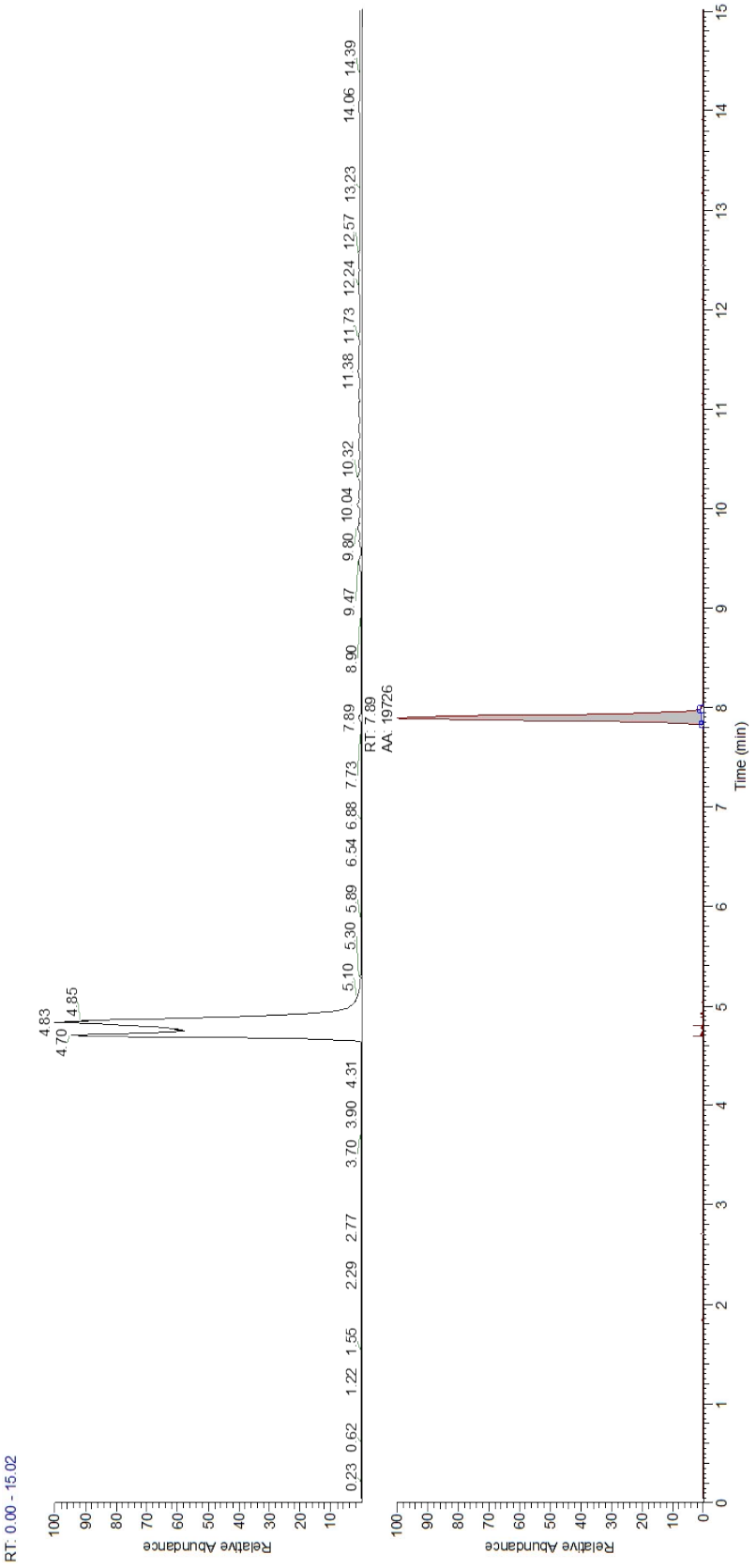

Figure S47 Head-space-GC-MS data of fresh RFB catholyte (0.1 M $ZnCl_2$, 0.8 M TMACl, 6 mM HCl, 27 mM PFc). Top – total ion current (TIC) (here main signals at 4.70 min and 4.83 min correspond to argon). Below – extracted ion current (EIC) of the mass to charge ratio of 66±0.5 m/z, which is specific for cyclopentadiene (if cyclopentadiene is present, a signal at RT 7.89 min is detected).

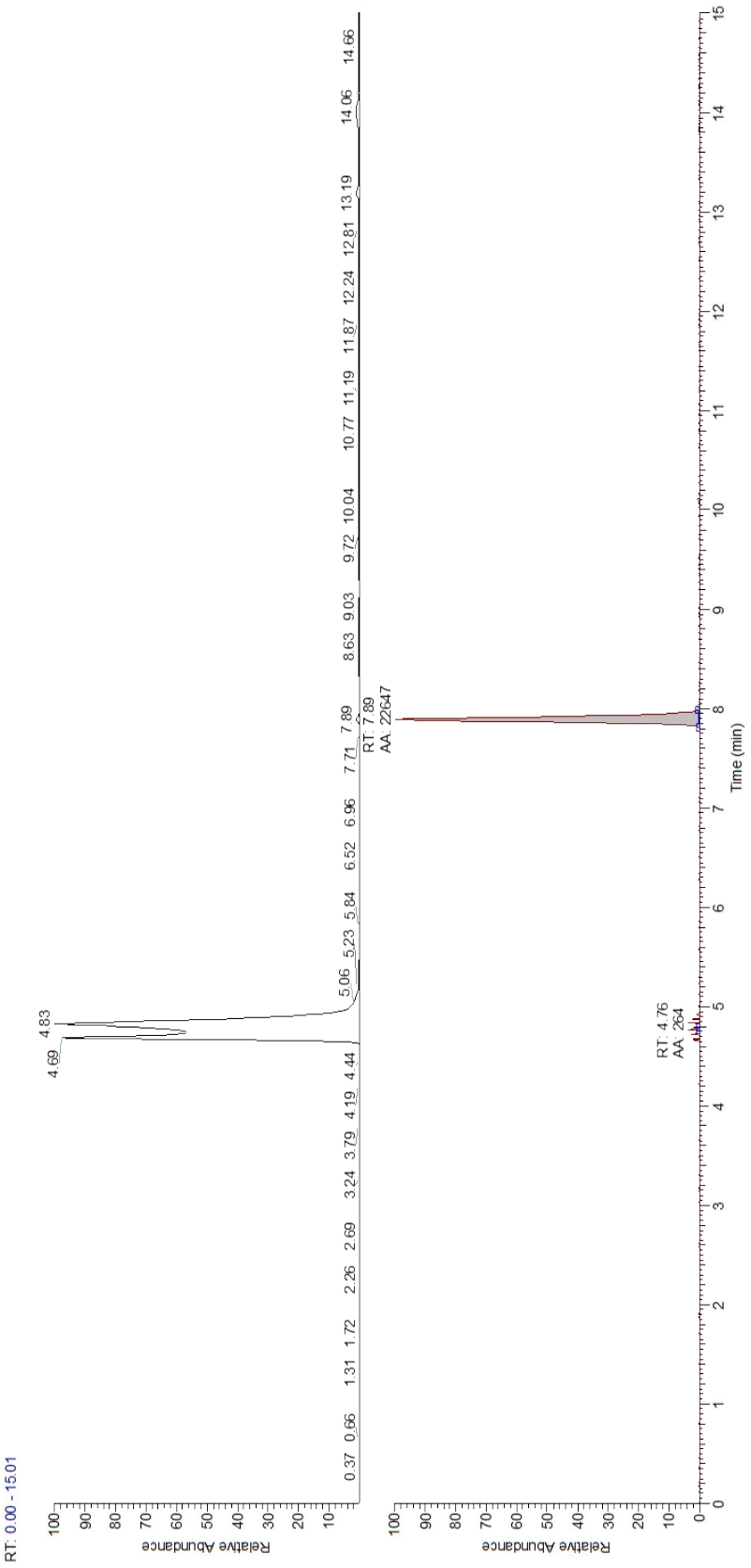

Figure S48 Head-space-GC-MS data of the used catholyte from UCSFCC at 60 °C (0.1 M $ZnCl_2$, 0.8 M TMACl, 6 mM HCl, 27 mM PFc). Top – total ion current (TIC) (here main signals at 4.70 min and 4.83 min correspond to argon). Below – extracted ion current (EIC) of the mass to charge ratio of 66±0.5 m/z, which is specific for cyclopentadiene (if cyclopentadiene is present, a signal at RT 7.89 min is detected).

Evaluation of the apparent rate constants for PFc catholyte fade in full RFBs using different heating setups

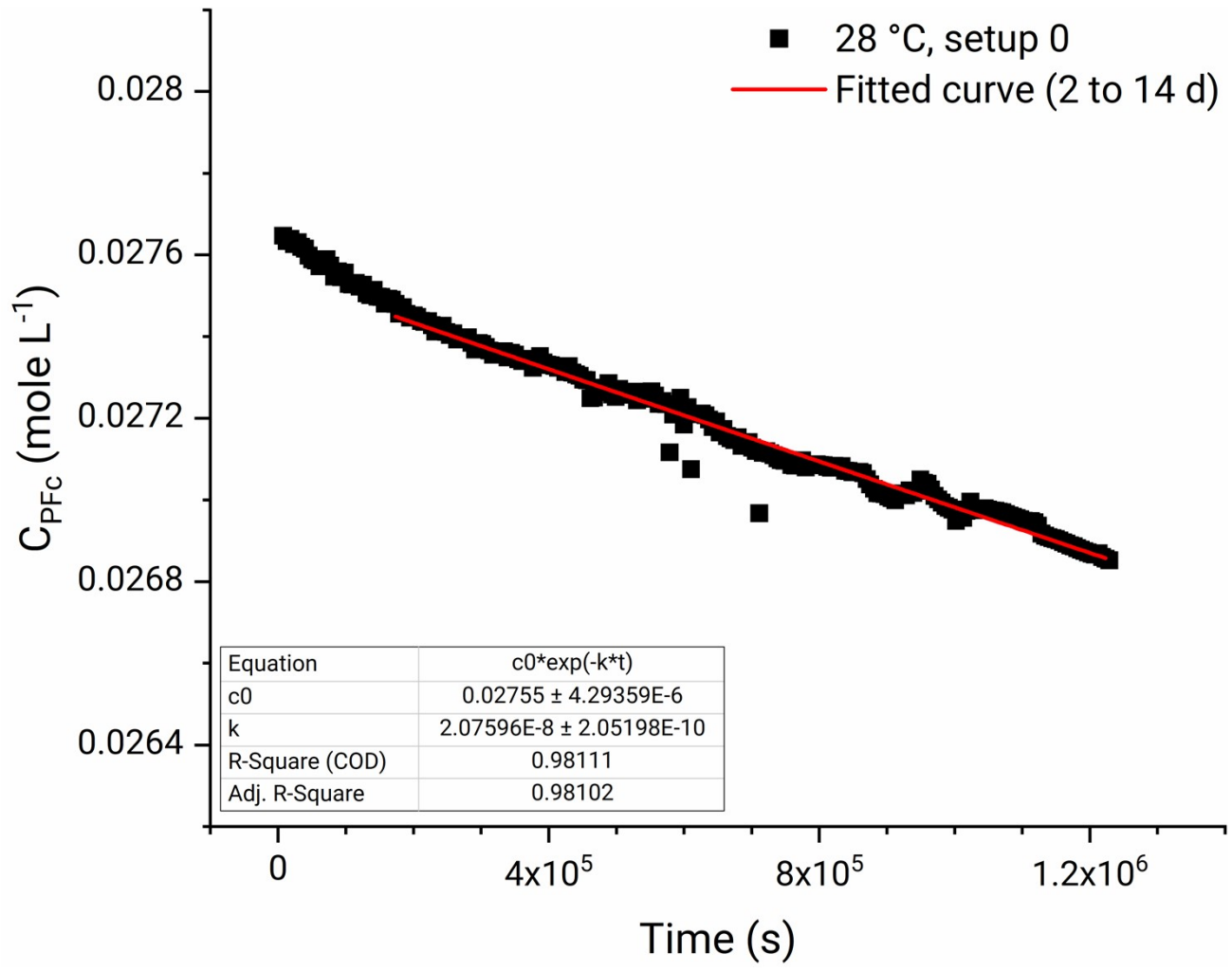

Figure S49 PFc electron equivalent concentration in full RFB *vs.* charge-discharge cycling time and exponential fit to range 2 to 14 d. Heating setup 0 was used and 28 °C bulk catholyte temperature was reached in the tank. PFc concentration was estimated based on discharge capacity assessed at each cycle.

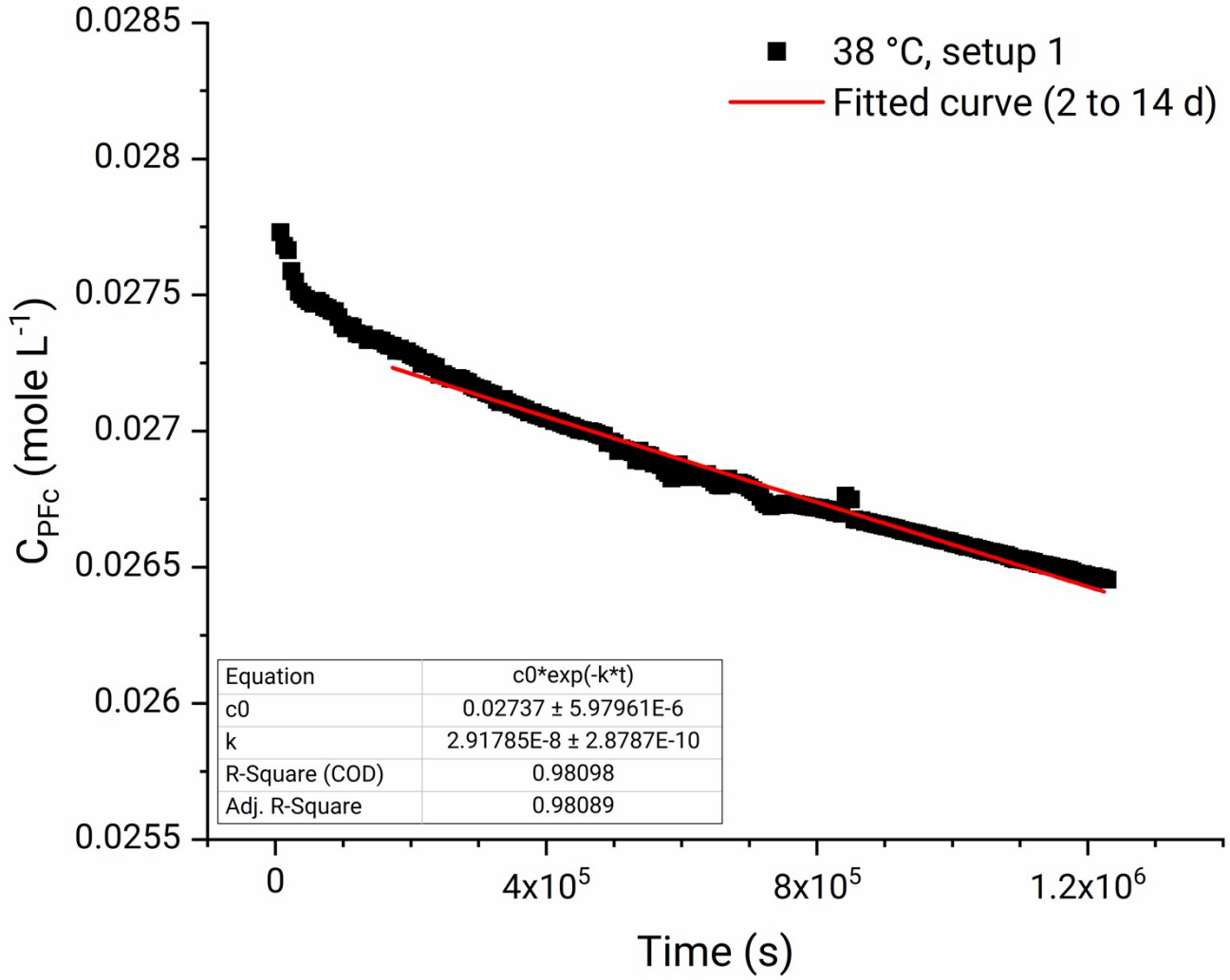

Figure S50 PFc electron equivalent concentration in full RFB *vs.* charge-discharge cycling time and exponential fit to range 2 to 14 d. Heating setup 1 was used and 38 °C bulk catholyte temperature was reached in the tank. PFc concentration was estimated based on discharge capacity assessed at each cycle.

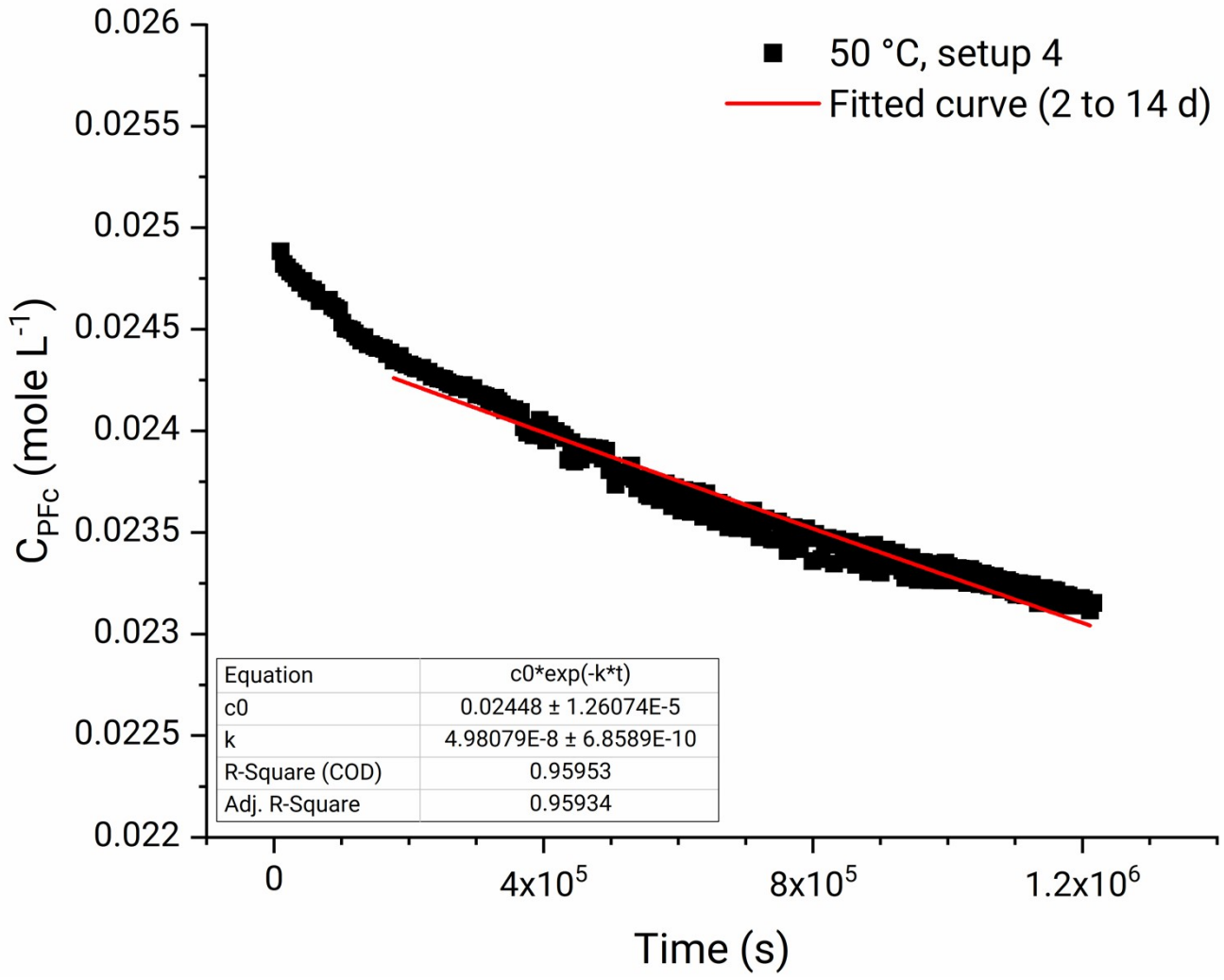

Figure S51 PFc electron equivalent concentration in full RFB *vs.* charge-discharge cycling time and exponential fit to range 2 to 14 d. Heating setup 4 was used and 50 °C bulk catholyte temperature was reached in the tank. PFc concentration was estimated based on discharge capacity assessed at each cycle.

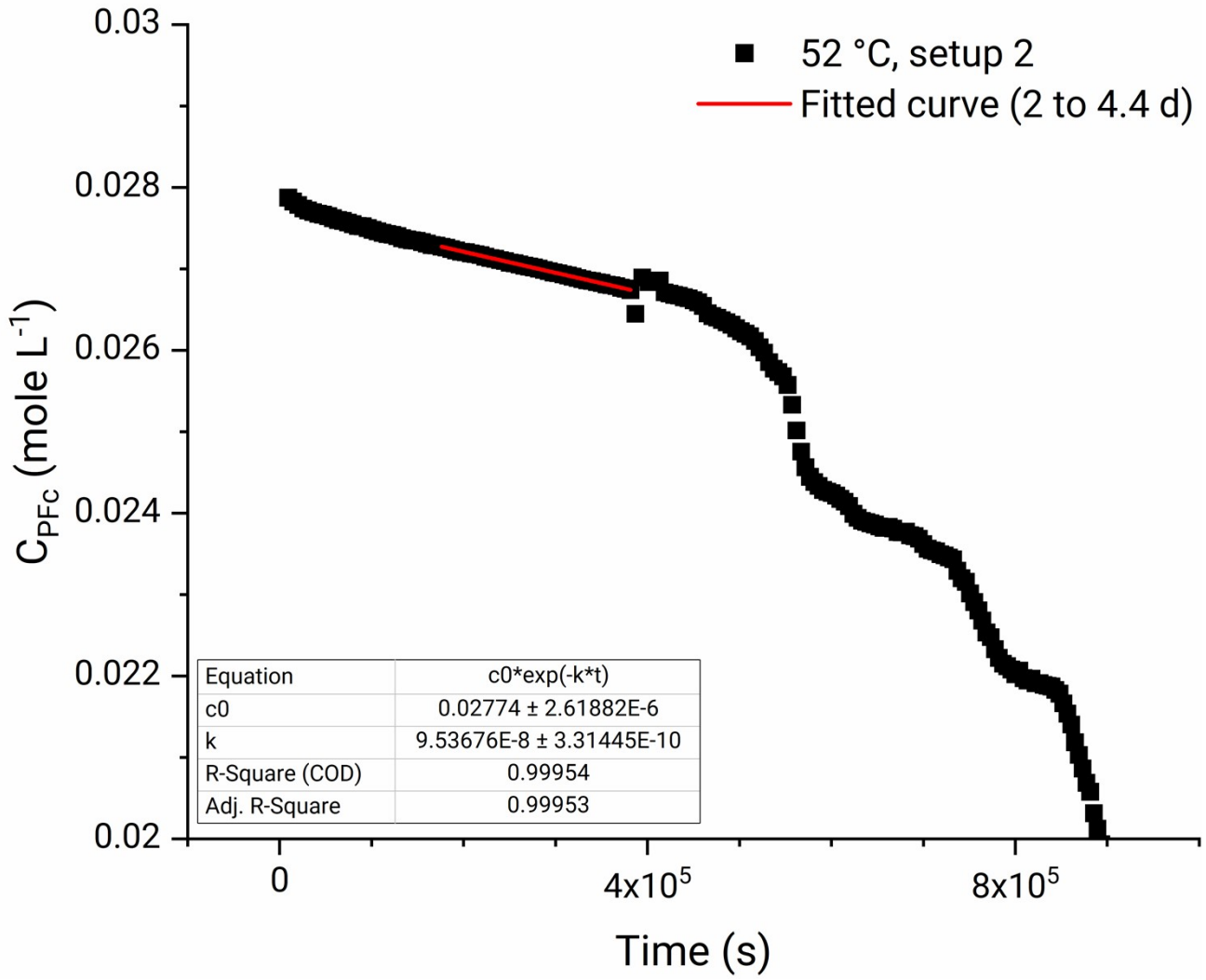

Figure S52 PFc electron equivalent concentration in full RFB *vs.* charge-discharge cycling time and exponential fit to range 2 to 4.4 d. Heating setup 2 was used and 52 °C bulk catholyte temperature was reached in the tank. PFc concentration was estimated based on discharge capacity assessed at each cycle.

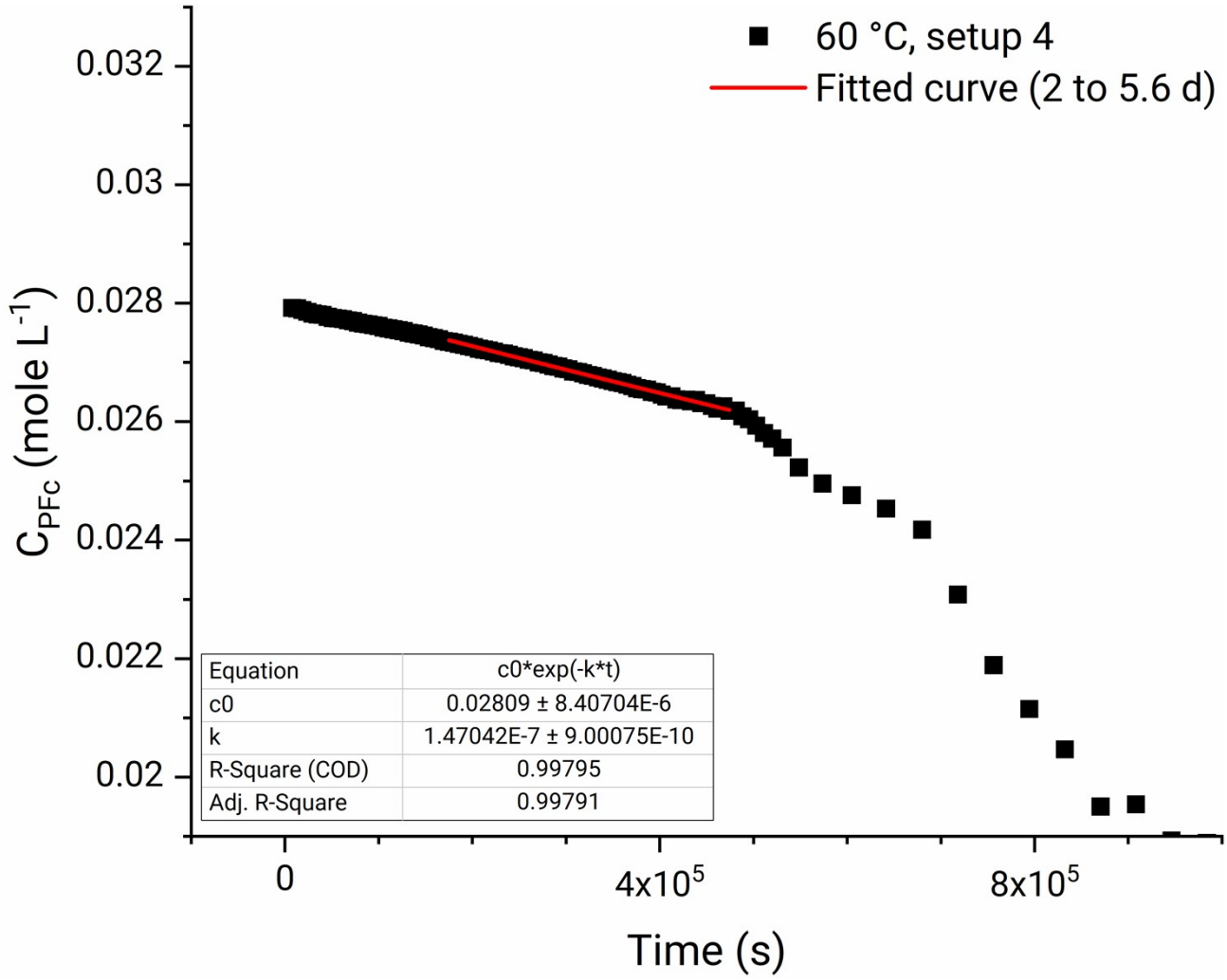

Figure S53 PFc electron equivalent concentration in full RFB *vs.* charge-discharge cycling time and exponential fit to range 2 to 5.6 d. Heating setup 4 was used and 60 °C bulk catholyte temperature was reached in the tank. PFc concentration was estimated based on discharge capacity assessed at each cycle.

Capacity fade rates estimated from the digitized results from the study by Quinn *et al.*[45]

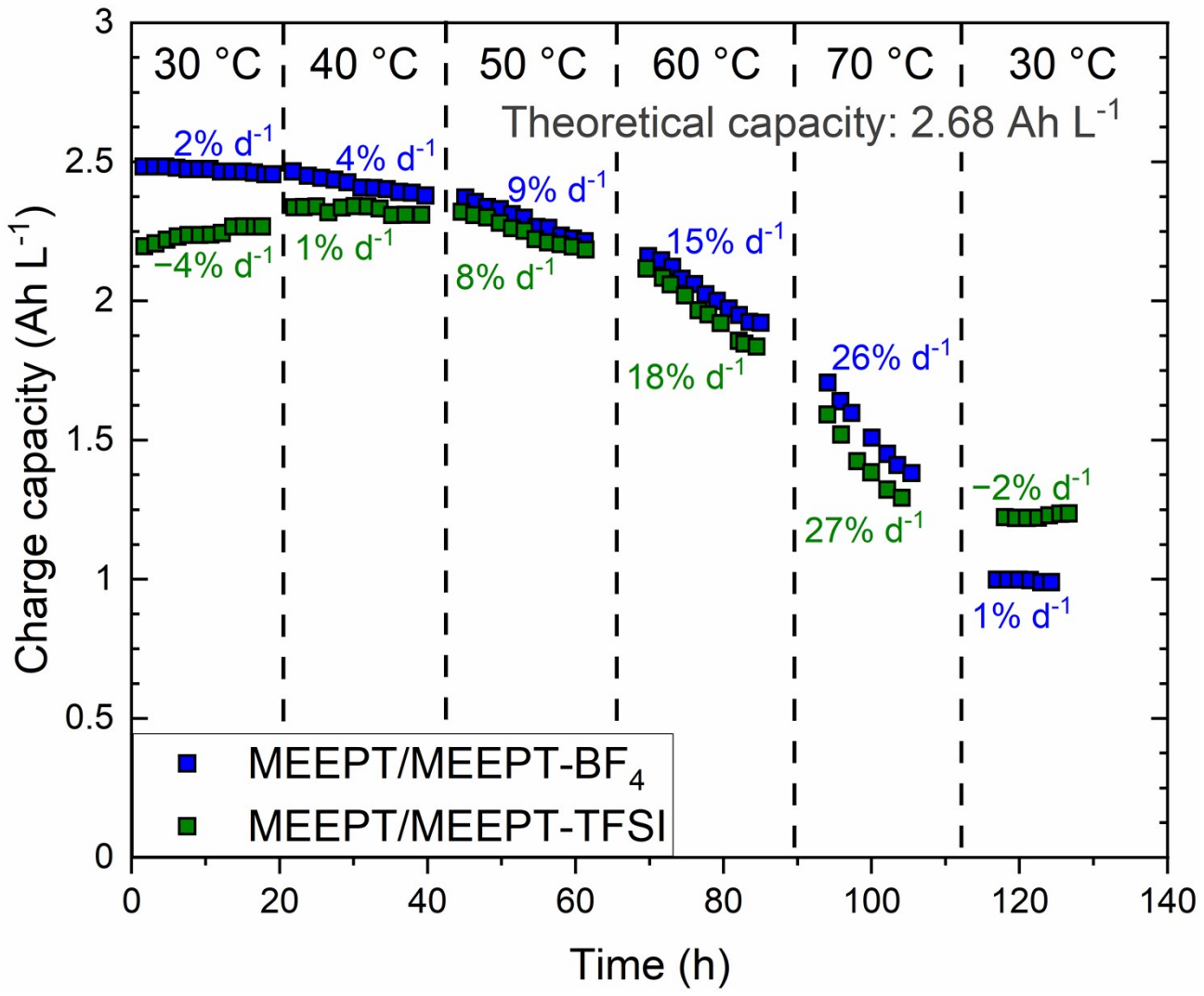

Figure S54 The capacity fade rates from UCSFCC test of the MEEPT molecule, using BF_4 and TFSI counterions. The datapoints were obtained by digitizing of the original data on Figure 5 from the work of Quinn *et al.* with the WebPlotDigitizer program. The original graph includes 10 datapoints for each of the temperatures and electrolyte compositions depicted on the original figure. Since digitalization was performed algorithmically, the digitalized data may contain both more and less datapoints in the same regions in comparison to the original plot.

Mechanism of the diphenylacetate oxidation which is redox mediated by ferrocene[48]

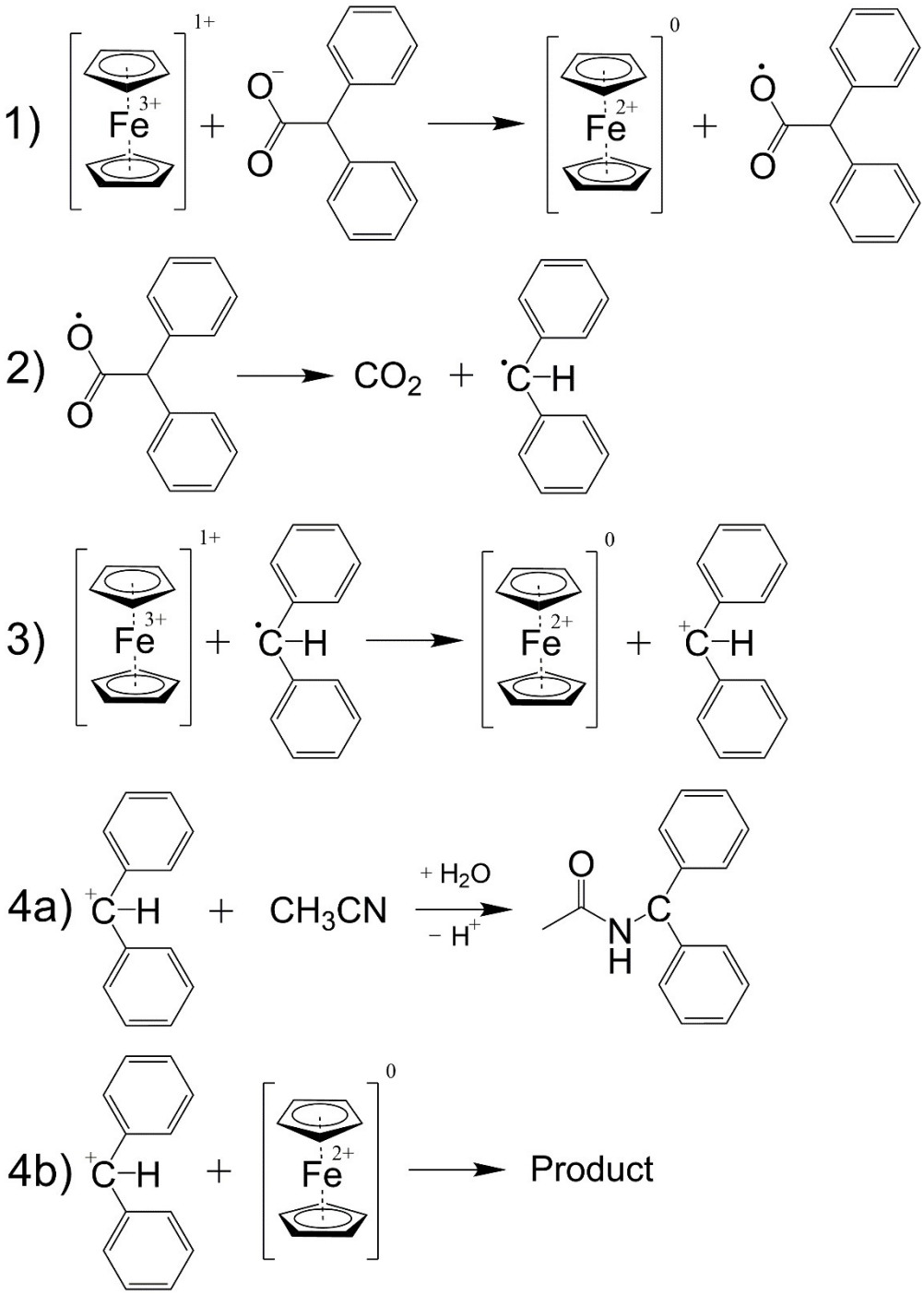

Scheme S1 Schematic representation of the oxidation of diphenylacetate anion by ferrocene in acetonitrile. The second reaction (generation of CO_2) is very fast and unavoidably occurs after the acetate oxidation and transformation into a radical. The carboradicals, occurring as a product in reaction (2), either recombine or undergo one more oxidation step with the charged ferrocene. Apart from the simple acetate anion, the diphenylacetate has bulky substituents located in α-carbon atom, thus, recombination of the occurring carboradicals is unfavorable. Consequently, the oxidation proceeds, yielding reduction of in total two ferrocene complexes. The occurring carbocation reacts both with acetonitrile and with ferrocene. The authors assume that in water, the reaction (4a) yields an alcohol, of an originating carbocation.

References

1. C. Xie, H. Zhang, W. Xu, W. Wang and X. Li, *Angew. Chem. Int. Ed. Engl.*, 2018, **57**, 11171-11176.
2. W. Lu, C. Xie, H. Zhang and X. Li, *ChemSusChem*, 2018, **11**, 3996-4006.
3. A. Tang, S. Ting, J. Bao and M. Skyllas-Kazacos, *J. Power Sources*, 2012, **203**, 165-176.
4. A. Trovò, A. Saccardo, M. Giomo and M. Guarnieri, *J. Power Sources*, 2019, **424**, 204-214.
5. A. Tang and M. Skyllas-Kazacos, *ChemPlusChem*, 2015, **80**, 368-375.
6. Annual climate in Sapporo, https://en.climate-data.org/asia/japan/hokkaido/sapporo-1003/, (accessed November 2023).
7. Annual climate in Sydney, https://en.climate-data.org/oceania/australia/new-south-wales/sydney-24/, (accessed November 2023).
8. Annual climate in Dubai, https://en.climate-data.org/asia/united-arab-emirates/dubai/dubai-705/, (accessed November 2023).
9. The hottest annual climate temperature amoung all cities on Earth, https://www.statista.com/statistics/1110333/hottest-world-cities-highest-annual-temperature/, (accessed November 2023).
10. The coldest annual climate temperature amoung all cities on Earth, https://www.explore.com/1084181/the-coldest-cities-in-the-world/, (accessed November 2023).
11. Annual climate in Oymyakon, https://en.climate-data.org/search/?q=Oymyakon, (accessed November 2023).
12. R. F. Gahn, N. H. Hagedorn and J. S. Ling, presented in part at the Eighteenth Intersociety Energy Conversion Engineering Conference, Orlando, Florida, 1983.
13. Y. K. Zeng, X. L. Zhou, L. An, L. Wei and T. S. Zhao, *J. Power Sources*, 2016, **324**, 738-744.
14. L. Qiao, S. Liu, M. Fang, M. Yang and X. Ma, *Polymers (Basel)*, 2022, **14**, 2245.
15. W. Wang, S. Kim, B. Chen, Z. Nie, J. Zhang, G.-G. Xia, L. Li and Z. Yang, *Energy Environ.l Sci.*, 2011, **4**, 4068.
16. E. H. Kirk, F. Fenini, S. N. Oreiro and A. Bentien, *Batteries (Basel)*, 2021, **7**, 87.
17. Y. B. Liu, L. H. Yu, L. Liu and J. Y. Xi, *Applied Energy*, 2021, **301**, 117454.
18. N. V. Roznyatovskaya, M. Fuhl, V. A. Roznyatovsky, J. Noack, P. Fischer, K. Pinkwart and J. Tubke, *Energy Technol.*, 2020, **8**, 2000445.
19. Y. Yang, Y. Zhang, L. Tang, T. Liu, S. Peng and X. Yang, *J. Power Sources*, 2020, **450**, 227675.
20. Y. Yang, Y. Zhang, T. Liu and J. Huang, *J. Power Sources*, 2019, **415**, 62-68.
21. G. Nikiforidis, A. Belhcen and M. Anouti, *J. Energy Chem.*, 2021, **57**, 238-246.
22. S. Abbas, J. Hwang, H. Kim, S. A. Chae, J. W. Kim, S. Mehboob, A. Ahn, O. H. Han and H. Y. Ha, *ACS Appl. Mater. Interfaces*, 2019, **11**, 26842-26853.
23. Y. N. Zhang, J. Y. Xi, L. Liu and Z. H. Wu, *J. Appl. Electrochem.*, 2020, **50**, 255-264.
24. V. Murugesan, Z. M. Nie, X. Zhang, P. Y. Gao, Z. H. Zhu, Q. Huang, L. T. Yan, D. Reed and W. Wang, *Cell Rep.,* 2021, **2**, 100323.
25. Y. Lee, D. Yun, J. Park, G. Hwang, D. Chung, M. Kim and J. Jeon, *J. Power Sources*, 2022, **547**, 232007.
26. P. K. Leung, C. P. de Leon and F. C. Walsh, *Electrochim. Acta*, 2012, **80**, 7-14.
27. G. Nikiforidis, L. Berlouis, D. Hall and D. Hodgson, *J. Power Sources*, 2013, **243**, 691-698.
28. G. Nikiforidis, L. Berlouis, D. Hall and D. Hodgson, *Electrochim. Acta*, 2014, **115**, 621-629.
29. H. Zhang, D. G. Lek, S. Huang, Y. M. Lee and Q. Wang, *Adv. Mater.*, 2022, **34**, 2202266.
30. X. J. Li, T. Y. Li, P. C. Xu, C. X. Xie, Y. H. Zhang and X. F. Li, *Adv. Funct. Mater.*, 2021, **31**, 2100133.
31. J. Hu, M. Yue, H. Zhang, Z. Yuan and X. Li, *Angew. Chem. Int. Ed. Engl.*, 2020, **59**, 6715-6719.
32. B. Li, Z. M. Nie, M. Vijayakumar, G. S. Li, J. Liu, V. Sprenkle and W. Wang, *Nat. Commun.,* 2015, **6**, 6303.
33. Z. F. Huang, P. Zhang, X. P. Gao, D. Henkensmeier, S. Passerini and R. Y. Chen, *ACS Appl. Energy Mater.*, 2019, **2**, 3773-3779.
34. J. C. Xu, S. Pang, X. Y. Wang, P. Wang and Y. L. Ji, *Joule*, 2021, **5**, 2437-2449.
35. P. Rohland, O. Nolte, K. Schreyer, H. Gorls, M. D. Hager and U. S. Schubert, *Mater. Adv.*, 2022, **3**, 4278-4288.
36. O. Nolte, P. Rohland, N. Ueberschaar, M. D. Hager and U. S. Schubert, *J. Power Sources*, 2022, **525**, 230996.
37. M. Cazot, G. Maranzana, J. Dillet, K. Dale and S. Didierjean, *J. Electrochem. Soc.*, 2020, **167**, 100539.
38. Z. Liang, R. K. Jha, T. M. Suduwella, N. H. Attanayake, Y. Wang, W. Zhang, C. Cao, A. P. Kaur, J. Landon and S. A. Odom, *J. Mater. Chem.*, 2022, **10**, 24685-24693.
39. C. Chu, B. W. Kwon, W. Lee and Y. Kwon, *Korean J. Chem. Eng.*, 2019, **36**, 1732-1739.
40. C. Wiberg, T. J. Carney, F. Brushett, E. Ahlberg and E. G. Wang, *Electrochim. Acta*, 2019, **317**, 478-485.
41. D. R. Chang, Y. Kim and S. Jung, *Int. J. Energy Res.*, 2019, **43**, 4449-4458.
42. X. Xing, Y. Huo, X. Wang, Y. Zhao and Y. Li, *Int. J. Hydrogen Energy*, 2017, **42**, 17488-17494.
43. P. S. Borchers, M. Strumpf, C. Friebe, I. Nischang, M. D. Hager, J. Elbert and U. S. Schubert, *Adv. Energy Mater.*, 2020, **10**, 2001825.
44. P. Rohland, K. Schreyer, M. D. Hager and U. S. Schubert, *RSC Adv.*, 2021, **11**, 38759-38764.
45. A. H. Quinn, K. M. Ripley, N. J. Matteucci, B. J. Neyhouse, C. A. O. Brown, W. P. Woltmann and F. R. Brushett, *J. Electrochem. Soc.*, 2023, **170**.
46. C. Sun and H. Zhang, *ChemSusChem*, 2022, **15**, e202101798.
47. M. Lopez-Atalaya, G. Codina, J. R. Perez, J. L. Vazquez and A. Aldaz, *J. Power Sources*, 1992, **39**, 147-154.
48. L. S. Hernández-Muñoz, A. Galano, P. D. Astudillo-Sánchez, M. M. Abu-Omar and F. J. González, *Electrochim. Acta*, 2014, **136**, 542-549.